PEOPLE'S DEMOCRATIC REPUBLIC OF ALGERIA

MINISTRY OF HIGHER EDUCATION AND SCIENTIFIC RESEARCH

UNIVERSITY MOHAMED KHIDER-BISKRA

Faculty of Sciences and Technology

Department of Electrical Engineering



Doctorate Degree in Electrical Engineering

Speciality: **Renewable Energy**

Option: Intelligent Energy Networks

Theme

Study and Realisation of a Photovoltaic Pumping Installation Prototype for Irrigation in the Field of Agriculture

Presented by **Mohamed Laaouad**

Jury:

President	Kamel Srairi	Professor	University of Biskra
Supervisor	Aicha Guergazi	Associate Prof	University of Biskra
Examiner	Hani Benguesmia	Professor	University of M'sila
Examiner	Sabrina Abdeddaim	Professor	University of Biskra

22 June 2026

RÉPUBLIQUE ALGÉRIENNE DÉMOCRATIQUE ET POPULAIRE

MINISTÈRE DE L'ENSEIGNEMENT SUPÉRIEUR ET DE LA RECHERCHE SCIENTIFIQUE

UNIVERSITÉ MOHAMED KHIDER - BISKRA

Faculté des Sciences et de la Technologie

Département de Génie Électrique



Doctorat en Électrotechnique

Spécialité :**Énergie Renouvelable**

Option : Réseaux Energitique Intelligents

Thème

Etude et Réalisation d'un Prototype d'une Installation de Pompage Photovoltaïque en Vue de L'irrigation dans le Domaine de L'agriculture

Présentée par **Mohamed Laaouad**

Jury :

Président	Kamel Srairi	Professeur	Université de Biskra
Encadreur	Aicha Guergazi	Maître de Conférences A	Université de Biskra
Examinateur	Hani Benguesmia	Professeur	Université de M'sila
Examinateur	Sabrina Abdeddaim	Professeur	Université de Biskra

22 Juin 2026

Acknowledgements

Praise be to Almighty God, who has given me faith, courage, and patience to carry out this work.

I want to express my deep gratitude to my supervisor, Dr. Aicha Guergazi from Biskra University, for the confidence she has placed in me, for her constant presence, and for her guidance, modesty, advice, and constructive remarks regarding the progress of this work.

I would like to thank Prof. Ammar Moussi and everyone who helped me to improve my work and who gave me any remarks that helped me to perfect this manuscript.

I express my deep gratitude to my parents, my brothers, my sister, and my whole family for their encouragement and prayers that allowed me to complete this modest work. I am very grateful for the confidence they have placed in me.

Finally, I express my gratitude to all those who have contributed in one way or another to the development of this work.

O Allah, send your blessings on your noble messenger Mohamed, his family, and companions, and bless us in our life.

Dedication

I dedicate this work to my beloved parents Ahmed and Ben Sahel.A:

whose unwavering faith and countless sacrifices paved every step of this journey. May this dedication serve as a humble testimony of my eternal gratitude and love.

To my brothers Abed Nour, Saber, my sister Yasmine and my wife Oubah.R family who gives me love and liveliness.

To all those who have helped me - directly or indirectly - and those who shared with me the emotional moments during the accomplishment of this work and who warmly supported and encouraged throughout my journey.

To all my friends who have always encouraged me, and to whom I wish more success.

Thanks!

Mohamed LAAOUAD

ملخص

تُقدّم هذه الدراسة استراتيجيات تحكّم متقدمة مطبّقة على منصّتين تجريبيتين تهدفان إلى تحسين تبادل الطاقة وكفاءة الأداء في أنظمة الضخ العاملة بالطاقة الكهروضوئية.

المنصّة الأولى، بعنوان «التحكّم الذكي لإدارة الطاقة المثلى في الأنظمة الكهروضوئية»، تعتمد على وحدة أردوينو ميغا مدمجة مع خوارزميات المنطق الضبابي ومحول رفع الجهد لتشغيل المضخّات التي تعمل بالتيار المستمر. يهدف هذا النظام إلى تحقيق كفاءة عالية مع تقليل تكلفة الأجهزة، ما يجعله حلاً مناسباً للمناطق الريفية والنظم المعتمدة على الطاقة الشمسية خارج الشبكة. وقد أثبتت التجارب أن استخدام المنطق الضبابي يحسّن الاستجابة الديناميكية ويحقق تتبّعاً فعالاً لنقطة القدرة العظمى تحت تغيّر الإشعاع الشمسي.

أما المنصّة الثانية، بعنوان «نظام الري الذكي لتطبيقات الضخّ بالتيار المتناوب»، فتعتمد على منضدة الاختبار الهيدروليكية $HM310$ لدراسة أداء المضخّات الطاردة المركزية العاملة بالتيار المتناوب تحت تحكم تكيفي دقيق. يوفّر النظام مراقبة لحظية وتنظيماً ديناميكياً يوازن بين الكفاءة الهيدروليكية واستهلاك الطاقة.كشف التحليل الإحصائي للبيانات المجمعة عن ارتباط خطي قوي بين تدفق المضخة وسرعة الدوران، بينما يؤدي الري المتحكم به بكفاءة هيدروليكية إلى أقصى حد من توفير الطاقة والمياه.

تُبرز هذه النتائج التكامل بين نظامي التحكم المقترحين لتشكيل إطار شامل لتحسين أنظمة الضخّ الكهروضوئية في كلٍّ من التيار المستمر والمتناوب، مما يسهم في تطوير حلول فعالة طاقياً، منخفضة التكلفة، وذات أتمتة ذكية تناسب احتياجات الزراعة الحديثة في مناطق زراعية مختلفة و بيئات مناخية متغيرة.

الكلمات المفتاحية: الضخ الكهروضوئية؛ التحكم الذكي ؛ الري الآلي؛ التحقق التجريبي؛ الزراعة المستدامة.

Abstract

This research introduces and evaluates advanced control strategies for two experimental test benches designed to enhance energy exchange and performance in photovoltaic water pumping systems. The first test bench, titled **"Intelligent Control for Optimised Power Management in Photovoltaic Systems"**, integrates an Arduino Mega controller with fuzzy logic algorithms and a DC-DC boost converter to regulate direct current pumps. This configuration aims to achieve high efficiency with reduced hardware costs, providing a technically viable alternative for rural and off-grid irrigation applications. Experimental results confirm that intelligent fuzzy control significantly improves dynamic response and maintains maximum power point tracking under variable irradiance conditions.

The second experimental setup, **"Smart Irrigation System for Large-scale AC Pumping Applications"**, utilises the HM 310 hydraulic test bench to practically investigate the performance of AC centrifugal pumps under a photovoltaic environment. This system incorporates real-time monitoring and adaptive control to properly balance hydraulic efficiency and energy consumption. Statistical analysis of the collected data revealed a strong linear correlation between pump flow rate and rotational speed, while efficient hydraulically controlled irrigation maximises energy and water savings.

Together, these two control architectures demonstrate a coherent framework for optimising photovoltaic water pumping systems across DC and AC domains. The developed approaches contribute to energy-efficient, cost-effective, and sustainably automated irrigation solutions suited to diverse agricultural and climatic conditions.

.

Key words: *Solar Photovoltaic pumping, Intelligent control, Automated irrigation, Experimental validation, Sustainable agriculture.*

Résumé

Cette recherche présente et évalue des stratégies de commande avancées appliquées à deux bancs d'essai expérimentaux destinés à améliorer l'échange énergétique et les performances des systèmes de pompage photovoltaïques.

Le premier banc, intitulé « **Commande intelligente pour la gestion optimisée de l'énergie dans les systèmes photovoltaïques** », repose sur l'intégration d'un Arduino Mega associé à un contrôleur logique flou et à un convertisseur élévateur de tension boost pour les pompes à courant continu. Cette configuration permet de réduire le coût global du matériel tout en augmentant l'efficacité énergétique. Les essais expérimentaux ont démontré que la logique floue améliore significativement la réponse dynamique et maintient un suivi optimal du point de puissance maximale, même sous des conditions d'irradiance variable.

Le second dispositif, intitulé « **Système d'irrigation intelligent pour applications de pompage à courant alternatif** », utilise le banc d'essai hydraulique HM 310 pour étudier pratiquement les performances des pompes centrifuges AC dans un environnement photovoltaïque. Ce système intègre une surveillance en temps réel et un contrôle adaptatif pour équilibrer correctement l'efficacité hydraulique et la consommation d'énergie. L'analyse statistique des données collectées a révélé une forte corrélation linéaire entre le débit de la pompe et la vitesse de rotation, tandis qu'une irrigation contrôlée, hydrauliquement efficace, maximise les économies d'énergie et d'eau.

L'ensemble de ces approches propose un cadre cohérent pour l'optimisation des systèmes de pompage photovoltaïques, tant en courant continu qu'en courant alternatif, contribuant au développement de solutions d'irrigation écoénergétiques, économiques et intelligemment automatisées, adaptées aux réalités agricoles contemporaines.

Mots clés :*Pompage solaire photovoltaïques , Commande intelligente, Irrigation automatisée, Validation expérimentale, Agriculture durable.*

Contents

List of Figures

List of Tables

List of Abbreviations

General introduction **1**

I INTRODUCTION AND LITERATURE REVIEW **3**

I.1 Introduction 3

I.1.1 Background 4

I.2 Irrigation in Modern Agriculture 7

I.3 Automated Irrigation System in Cultivated Land 7

I.4 Types of Irrigation 8

I.4.1 Manual Irrigation 8

I.4.2 Surface Flow (Gravity) Irrigation 9

I.4.3 Sprinkler Irrigation 10

I.4.4 Micro-Irrigation (Drip Irrigation) 11

I.4.5 Precision Irrigation 12

I.4.6 Statement of the Problem 14

I.4.7 Objectives 15

I.4.8 Thesis Contributions 16

I.4.9 Thesis Outlines 17

I.5 Conclusion 17

II MODEL PRESENTATION OF DIRECT PHOTOVOLTAIC IRRIGATION SYSTEMS **19**

II.1 Photovoltaic Array Components 20

II.2 Photovoltaic Cell 21
II.3 Photovoltaic Module 23
II.4 Meteorological Influences on PV Modules 24
II.4.1 Impact of Irradiation (G) 25
II.4.2 Impact of Temperature (T_c) 27
II.5 Electronic Power Converters 28
II.5.1 DC–DC Boost Converter 28
II.5.2 DC–AC Voltage Source Inverter 31
II.6 Pump Unit 32
II.6.1 DC Pump Unit 32
II.6.2 AC Pump Units 34
II.6.3 Three Phase Induction Motor Equations 37
II.6.4 Equivalent Two-Phase (d–q) Model 38
II.7 Centrifugal Pump 40
II.8 Conclusion 42

III DEVELOPED TECHNIQUES 43
III.1 Introduction 43
III.2 Intelligent Control for Optimised power Management in photostatic system 43
III.3 Structural Overview 44
III.4 Energy Control Strategy 45
III.4.1 Fuzzification 46
III.4.2 Rules 46
III.4.3 Intelligence Inference 47
III.4.4 Defuzzification 47
III.4.5 Hardware Control components 47
III.5 Smart Irrigation AC coupled PV pumping System for Large-scale Applications 48
III.5.1 PV AC pumping Test bench 48
III.5.2 Implementation Structure Overview 48
III.5.3 PV energy production 49
III.5.4 Solar Energy Conversion 50
III.5.5 Energy Management 51
III.5.6 Irrigation control Via VSD 52
III.5.7 System operation 52
III.5.8 Role of water in vegetation 54

III.6 Water requirements of cultivated plants 55
III.6.1 Irrigation Grassland 56
III.7 Conclusion 57

IV IMPLEMENTATION AND TESTS RESULTS 58
IV.1 Introduction 58
IV.2 First Experimental DC Prototype 59
IV.2.1 Photovoltaic Module 59
IV.2.2 Boost converter setup 60
IV.2.3 Arduino Mega Microcontroller 62
IV.2.4 Current sensor LA55 63
IV.2.5 Voltage sensor LV25 64
IV.2.6 Arduino Mega PWM signal 65
IV.2.7 PWM signal Adaptation 66
IV.2.8 Climatic Data of PV System Test Site 66
IV.2.9 Experimental Fuzzy logic MPPT Results 67
IV.2.10Pump Unit Performance 69
IV.3 Conclusion 70
IV.4 AC Prototype Experimental Validation Results and Discussion 71
IV.4.1 Introduction 71
IV.4.2 Test Bench Setup 71
IV.4.3 Testing Procedure 74
IV.4.4 Soil Moisture Sensor FC 28 76
IV.5 Hydraulic Performance 77
IV.5.1 Measured Parameters 77
IV.5.2 Head–Discharge Relationship 77
IV.5.3 Power and Efficiency Evaluation 78
IV.5.4 Effect of Rotational Speed 79
IV.6 Electrical and Control Response 79
IV.6.1 Measured Control Variables 79
IV.6.2 Motor Speed and Electrical Power Coupling 80
IV.6.3 Control Response to Soil Moisture Feedback 81
IV.6.4 Transient Response and Stability 81
IV.6.5 Energy Utilisation 82
IV.6.6 Discussion and Implications 82

IV.7 Soil Moisture Dynamics 83
IV.8 Moisture Variation During Irrigation Cycles 83
IV.8.1 System Responsiveness and Control Logic 84
IV.8.2 Sensor Stability and Signal Integrity 85
IV.8.3 Post-Irrigation Moisture Retention 86
IV.8.4 Energy–Moisture Correlation 86
IV.8.5 Discussion and Implications 86
IV.9 Energy Analysis 87
IV.9.1 Measured Power Characteristics 87
IV.10 Power–Speed Relationship 87
IV.10.1 Power–Flow Efficiency Analysis 88
IV.10.2 Variable Frequency Operation and Energy Savings 89
IV.10.3 System Efficiency and Energy Utilisation 90
IV.10.4 Cumulative Energy Consumption 91
IV.10.5 Discussion and Implications 92
IV.11 Grassland Field Experimentation 92
IV.11.1 Experimental Conditions 93
IV.11.2 Temporal Variation of Environmental Parameters 93
IV.11.3 Soil Moisture Response to Irrigation Events 94
IV.11.4 Pressure and Flow Uniformity Across the Plot 95
IV.11.5 Evapotranspiration Correlation Analysis 95
IV.11.6 System Responsiveness and Control Reliability 96
IV.11.7 Overall Field Performance Discussion 97
IV.12 Conclusion 98
Future Perspectives 100

References **102**

A

Appendix A

A.1 Power pack sizing . . . . .
A.1.1 Charge sheet . . . . .
A.1.2 Determination of the values of L, C1 and C2 . . . . .
A.2 SAER elettropompe BP 6 C data sheet . . . . .

List of Figures

I.1 Manual irrigation using a watering can for small-scale crop watering. 9
I.2 Surface (gravity) irrigation through open channels and field ditches. 10
I.3 Sprinkler irrigation system delivering pressurised water uniformly 11
I.4 Drip irrigation system supplying water directly to plant root zones. 12
I.5 Precision irrigation system integrating sensor feedback and automated control for optimised water application 13

II.1 PV array structure. 21
II.2 Equivalent circuit of a photovoltaic cell. 22
II.3 Equivalent circuit of a photovoltaic module. 24
II.4 Current–voltage characteristics of the photovoltaic module at different irradiance levels ($T_c = 25°C$). 25
II.5 Power–voltage characteristics of the photovoltaic module at different irradiance levels ($T_c = 25°C$). 26
II.6 Current–voltage characteristics of the photovoltaic module for varying temperatures ($T_c = 0, 15, 25, 35, 45, 65°C$) at $E = 1000\ W/m^2$. 27
II.7 Power–voltage characteristics of the photovoltaic module for varying temperatures ($T_c = 0, 15, 25, 35, 45, 65°C$) at $E = 1000\ W/m^2$. 27
II.8 Waveforms of currents and voltages in the boost converter. 29
II.9 Equivalent circuit of a three phase voltage source inverter. 31
II.10 Pump unit electrical types. 32
II.11 Induction motor presentation. 35
II.12 Schematic representation of the induction motor. 37

III.1 Block diagram applied structure 45
III.2 Schematic electronic circuit of the proposed structure. 46
III.3 LARHYSS Laboratory Solar PV field. 49

III.4 3 kW Xantrex SW3048E DC-AC inverter-charger 51
III.5 VSD irrigation block diagram 52
III.6 Block diagram of implemented smart irrigation system architecture. 54

IV.1 First experimental test bench 59
IV.2 Photovoltaic module used in the experimental setup. 60
IV.3 Boost converter 61
IV.4 Arduino Mega 62
IV.5 Current sensor LA55 64
IV.6 Voltage sensor LV25 65
IV.7 PWM signal of Arduino mega with DDS Function Generator signal 65
IV.8 PWM signal amplification 66
IV.9 Ambient climatic conditions: (a) Radiation, (b) Temperature 67
IV.10PV panel power and chopper output power 68
IV.11Incremental MPP as a Function of Voltage 68
IV.12Discharge function pump power 69
IV.13HM 310 centrifugal pump test bench 73
IV.14Irrigation Test Field 73
IV.15The photovoltaic pumping system operating organisational chart 75
IV.16Arduino Uno board architecture 76
IV.17Soil Moisture Sensor FC-28 76
IV.18Relationship between head and discharge showing near linear behavior. . . . 78
IV.19Pump Efficiency vs Flow Rate 78
IV.20Discharge Variation with Pump Speed. 79
IV.21Variation of Electrical Power vs Motor Speed 80
IV.22Proportional control behavior between PWM and frequency 81
IV.23Motor speed adjustment according to soil moisture variation. 81
IV.24Transient Pressure Response of the Control Loop 82
IV.25Soil Moisture Dynamics Before and After Irrigation. 84
IV.26Pump Activation Trigger Based on Moisture Feedback 85
IV.27Short term stability of soil moisture sensor output under steady conditions. . 85
IV.28Post-Irrigation Moisture Retention Curve 86
IV.29Electrical Power in relation to Motor Speed for the irrigation pump. 88
IV.30Measured power consumption in relation to flow rate 89
IV.31Energy Comparison between Operating Modes 90

IV.32System Efficiency Curve. 91
IV.33Cumulative electrical energy consumption comparing VSD and constant speed modes. 92
IV.34Patterns of Solar Radiation and Ambient Temperature Variation recorded during the field tests. 94
IV.35Soil Moisture Response During Irrigation Events. 95
IV.36Pressure distribution along irrigation lateral showing uniform delivery. 95
IV.37Relationship Between Solar Radiation and ET Rate. 96
IV.38Pressure Stability During On–Off Control Cycle. 97

List of Tables

III.1 PV module characteristic. 50
III.2 Water demand variations across plants 56

IV.1 Electrical parameters of the 20 W photovoltaic module. 60
IV.2 Boost converter setup 61
IV.3 Main characteristics of the Arduino Mega 2560 63
IV.4 Sample of experimental data for pump performance 77
IV.5 Sample of control and electrical data during irrigation 80
IV.6 Measured electrical and hydraulic parameters during irrigation 87
IV.7 Representative parameters during field experimentation in May (Biskra region). 93

List of Abbreviations

AC	Alternating Current
DC	Direct Current
VFD	Variable Frequency Drive
PWM	Pulse Width Modulation
ADC	Analog-to-Digital Converter
MCU	Microcontroller Unit
IGBT	Insulated-Gate Bipolar Transistor
MOSFET	Metal–Oxide–Semiconductor Field-Effect Transistor
SCADA	Supervisory Control and Data Acquisition
DCDC	DC–DC Converter
HP	Horsepower
TDH	Total Dynamic Head
PV	Photovoltaic
PVG	Photovoltaic Generator
MPPT	Maximum Power Point Tracker
MPP	Maximum Power Point
GHI	Global Horizontal Irradiance
DNI	Direct Normal Irradiance
SoC	State of Charge
E	Solar irradiance (W/m^2)
S	Surface area of the PV module (m^2)

I_{ph}	Photocurrent generated by the PV cell (A)
I_d	Diode current (A)
I_0	Diode saturation current (A)
I_s	Reverse saturation current of PN junction (A)
I	Load current (A)
I_{sc}	Short-circuit current (A)
I_{mpp}	Current at maximum power point (A)
I_R	Current through shunt resistance R_{sh} (A)
V_p	PV cell voltage (V)
V_{oc}	Open-circuit voltage (V)
V_{mpp}	Voltage at maximum power point (V)
R_s	Series resistance (Ω)
R_{sh}	Shunt resistance (Ω)
N_s	Number of cells in series
N_p	Number of cells in parallel
P_M	Maximum output power (W)
η	PV generator efficiency
η_c	Solar cell efficiency
α	Converter duty cycle
q	Electron charge (1.602×10^{-19} C)
k	Boltzmann constant (1.38×10^{-23} J/K)
T	Absolute temperature (K)
U_T	Thermal voltage (V)
P_e	Input power (W)
P_s	Output power of the PV generator (W)

BLDC	Brushless Direct Current motor
VSD	Variable Speed Drive
HM	Hydraulic Machine (test bench series)
RS-232	Recommended Standard 232 (serial communication)
USB	Universal Serial Bus
ISP	In-System Programming
ICSP	In-Circuit Serial Programming
TTL	Transistor–Transistor Logic
UART	Universal Asynchronous Receiver–Transmitter
SPI	Serial Peripheral Interface
I2C	Inter-Integrated Circuit
DDS	Direct Digital Synthesis
LA55	Hall-effect current sensor (LEM LA55-P)
LV25	Voltage transducer (LEM LV25-P)
FC-28	Soil moisture sensor module
LM393	Comparator-based sensor interface module
ADC	Analog-to-Digital Converter
Q	Volumetric flow rate ($\mathrm{L\,h^{-1}}$)
H	Hydraulic head (bar or m)
N	Rotational speed (rpm)
TDH	Total Dynamic Head
ET	Evapotranspiration
FAO	Food and Agriculture Organization
P_e	Electrical input power (W)
P_m	Mechanical shaft power (W)
P_h	Hydraulic power (W)
f	Electrical frequency (Hz)
V_{pv}	PV terminal voltage (V)
I_{pv}	PV output current (A)

PWM	Pulse Width Modulation
MPP	Maximum Power Point
MPPT	Maximum Power Point Tracking
η	Overall system efficiency (%)
ρ	Water density ($\mathrm{kg\,m^{-3}}$)
g	Gravitational acceleration ($\mathrm{m\,s^{-2}}$)

General introduction

Water scarcity is emerging as one of the most critical challenges of our time, intensifying the need for innovative approaches in water management and modern agriculture. With the increasing pressures of climate change, rapid population growth, and depleting freshwater resources, traditional irrigation systems are being rethought in favor of more efficient, intelligent, and sustainable methods. Recent studies have highlighted that renewable energy-based irrigation systems and smart control technologies not only conserve water but also enhance agricultural productivity and sustainability [1].

This thesis is structured to explore a comprehensive pathway toward sustainable water management in agriculture through the integration of photovoltaic irrigation water pumping systems with intelligent control techniques. In Chapter 1, we set the stage with an introduction and literature review, examining the background of the global water crisis and the challenges faced by modern agriculture. This section also discusses the role of smart irrigation systems – which leverage advanced sensors, artificial intelligence, and data analytics – as key solutions for reducing water waste and improving crop yield [2].

Chapter 2 delves into the photovoltaic irrigation water pumping system. It provides an in-depth look at the components of these systems, including photovoltaic arrays, cells, modules, and the influence of meteorological conditions on their performance. This chapter further evaluates the role of electronic power converters and the operational dynamics of pump units, echoing best practices in sustainable and renewable energy use as documented by several international initiatives [3][4].

In Chapter 3, we focus on the development of advanced techniques for optimizing these irrigation systems, particularly through intelligent control strategies. Here, innovative methodologies such as fuzzy logic for power management, as well as the design of structure and control hardware, are presented. Recent advancements in smart irrigation controllers demonstrate how integrated sensor networks and data-driven decision-making can significantly boost water use efficiency while adapting to variable environmental conditions [5].

Finally, Chapter 4 presents the experimental implementations and test results that vali-

date the proposed systems and control strategies. The real-world performance data collected from test benches underscore the practical benefits of combining photovoltaic power generation with precision irrigation techniques. The experiments serve to confirm that these integrated systems can mitigate water scarcity, reduce operational costs, and ultimately contribute to enhanced food security and sustainable agricultural practices[6].

In essence, this thesis contributes a holistic approach to modern irrigation challenges by integrating renewable solar energy with advanced smart irrigation technologies. Through both theoretical insights and practical validations, the work aims to offer a robust framework for addressing water scarcity and promoting sustainable agricultural development in the face of global climate challenges.

Chapter I

INTRODUCTION AND LITERATURE REVIEW

I.1 Introduction

Electrical energy serves as a cornerstone of modern development, compelling nations to expand their production capacity amid rising global demand driven by industrialization, population growth, and technological advancement [7]. To ensure sustainable progress, reducing reliance on fossil fuels has become imperative, as these sources contribute significantly to environmental degradation and climate change [8]. However, balancing growing energy consumption with production presents challenges, including stringent environmental regulations, rising costs, and the need for reliable infrastructure [9]. In this context, renewable energy emerges as a transformative solution enabling countries, particularly developing ones, to meet escalating electricity demands while advancing energy security, economic stability, and environmental sustainability [10].

This transition is especially critical in sectors like agriculture, where rural communities often lack access to centralised power grids. By integrating renewable energy systems, these regions can overcome energy poverty, enhance productivity and foster resilience aligning global sustainability goals with local socio-economic needs [11].

I.1.1 Background

Irrigation has traditionally relied on gravity fed canals, open channels, and manually operated pumps powered by fossil fuels. While these conventional systems were initially effective, they present major inefficiencies: substantial water losses through evaporation and infiltration, limited control over application rates, and high energy consumption. These shortcomings have driven research toward renewable energy based irrigation technologies that offer more sustainable and efficient water management solutions.

Since the 1970s, a large body of theoretical, numerical, and experimental studies has examined photovoltaic water pumping systems (PVPS) as a means of addressing both energy and water scarcity in agriculture. Pioneering investigations assessed the technical feasibility and economic potential of combining solar powered generation with hydraulic pumping. Their findings established the conceptual foundation for integrating a photovoltaic source with an electro hydraulic pumping unit, which later guided system optimisation and cost reduction research [12].

Despite considerable progress, the literature reveals a lack of large-scale experimental validation of photovoltaic irrigation systems. Most early works focused on analytical modelling and prototype simulations rather than field experimentation under real climatic conditions.

in 1998 proposed a cost-effective configuration in which a permanent magnet motor was directly powered by a photovoltaic array, eliminating the need for current and position sensors and thereby reducing overall system complexity and cost [13]. Subsequent researchers refined direct coupling control strategies for PV motors, achieving improved torque stability and water pumping performance under variable irradiance [14].

To determine optimal installation strategies researchers conducted a long term comparative study of different PV-driven pumping configurations. Their results showed that using a solar tracking mechanism significantly improved field efficiency, albeit with higher installation costs [15]. Similarly, in 2005 analysed the operational behavior of a positive displacement pump under different rotational speeds. They observed that, at higher speeds, the pump completed thirty one working stages during midday hours, while at lower speeds it operated with forty six stages yielding an increased total volume of approximately 9800 m^3 of water [16].

In subsequent years, the optimisation of photovoltaic pumping systems became a key area of investigation. An applied design optimisation methods to meet domestic and agricultural water needs in rural Kuwait. The resulting 0.21 kW system supplied 12 m^3 of water per day for 300 people, demonstrating the technical and economic viability of small-scale PV

pumping [17].

For developing an hourly simulation model for seven PV array configurations over a one year period. Their results indicated that increasing the array size increased the pumped water volume and subsystem efficiency, although excessive scaling reduced conversion efficiency [18]. following that further optimised PV-pump systems by incorporating parameters such as irrigation demand, soil moisture content, evapotranspiration, rainfall efficiency, solar irradiance, ambient temperature, and groundwater depth [19].

next a compared of two pumping configurations: a centrifugal pump driven by a three phase induction motor and a positive displacement pump powered by a DC motor. Their findings showed that the DC system achieved superior hydraulic efficiency and reliability under arid conditions [20].

Subsequent studies examined environmental factors influencing PV performance. compiled an extensive database of hourly solar radiation and temperature measurements for performance modelling [21]. then an implemented a water spraying technique to cool PV surfaces, achieving notable gains in efficiency and system economy [22]. in 2010 a proposed hybrid cooling strategy using pump circulated water to mitigate thermal losses and enhance optical absorption, confirming that larger PV modules exhibit lower temperature sensitivity [23].

After that studying the effect of dust accumulation on PV modules using controlled sand and clay deposits. They recorded up to an 18 % reduction in power output in uncleaned modules, highlighting the necessity of periodic maintenance in desert environments [24]. Then compared two PV panel configurations parallel and series reported significant performance differences under high irradiance conditions [25].

in 2013 designed a 1.5 kW PV-driven pumping system and compared its life-cycle cost to that of a diesel powered alternative, concluding that solar pumping is economically superior over the long term [26]. completing the work with corroborate these findings through real installations in Mexico and India, where PV systems achieved payback periods of four to six years and service lifespans exceeding twenty years [27].

Economic assessments were expanded using the RETScreen simulation platform, which demonstrated annual energy savings of 7–8 MWh for a 4.48 kW PV motor–pump configuration [28].Furthermore, an optimised PVPS design for rural Oman, comprising 0.84 kW modules, a 0.8 kW converter, and 12 V / 200 Ah battery storage. Their study estimated an energy cost of 0.309 USD kWh^{-1} significantly lower than diesel-based systems at 0.79 USD kWh^{-1} [29].

More recent research integrates intelligent management and control algorithms into PV irrigation systems by developing a real-time management framework linking solar energy availability with irrigation water demand, incorporating soil moisture balance and hydraulic network behavior [30]. Then this approach extended with a multi sector optimisation model that enables concurrent operation of several irrigation zones to maximise energy use efficiency [31].

Despite these advancements, many farms lack the topographical conditions required for gravity fed reservoirs. Booster stations are therefore necessary to provide adequate pressure for uniform water distribution noted that such infrastructure requirements significantly influence the technical feasibility and cost effectiveness of PV irrigation projects [32].

Finally demonstrating sprinkler irrigation, which applies water through pressurised nozzles that simulate rainfall, enhances microclimate regulation, crop yield, and water use efficiency [33], confirmed that sprinkler systems can be automated to improve uniformity and scheduling [34]. Field experiments showed reduced canopy temperatures and improved vapor pressure profiles under sprinkler irrigation [35]. At the farm scale, this technology reduces labor requirements and promotes agricultural intensification, while at the community scale, it ensures more reliable and equitable water distribution concluded that the full benefits of sprinkler irrigation are achieved when integrated into a comprehensive farm-management framework [36].

This thesis demonstrates that intelligent photovoltaic pumping can be considered a credible and practical solution for autonomous irrigation. The work addressed the problem from both the energy side and the irrigation side. For the DC prototype, the results confirmed that fuzzy MPPT control can effectively maximise photovoltaic energy extraction with a low-cost embedded platform. For the AC prototype, the results showed that variable-speed regulation and sensor feedback can improve hydraulic management and reduce cumulative energy consumption. Taken together, these results support the idea that photovoltaic irrigation systems should not be designed as simple power-supply substitutions. They should be conceived as integrated systems in which energy conversion, pumping behavior, and irrigation demand are coordinated. As for future work, several directions can extend this research: the integration of hybrid renewable sources, the use of predictive and AI-based control methods, and the deployment of IoT supervision for larger-scale field applications. Thus, the thesis not only validates a prototype but also opens a pathway toward smarter and more sustainable irrigation systems for agriculture in arid regions.

I.2 Irrigation in Modern Agriculture

Irrigation represents a fundamental component of modern agricultural practice, serving as a controlled and artificial supply of freshwater to croplands in order to sustain and enhance plant growth. It effectively functions as an artificial form of precipitation that compensates for the irregularity of natural rainfall, particularly in arid and semi-arid climates. Modern irrigation systems, ranging from manually operated setups to highly automated sprinkler and drip systems, play a crucial role in ensuring consistent water availability and optimal soil moisture levels, thereby promoting efficient crop development and yield stability.

Beyond simple water provision, irrigation also contributes to soil conservation and land reclamation, supporting the restoration of degraded ecosystems and stabilising landscapes exposed to erosion. Automated systems are increasingly preferred for their precision and water-use efficiency, yet traditional manual methods remain in use where technological resources are limited.

The importance of irrigation extends beyond agronomy, influencing food security, economic resilience, and environmental sustainability. By regulating soil–plant–water dynamics, irrigation mitigates the adverse impacts of water scarcity, excessive drainage, or groundwater depletion—phenomena commonly encountered in arid regions. Thus, irrigation is not only a technique for enhancing agricultural productivity but also a strategic tool for sustainable land management and climate adaptation [37, 38].

I.3 Automated Irrigation System in Cultivated Land

Automated irrigation systems represent a transformative evolution in agricultural water management, designed to provide fresh water to crops at regular intervals while optimizing resource efficiency. Such systems integrate hydraulic, electronic, and control technologies to regulate water delivery with precision according to soil moisture and plant requirements.

These systems encompass multiple irrigation methods—surface, subsurface, sprinkler, and drip—each adapted to specific soil types, crop varieties, and climatic conditions. Water may be distributed through open channels or pressurised piping networks and can be enriched with nutrients to support fertigation practices, enhancing plant growth while minimising waste.

Traditional irrigation relied primarily on open canal systems for water distribution, an approach that, while effective historically, suffers from substantial inefficiencies due to water loss from infiltration and evaporation. As a result, modern agricultural practices increasingly favour closed-loop or pressurised systems equipped with automated control and monitoring

technologies. These advanced configurations allow real-time adjustment of irrigation schedules based on sensor feedback, meteorological inputs, and crop growth stages.

Among these modern systems, sprinkler and drip irrigation are the most prevalent in cultivated lands. Sprinkler systems deliver water in a manner analogous to natural rainfall, thereby avoiding over-saturation and protecting fragile seedlings. Drip systems, by contrast, supply water directly to the root zone, significantly improving water-use efficiency and minimising losses through evaporation or run-off.

For an irrigation system to operate efficiently, the interaction between soil, water, and plant physiology must be thoroughly understood and quantified. Therefore, modern irrigation management incorporates sensor-based feedback loops, programmable logic controllers (PLCs), and wireless data transmission systems that enable precise control of timing, duration, and water volume application.

These innovations mark the transition from conventional, labour-intensive irrigation to intelligent, self-regulating agricultural infrastructure, paving the way for smart farming systems capable of adaptive water management under variable climatic and soil conditions [39].

I.4 Types of Irrigation

Irrigation systems can source water from a wide variety of natural and engineered reservoirs including rivers, lakes, groundwater wells, wastewater treatment facilities, and seawater desalination plants. These sources supply irrigation networks that may operate under gravity flow through open channels or under pressure through pipelines, depending on the topography and water quality requirements.

Historically, human civilisations have practised irrigation for more than 5,000 years, evolving from simple gravity-fed canals to sophisticated pressurised and automated systems that integrate sensor-based feedback control. This evolution has been driven by the need to balance water efficiency, energy consumption, and crop productivity [40, 41].

I.4.1 Manual Irrigation

Manual irrigation Figure I.1 [42] refers to the direct application of water by human effort, whether using simple tools such as buckets, hoses, or watering cans. Although this technique offers flexibility for small-scale cultivation and nursery operations, it is largely impractical for large agricultural areas due to its intensive labour requirements and inconsistent water distribution.

Studies indicate that manual irrigation lacks the precision and uniformity required for commercial-scale agriculture, often resulting in uneven moisture profiles, inefficient water usage, and increased susceptibility to plant stress. Consequently, it is now mainly restricted to small gardens, experimental plots, and regions lacking infrastructure for mechanised irrigation [43].



Figure I.1: Manual irrigation using a watering can for small-scale crop watering.

I.4.2 Surface Flow (Gravity) Irrigation

Surface or gravity irrigation Figure I.2 [44] relies on the natural gravitational flow of water through open canals and field channels to distribute water across cultivated plots. Main channels convey water to secondary and tertiary networks that deliver it to the fields. While this system is simple and inexpensive, it suffers from significant inefficiencies due to infiltration, percolation, and evaporation losses, particularly in hot and arid climates.

The absence of pressurisation and limited control over flow distribution make this technique unsuitable for precision water management or heterogeneous soils. Nevertheless, gravity-fed irrigation remains prevalent in traditional agricultural systems where energy availability or infrastructure is limited [45].



Figure I.2: Surface (gravity) irrigation through open channels and field ditches.

I.4.3 Sprinkler Irrigation

Sprinkler irrigation Figure I.3[46] simulates natural rainfall by distributing water under pressure through a network of pipes and sprinklers. Water is pumped and atomised into fine droplets that fall uniformly over the cultivated surface, promoting even soil wetting and optimal aeration.

System performance depends critically on nozzle design, pressure regulation, and climatic conditions such as wind and temperature, which influence droplet dispersion and evaporation rates. Sprinkler systems are ideal for a wide variety of crops and terrains, offering flexibility and control in both small-scale and industrial applications.

Proper design must ensure uniform water distribution and minimise energy losses, taking into account the hydraulic s of the pump and the irrigation grid. As such, sprinkler irrigation represents a balance between mechanical sophistication and agronomic precision [47].



Figure I.3: Sprinkler irrigation system delivering pressurised water uniformly .

I.4.4 Micro-Irrigation (Drip Irrigation)

Drip or micro-irrigation Figure I.4 [48] is the most water-efficient irrigation technique, delivering precise quantities of water and nutrients directly to the plant root zone. This system minimises losses from evaporation, deep percolation, and surface run-off by maintaining slow, localised discharge through emitters or micro-tubes either above or below the soil surface[49].

Micro-irrigation enables precise control over soil moisture and fertigation, significantly improving water-use efficiency and crop productivity. Its adoption is expanding globally due to its compatibility with renewable energy sources such as photovoltaic-powered pumps, making it a cornerstone of sustainable irrigation in arid regions [50].



Figure I.4: Drip irrigation system supplying water directly to plant root zones.

I.4.5 Precision Irrigation

Precision irrigation Figure I.5 [51] represents the most advanced stage of irrigation technology, integrating data-driven control, real-time sensing, and predictive analytics to optimise water use at plant-specific and spatially variable scales. By employing soil moisture sensors, weather stations, and satellite-based monitoring, these systems dynamically adjust irrigation schedules and volumes to crop needs.

This approach enables localised management of water and nutrients, thus enhancing yield while minimising environmental impacts such as salinity accumulation or nutrient leaching. Automated sprinkler or drip networks are often employed in precision irrigation, coordinated by computer algorithms or AI-based decision systems.

Although the capital investment and technical expertise required are higher than for conventional methods, precision irrigation is increasingly recognised as a key enabler of sustainable intensification in both field and horticultural production systems [52, 53].



Figure I.5: Precision irrigation system integrating sensor feedback and automated control for optimised water application .

I.4.6 Statement of the Problem

The global water crisis represents one of the most urgent challenges of the twenty first century. Population growth, climate variability, and the over exploitation of groundwater resources have severely increased pressure on agricultural water supplies. As agriculture consumes more than 70% of the world's available freshwater, improving irrigation efficiency has become a strategic priority for achieving global food security and environmental sustainability. At the same time, the agricultural sector faces persistent energy shortages, particularly in rural and off grid regions where access to conventional electricity is limited or unreliable. Consequently, photovoltaic (PV) powered irrigation systems have emerged as a viable alternative for providing water in an environmentally responsible and energy independent manner.

Despite their promise, PV water pumping systems have not yet achieved widespread adoption. Their diffusion is constrained by relatively low energy conversion efficiency and high installation costs per watt compared with diesel powered systems. Moreover, conventional irrigation management often leads to excessive water consumption and suboptimal energy utilisation due to a lack of automation and intelligent feedback control. These limitations highlight the need for integrated solutions that improve both hydraulic and electrical efficiency maximising water productivity while minimising energy consumption[54].

Recent advances in smart irrigation systems have demonstrated that incorporating sensor networks, data driven decision algorithms, and adaptive control mechanisms can drastically enhance the sustainability of irrigation practices. Smart irrigation enables real-time monitoring of soil moisture, temperature, and solar radiation, allowing precise water delivery only when and where it is needed. When powered by photovoltaic systems, such intelligent control not only conserves water but also significantly reduces overall energy use by synchronising pump operation with renewable power availability. However, the efficiency of these systems still depends critically on the ability of the PV array to operate at its maximum power point under varying environmental conditions.

The central technical challenge, therefore, lies in ensuring optimal power extraction from PV modules while maintaining adaptive irrigation control. Conventional maximum power point tracking (MPPT) algorithms such as perturb and observe or incremental conductance techniques often exhibit slow transient response, poor steady state accuracy, and oscillations around the optimal point. These weaknesses reduce both electrical efficiency and irrigation system reliability, limiting the applicability of PV powered smart irrigation systems in real world agricultural environments[55].

To overcome these limitations, this research proposes an intelligent control strategy based

on a fuzzy logic MPPT algorithm implemented on an Arduino Mega microcontroller. Fuzzy logic, as a branch of artificial, enables adaptive and heuristic decision making under uncertain conditions by mimicking human reasoning. Integrated into the PV pumping system, the proposed controller enhances dynamic response, minimises power oscillations, and maintains continuous maximum power extraction. Furthermore, by coupling this control with real-time irrigation feedback, the system contributes to significant water savings, reduced energy consumption, and optimised pump operation.

Beyond its technical contributions, this study addresses the broader issue of sustainable resource management by uniting renewable energy generation with precision water use. The developed fuzzy logic based MPPT controller provides a low-cost, scalable, and autonomous solution for rural agriculture, capable of improving both water use efficiency and energy productivity.

In summary, the central problem can be articulated as follows: How can intelligent control and smart irrigation control strategies specifically a fuzzy logic based MPPT algorithm implemented on an embedded Arduino platform be designed and optimised to maximise energy efficiency, water savings, and operational stability in photovoltaic water pumping systems under variable environmental conditions? Addressing this problem contributes simultaneously to advancing intelligent renewable energy control and mitigating global water scarcity through sustainable, energy efficient irrigation technologies.

I.4.7 Objectives

The objectives of this thesis entitled Study and Realisation of a Photovoltaic Pumping Installation Prototype for Irrigation in the Field of Agriculture are as follows:

Maximise Energy Production

The primary objective is to develop a system that optimises the energy production from photovoltaic (PV) panels by implementing a fuzzy logic maximum power point tracking (MPPT) controller. This is particularly important under varying weather conditions and solar irradiance levels.

Find a Low Cost Solutions

The study aims to demonstrate that the fuzzy logic controller, when implemented on a low-cost Arduino Mega microcontroller, can effectively monitor and control the PV

pumping system. The goal is to provide an economical solution for energy management in isolated areas.

Real-Time Control and Monitoring

Another objective is to create a system that allows for real-time monitoring and responsive control of the PV panels output. This involves using voltage and current sensors to feed data into the fuzzy controller for continuous adjustment of the system's performance.

Reduce System Oscillations

The study aims to show that the fuzzy logic controller can minimise oscillations in the system, providing a stable operational performance despite fluctuations in ambient conditions, such as temperature and irradiance.

Improve Irrigation System Efficiency

An additional objective is to evaluate and improve the efficiency of the pumping system for irrigation powered by the PV setup, ensuring that it can reliably operate while delivering optimal performance under varying environmental conditions.

Experimental Validation

The research also seeks to provide experimental validation of the proposed control approach and demonstrate how it effectively tracks the maximum power point while managing output voltage stability.

These objectives collectively highlight the goal of enhancing the functionality and efficiency of small and large scale PV energy systems for applications in areas with limited access to traditional power sources.

I.4.8 Thesis Contributions

M. Laaouad and A. Guergazi, "Implementation of Fuzzy Logic MPPT Based on Arduino in Small-Scale PV Pumping System," *International Journal of Power Electronics and Drive Systems*, vol. 15, no. 1, pp. 192–200, 2024. doi: 10.11591/ijpeds.v15.i1.pp192-200.

M. Laaouad and A. Guergazi, "Design and Application of Fuzzy Logic on Arduino Mega MPPT Using MATLAB/Simulink," in *Proceedings of the 2nd World Energy Storage Conference (WESC-2022)*, Istanbul, Turkiye, Dec. 18–21, 2022.

M. Laaouad and A. Guergazi, "Arduino Mega-Based Fuzzy Logic Controller for Photovoltaic Systems," in *IEEE 1st International Conference on Renewable Solutions For Ecosystems Toward a Sustainable Energy Transition (ICRSEtoSET 2023)*, Djelfa, Algeria, May 6–7, 2023. doi: 10.1109/ICRSEtoSET56772.2023.10525434.

I.4.9 Thesis Outlines

This doctoral thesis provides background information about grassland irrigation experienced in Biskra-Algeria and PVWP system. This thesis consists of the following chapters:

- Chapter 1 Introduction and Literature Review

  Introduce the thesis background as the irrigation system side, knowledge gaps and challenges, objectives, contributions and thesis outline.

- Chapter 2 Model Presentation of the Direct Photovoltaic Irrigation Systems

  Demonstrate the PV systems components, including the photovoltaic module, DC-DC converter, DC-AC inverter, and pumping units

- Chapter 3 Developed Techniques

  Description of the applied structure for DC and AC systems,Methodology of control,irrigation control algorithm flowchart

- Chapter 4 Implementation and Results

  Present the tests benches and experimentally validate the control methods developed in this thesis. They are associated with energy management strategies of the system for irrigation on an agricultural area.

I.5 Conclusion

This chapter has provided a comprehensive overview of the evolution, current state, and challenges of photovoltaic (PV) water-pumping systems for irrigation applications. It began by situating the research within the broader context of global energy transitions and agricultural sustainability, emphasising the dual challenges of water scarcity and energy dependence in

rural areas. Through a detailed review of prior studies, we examined the main technological advances in PV pumping systems from early feasibility studies and component optimisation to modern intelligent and hybrid control approaches with irrigation types.

The literature analysis revealed that, although significant progress has been made in the design and control of photovoltaic irrigation systems, several limitations persist. Chief among these are the relatively low energy conversion efficiency of PV modules under variable weather conditions, the limited adoption of adaptive control techniques, and the scarcity of experimental validation in real agricultural settings. Furthermore, traditional irrigation practices still lack automation and energy synchronisation with renewable sources, leading to inefficiencies in both water use and energy consumption. Beyond the literature analysis, this chapter explored modern irrigation technologies that integrate automation and precision control. The discussion encompassed traditional, semi-automated, and fully automated irrigation networks capable of adjusting water delivery in real time according to soil moisture and meteorological data acquired from sensors. Such smart irrigation systems ensure optimal water use efficiency, prevent over irrigation, and support sustainable agricultural production.

To address these issues, this research introduces an intelligent control approach based on fuzzy logic maximum power point tracking (MPPT) implemented on an Arduino Mega microcontroller. The aim is to enhance the dynamic performance and energy yield of PV-driven irrigation systems while ensuring efficient water management through smart irrigation control. This approach integrates renewable energy generation with precision agriculture, providing a low-cost, autonomous, and sustainable solution suitable for rural environments.

Building upon the identified research gaps, the subsequent chapter (**Chapter 2**) presents the structural and mathematical models of the two direct photovoltaic irrigation configurations under study:

- **System 1:** Direct AC-Coupled PV Irrigation System (PV–Inverter–AC Load, Without Storage);
- **System 2:** Direct DC-Coupled PV Irrigation System (PV–DC/DC Converter–DC Load, Without Storage).

The next chapter develops these system models in detail, establishing the analytical framework that will serve as the foundation for the control design, simulation, and experimental validation presented in the later chapters.

Chapter II

MODEL PRESENTATION OF DIRECT PHOTOVOLTAIC IRRIGATION SYSTEMS

Introduction

The modelling of photovoltaic (PV) irrigation systems represents a fundamental step toward understanding and evaluating their operational behavior under varying solar conditions. Accurate modelling enables the prediction of system responses to dynamic environmental inputs and supports the optimisation of design parameters for efficient energy–water conversion. In this context, the present chapter is dedicated to the structural and mathematical presentation of two direct PV configurations developed for irrigation applications. The objective is to establish representative models for each configuration, enabling the analysis of their energy conversion chains from solar radiation to hydraulic output. Such a modelling approach provides the theoretical framework required for subsequent simulation, control, and experimental validation.

The two systems under consideration are defined as follows:

- **System 1 – Direct AC-Coupled PV Irrigation System (Without Storage):** This configuration consists of photovoltaic panels connected to a DC–AC inverter that supplies an alternating current load, typically an AC motor driving a centrifugal pump. The absence of energy storage ensures a direct conversion of solar energy into mechanical pumping power, operating instantaneously according to the available solar irradiance. This topology is advantageous for applications requiring high motor torque and com-

patibility with standard AC equipment, but its performance is directly dependent on solar intermittency.

- **System 2 – Direct DC-Coupled PV Irrigation System (Without Storage):** This configuration integrates photovoltaic panels with a DC–DC converter that directly powers a DC load, such as a DC moto-pump. The system provides a simplified conversion path and higher efficiency under variable solar input, without the inclusion of any intermediate storage device. It offers improved matching between the PV generator and the hydraulic load through dynamic voltage and current control, which enhances the overall energy utilisation efficiency.

In both configurations, the elimination of intermediate storage elements (such as batteries) reduces system cost, maintenance, and energy losses, thereby promoting sustainable and autonomous irrigation operation in remote or off-grid locations.

This chapter presents the physical structure and functional interconnections of both systems, followed by the mathematical models describing each subsystem namely:

- the photovoltaic generator .
- the power conversion stages (DC–DC converter and DC–AC inverter).
- electromechanical pumping unit.

The modelling equations are developed to characterise the energy transformation processes occurring along the conversion chain, from solar irradiance to mechanical water pumping power. The formulation also incorporates electrical and hydraulic efficiencies, enabling an integrated evaluation of overall system performance under dynamic solar conditions.

Through this model-based presentation, the operational principles and performance defining relationships of both AC and DC PV irrigation configurations are systematically detailed, forming the analytical foundation for subsequent performance analysis and control studies. This foundation will later support the validation of experimental data and the design of intelligent control strategies aimed at maximising energy extraction and water delivery efficiency.

II.1 Photovoltaic Array Components

Photovoltaic (PV) arrays constitute the primary energy conversion interface in solar-driven irrigation systems. They are assembled from multiple PV modules interconnected in series and/or parallel to achieve the required voltage and current levels compatible with the

downstream power conditioning units. Each module, in turn, comprises several photovoltaic cells that operate as the fundamental semiconductor devices converting solar irradiance into electrical power.

The interconnection configuration series, parallel or hybrid depends on the electrical specifications of the power conversion stage, such as the DC–DC converter or inverter input characteristics, ensuring optimal energy transfer efficiency and operational stability [56].

The general structure of a PV array is depicted in Figure II.1, illustrating the hierarchical organisation from individual cells to the complete array.

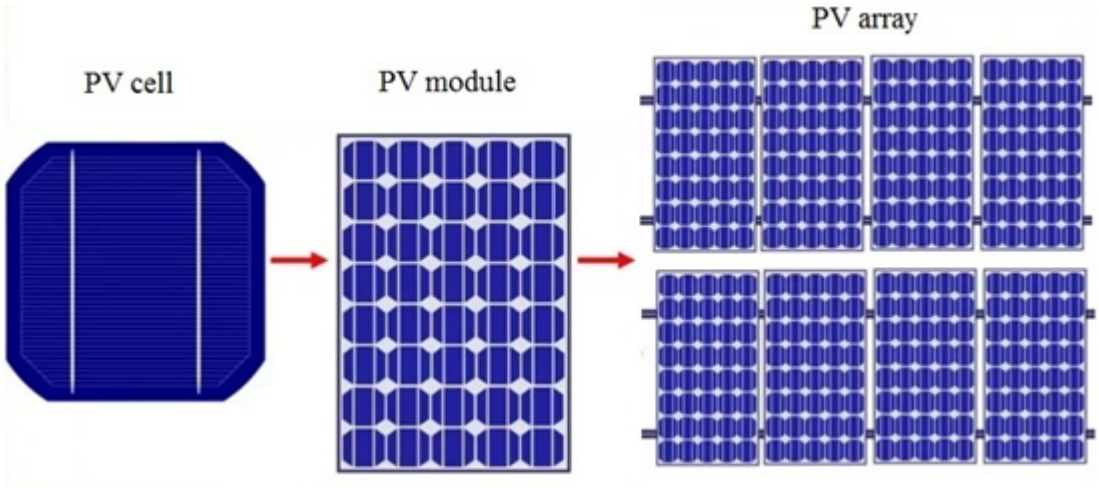

Figure II.1: PV array structure.

II.2 Photovoltaic Cell

A photovoltaic cell directly converts solar radiation into electrical energy through the photovoltaic effect, which occurs at the junction of semiconductor materials. The non-linear current–voltage (I–V) characteristics of a PV cell are strongly influenced by solar irradiance and temperature, leading to significant variations in output performance under fluctuating environmental conditions.

To describe this behavior, several equivalent electrical circuit models have been proposed in the literature. Among these, the single diode model has gained widespread acceptance due to its balance between simplicity and accuracy in representing real PV cell dynamics [57][58].

As shown in Figure II.2, the PV cell is modelled as a photocurrent source connected in parallel with a diode, a shunt resistance (R_{Sh}), and a series resistance (R_S). This configuration effectively captures both the ideal and non-ideal loss mechanisms of the cell, including

leakage currents and internal resistive losses.

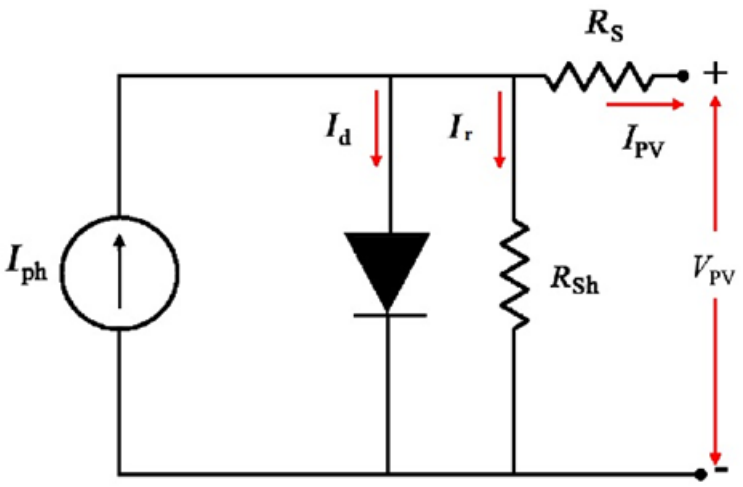

Figure II.2: Equivalent circuit of a photovoltaic cell.

The mathematical expression describing the current–voltage behavior of the PV cell, according to the single diode model, is given by:

$$\begin{aligned} I_{pv} &= I_{ph} - I_d - I_r \\ &= I_{ph} - I_0 \left(e^{\frac{V_{pv}+R_S I_{pv}}{nV_t}} - 1 \right) - \frac{V_{pv} + R_S I_{pv}}{R_{Sh}} \end{aligned} \tag{II.1}$$

where:

- I_{pv} – cell output current (A).
- I_{ph} – photocurrent generated by incident irradiance (A).
- I_d – diode current following the Shockley equation (A).
- I_r – shunt leakage current (A).
- I_0 – diode reverse saturation current (A);
- V_{pv} – cell output voltage (V).
- R_S – series resistance representing internal ohmic losses (Ω).
- R_{Sh} – shunt resistance representing leakage paths (Ω).

- n – diode ideality factor (dimensionless).
- V_t – thermal voltage defined as:

$$V_t = \frac{kT}{q} \tag{II.2}$$

where: k is the Boltzmann constant ($1.38 \times 10^{-23}\ J/K$), T is the absolute temperature (K), and q is the elementary electronic charge ($1.6 \times 10^{-19}\ C$) [59].

This model provides the analytical foundation for simulating PV module and array performance under varying irradiance and temperature conditions, thereby supporting system-level design and optimisation in photovoltaic irrigation applications.

II.3 Photovoltaic Module

Individual photovoltaic (PV) cells generate relatively low voltage and current, typically on the order of 0.5–0.7 V per cell and a few amperes under standard conditions. To obtain usable power levels suitable for practical applications, these cells are electrically interconnected in series and/or parallel to form a photovoltaic module.

Series connection increases the total output voltage by summing the voltages of the constituent cells, while parallel connection increases the current capacity by summing their currents. The resulting configuration allows the module to deliver the rated power required by the intended load or power conditioning system.

PV modules are characterised and rated under Standard Test Conditions (STC), defined at an irradiance of 1000 W/m^2, a cell temperature of 25°C, and an air mass (AM) of 1.5. These standardised conditions facilitate comparison of module performance across different technologies and manufacturers.

The equivalent electrical circuit of a PV module is illustrated in Figure II.3. Assuming identical cells, the overall current–voltage (I–V) behavior of the module can be derived by extending the single diode model to account for the interconnection of N_s series-connected cells and N_p parallel-connected cell strings [60]. The corresponding non-linear equation governing the module's output current is expressed as:

$$I_{pv} = N_p I_{ph} - N_p I_0 \left(e^{\frac{N_p V_{pv} + (N_s/N_p) R_S I_{pv}}{n N_p V_t}} - 1 \right) - \frac{N_p V_{pv} + (N_s/N_p) R_S I_{pv}}{(N_s/N_p) R_p}$$

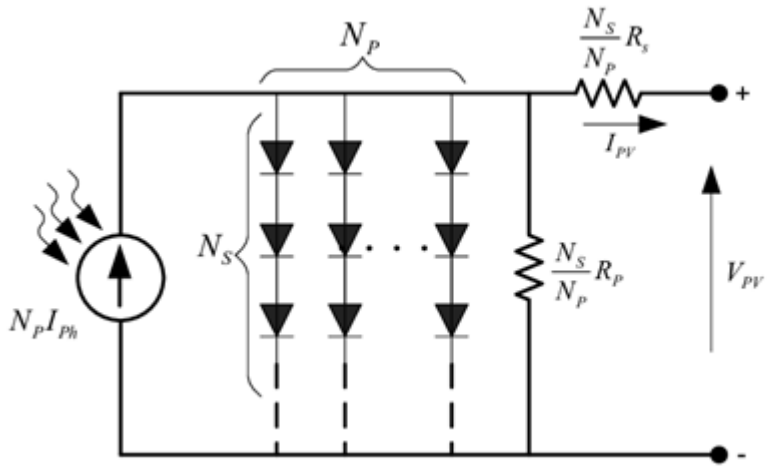

Figure II.3: Equivalent circuit of a photovoltaic module.

where:

- I_{pv} – output current of the PV module (A);
- V_{pv} – output voltage of the PV module (V);
- N_s – number of PV cells connected in series;
- N_p – number of PV cells connected in parallel.

This model effectively represents the aggregated electrical response of multiple cells within a single module, accounting for the internal resistive effects and exponential diode characteristics inherited from individual cell behavior. It forms the foundation for the subsequent modeling of photovoltaic arrays and system-level performance evaluation.

II.4 Meteorological Influences on PV Modules

The performance of photovoltaic (PV) modules is inherently governed by meteorological conditions, which directly influence the energy conversion process. Solar irradiance (G) represents the dominant driving parameter, determining the amount of incident radiant energy available for conversion into electrical power [61]. However, irradiance levels fluctuate dynamically due to variations in cloud cover, atmospheric turbidity, seasonal cycles, and the presence of aerosols or dust particles, all of which induce substantial power fluctuations in PV systems [62].

Temperature constitutes a secondary yet crucial factor, as elevated cell or ambient temperatures increase semiconductor carrier recombination and internal resistive losses, thereby reducing conversion efficiency. Conversely, convective wind flow can enhance surface cooling, partially mitigating the thermal effects and improving instantaneous output performance [63]. Hence, the overall PV module behavior is the result of a complex and transient interaction between solar irradiance, temperature, and wind dynamics.

II.4.1 Impact of Irradiation (G)

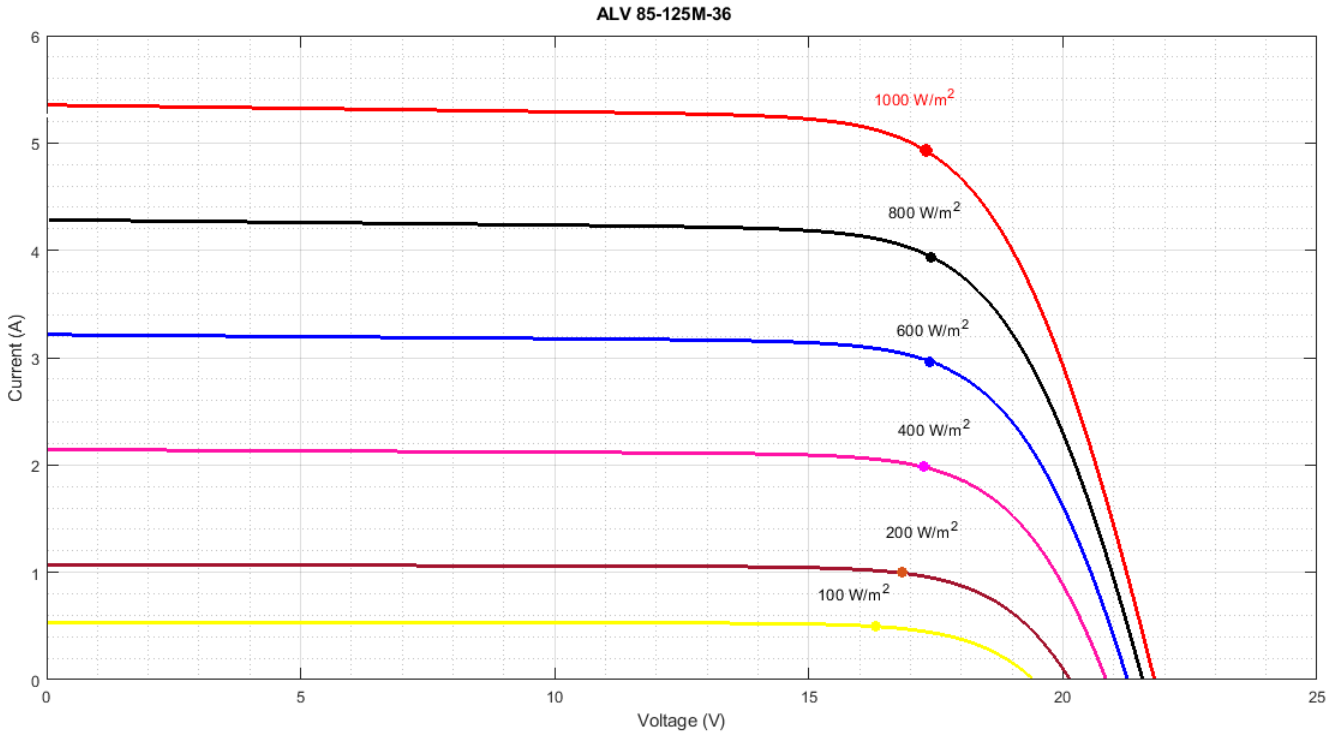

Figure II.4: Current–voltage characteristics of the photovoltaic module at different irradiance levels ($T_c = 25°C$).

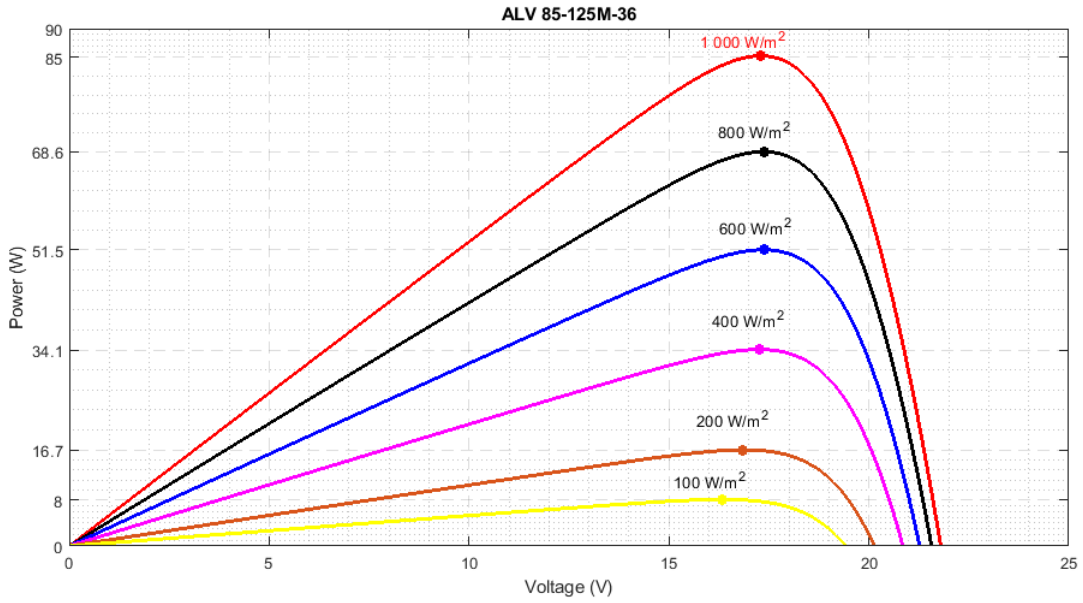

Figure II.5: Power–voltage characteristics of the photovoltaic module at different irradiance levels ($T_c = 25°C$).

Figures II.4 and II.5 illustrate the current–voltage and power–voltage characteristics of a photovoltaic module for varying irradiance levels at constant cell temperature. It is evident that the open-circuit voltage (V_{oc}) exhibits only a minor increase with irradiance, whereas the short-circuit current (I_{sc}) and the corresponding output power increase almost linearly with the level of solar illumination.

This behavior arises because the photocurrent component is directly proportional to the number of incident photons absorbed by the cell, while the voltage is logarithmically dependent on the photocurrent, resulting in a smaller rate of change. Consequently, the maximum power point (MPP) shifts toward higher current values with increasing irradiance, emphasising the importance of adaptive power tracking algorithms for optimal system efficiency.

II.4.2 Impact of Temperature (T_c)

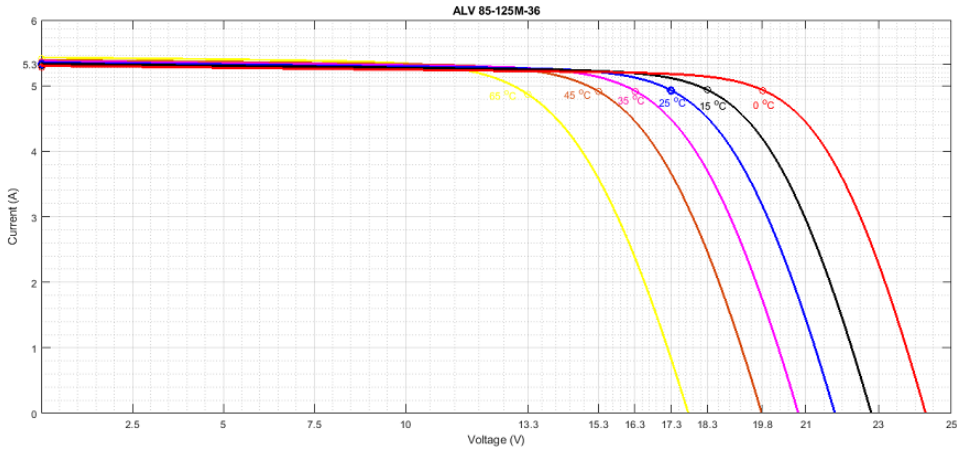

Figure II.6: Current–voltage characteristics of the photovoltaic module for varying temperatures ($T_c = 0, 15, 25, 35, 45, 65°C$) at $E = 1000\ W/m^2$.

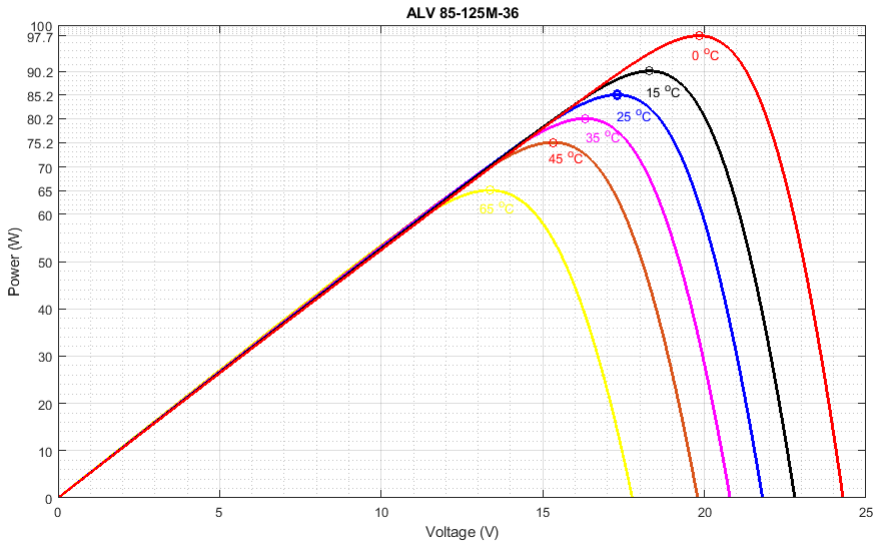

Figure II.7: Power–voltage characteristics of the photovoltaic module for varying temperatures ($T_c = 0, 15, 25, 35, 45, 65°C$) at $E = 1000\ W/m^2$.

Figures II.6 and II.7 demonstrate the temperature dependent behavior of the PV module at constant irradiance. As temperature increases, the open-circuit voltage (V_{oc}) and the maximum power output (P_{max}) decrease markedly, while the short-circuit current (I_{sc}) experiences a slight increase.

This trend results from the temperature induced reduction of the semiconductor bandgap, which increases the intrinsic carrier concentration and diode reverse saturation current, leading to a lower terminal voltage for a given current. The marginal rise in I_{sc} is attributed to enhanced carrier mobility at elevated temperatures, although this effect is minor compared to the voltage degradation. Overall, thermal influence causes a leftward and downward shift of the I–V and P–V curves, underscoring the need for adequate module cooling and temperature compensation in PV system design.

II.5 Electronic Power Converters

Power electronic converters are fundamental components in photovoltaic (PV) energy systems, providing the necessary interface between the variable DC output of PV arrays and the AC power required by electrical loads or the grid. Owing to their high controllability, efficiency, and adaptability to changing environmental conditions, these converters have received growing attention in recent years. Since the electrical output of a PV array depends strongly on solar irradiance and temperature, it exhibits a fluctuating DC voltage that cannot directly supply AC loads. Consequently, the integration of DC–DC and DC–AC conversion stages is essential to ensure stable and efficient energy conversion from the PV source to the load [64].

II.5.1 DC–DC Boost Converter

The DC–DC converter plays a crucial role in maintaining the PV array at its maximum power point (MPP), thereby ensuring optimal energy extraction. Among the various topologies, the boost converter is widely adopted due to its structural simplicity, ease of control, and capability to increase the output voltage while providing a continuous input current. It also serves as the interface for implementing maximum power point tracking (MPPT) algorithms.

The boost converter typically consists of an inductor, a power semiconductor switch (MOSFET or IGBT), a diode, and an output capacitor. Figure (II.8) illustrates the schematic diagram of the converter, along with the current and voltage waveforms corresponding to the switch conduction (on) and cut-off (off) intervals for the ideal case [65].

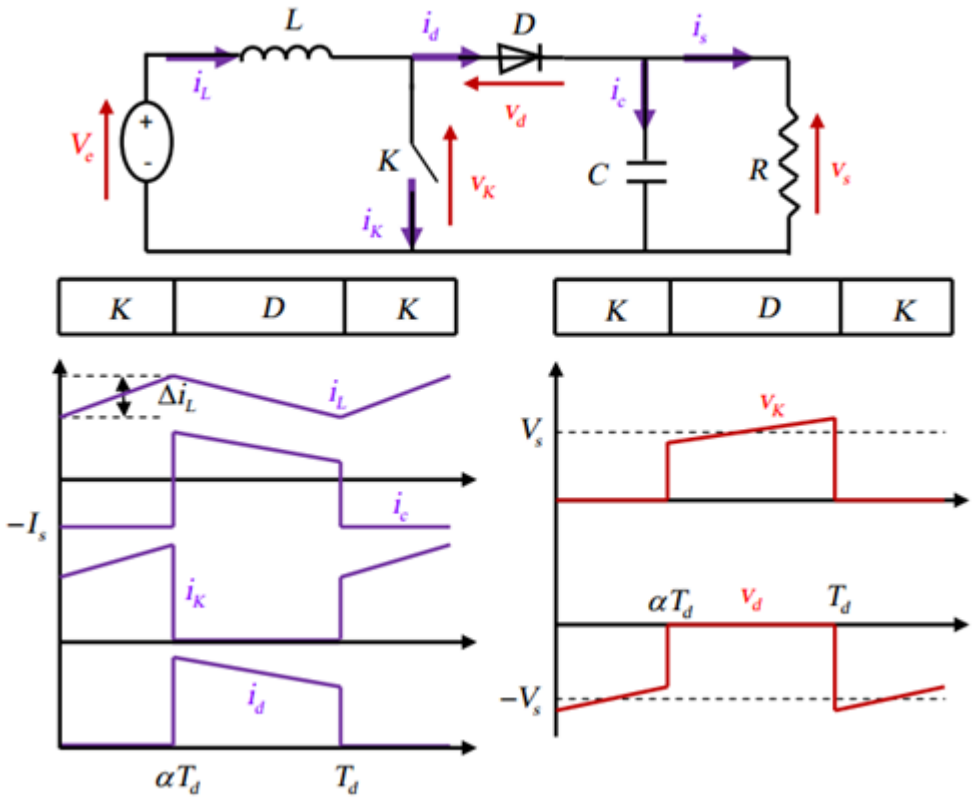

Figure II.8: Waveforms of currents and voltages in the boost converter.

When the switch K is turned *on*, the inductor stores energy from the input source, and the circuit operation is governed by:

$$L\frac{di_L}{dt} = V_e \tag{II.3}$$

Thus, the inductor current increases linearly according to:

$$i_L = I_{min} + \frac{V_e}{L}t \tag{II.4}$$

At $t = \alpha T_d$, the inductor current reaches its maximum value:

$$I_{max} = I_{min} + \frac{V_e}{L}\alpha T_d \tag{II.5}$$

When the switch K is turned *off*, the stored energy in the inductor is transferred to the load through the diode, and the system equation becomes:

$$L\frac{di_L}{dt} = V_e - V_s \tag{II.6}$$

$$i_L = I_{max} + \frac{V_e - V_s}{L}(t - \alpha T_d) \tag{II.7}$$

At $t = T_d$, the inductor current returns to its minimum value:

$$I_{min} = I_{max} + \frac{V_e - V_s}{L}(1 - \alpha)T_d \tag{II.8}$$

The ripple of the inductor current is given by:

$$\Delta i_L = I_{max} - I_{min} \tag{II.9}$$

From the steady-state condition (volt-second balance), the average output voltage V_s can be expressed as:

$$V_s = \frac{V_e}{1 - \alpha} \tag{II.10}$$

This expression indicates that the output voltage can be controlled by adjusting either the input voltage or the duty cycle α (where $0 < \alpha < 1$). Hence, the boost converter effectively functions as a voltage elevator. Applying the power balance principle between input and output allows expressing the average inductor current in terms of the output current:

$$I_L = \frac{I_s}{1 - \alpha} \tag{II.11}$$

Using Equation (II.5), the inductor current ripple is derived as:

$$\Delta i_L = \frac{\alpha V_e}{Lf} \tag{II.12}$$

where f denotes the switching frequency.

During the switch-on interval ($0 < t < \alpha T_d$), the output capacitor supplies energy to the load, resulting in:

$$C\frac{dV_s}{dt} = -i_s \tag{II.13}$$

Thus, the output voltage ripple can be expressed as:

$$\Delta V_s = \frac{\alpha V_e}{(1 - \alpha)RCf} \tag{II.14}$$

II.5.2 DC–AC Voltage Source Inverter

The DC–AC voltage source inverter (VSI) is responsible for converting the regulated DC voltage from the DC–DC stage into AC power suitable for grid connection or load supply. The conventional VSI topology comprises six insulated-gate bipolar transistors (IGBTs) arranged in a three phase bridge configuration. This structure allows bidirectional power flow and precise waveform synthesis through controlled switching sequences [66].

Figure (II.9) illustrates the typical VSI configuration, in which each leg corresponds to one phase. The complementary operation of the upper and lower switches in each leg minimises harmonic distortion and improves conversion efficiency compared to thyristor-based topologies [67]. The inverter is generally controlled by analog or digital modulation techniques, such as pulse width modulation (PWM), to adjust the effective output voltage and frequency according to load or grid requirements.

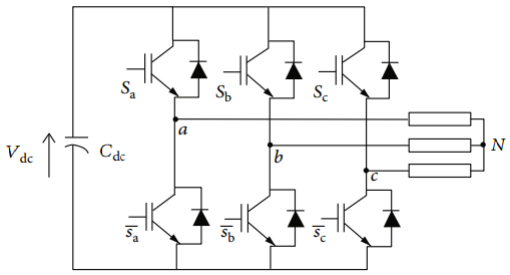

Figure II.9: Equivalent circuit of a three phase voltage source inverter.

Advanced PWM strategies, such as space vector modulation (SVM), have been extensively developed to enhance the harmonic performance, reduce switching losses, and improve the inverter's dynamic response [68]. The mathematical model of a three phase VSI can be represented by:

$$\begin{bmatrix} V_a \\ V_b \\ V_c \end{bmatrix} = \frac{V_{dc}}{3} \begin{bmatrix} 2 & -1 & -1 \\ -1 & 2 & -1 \\ -1 & -1 & 2 \end{bmatrix} \begin{bmatrix} S_a \\ S_b \\ S_c \end{bmatrix} \tag{II.15}$$

where S_a, S_b, and S_c represent the logical switching states of the corresponding inverter legs, and V_{dc} is the DC-link voltage. This matrix formulation facilitates the analysis of inverter output voltages and serves as the foundation for implementing advanced control strategies such as vector control and direct torque control.

II.6 Pump Unit

Electric motor–pump assemblies serve as the core of electro-hydraulic energy conversion, transforming electrical energy into hydraulic power with high precision and controllability. Electric motors paired with hydraulic pumps efficiently convert electrical energy into hydraulic power, with AC- and DC-driven units representing the two principal configurations, as illustrated in Figure (II.10). AC motor–pump systems are predominantly employed in high-power and industrial scale applications due to their robust construction, reliability, and compatibility with grid-supplied alternating current. Conversely, DC motor–pump units are preferred in decentralised and mobile systems particularly in photovoltaic (PV)-powered or battery operated configurations where direct current operation enables enhanced autonomy and flexibility. This distinction ensures optimised energy utilisation and adaptability across varying operational contexts. Both technologies play a vital role in the automation of modern hydraulic systems, offering a balance between power density, control precision, and energy efficiency [69].



(a) AC pump unit

(b) DC pump unit

Figure II.10: Pump unit electrical types.

II.6.1 DC Pump Unit

DC-powered hydraulic pump units offer superior portability and are optimally suited for autonomous, off-grid, or solar-based hydraulic applications. Operating directly from photovoltaic arrays or storage batteries, they enable energy self-sufficiency and sustained hydraulic performance under variable conditions. Designed for mobility, these units excel in remote installations, agricultural irrigation, and mobile platforms where flexible deployment and energy efficiency are critical. Compact yet efficient, they combine high energy density with operational versatility, providing a reliable interface between renewable DC sources and hydraulic

actuators. Their inherent capability to merge sustainable energy with hydraulic functionality makes them an essential component in modern decentralized automation systems.

For analytical modeling, the DC motor driving the pump is assumed to exhibit constant field excitation. Neglecting switching transients and armature reaction effects, the armature voltage equation can be expressed as follows [70]:

$$V_{ch} = R_a I_{ch} + L_a \frac{dI_{ch}}{dt} + K_e \omega \tag{II.16}$$

where R_a and L_a represent the armature resistance and inductance, respectively, I_{ch} is the armature current, K_e the back electromotive force (EMF) constant, and ω the angular velocity of the motor shaft.

The electromagnetic torque generated by the motor is given by:

$$C_e = K_t I_{ch} \tag{II.17}$$

The hydraulic pump imposes a resisting torque that increases nonlinearly with speed, modeled as:

$$C_r = K_r \omega^2 + C_s \tag{II.18}$$

where K_r ($Nm{\cdot}s^2/rad^2$) and C_s denote, respectively, the viscous and static torque coefficients. The electromechanical coupling between the motor and the pump can then be described by the dynamic equilibrium of torques:

$$J_a \frac{d\omega}{dt} = C_e - C_r \tag{II.19}$$

where J_a is the combined moment of inertia of the motor–pump assembly. This differential equation governs the transient and steady-state response of the DC-driven hydraulic pump, providing a foundation for performance simulation, control design, and efficiency optimization.

II.6.2 AC Pump Units

AC motor-driven hydraulic pumps are widely recognized for their superior suitability in fixed or industrial environments, where continuous operation, mechanical robustness, and grid synchronization are key performance requirements. These systems typically couple a three phase induction motor with a centrifugal pump, forming a configuration known for its reliability, mechanical simplicity, and high volumetric efficiency.

Due to their ability to deliver constant torque over a broad speed range, AC pump units are highly effective in process automation, manufacturing, and large scale irrigation systems. When integrated with variable frequency drives (VFDs), their performance can be finely regulated to match hydraulic demand, thus enhancing both energy efficiency and system responsiveness [71]. This combination of electrical and hydraulic optimization has established AC motor–pump units as the standard solution in industrial and agricultural sectors where high power density and long service life are essential.

II.6.2.1 Induction Motor

Induction motors (IMs) constitute one of the most essential components of modern electromechanical energy conversion systems, forming the backbone of industrial, agricultural, and domestic applications. Their widespread use stems from their robust construction, operational simplicity, high reliability, and minimal maintenance requirements, as illustrated in Figure (II.11). These machines are manufactured in various topologies, including single phase, three phase squirrel-cage, and wound-rotor configurations, with the three phase induction motor being the most prevalent in industrial practice due to its superior performance, efficiency, and versatility [72]. Moreover, advances in control strategies and power electronics have further enhanced their adaptability, enabling precise torque and speed regulation. Empirical studies demonstrate that AC-driven pump systems incorporating induction motors can achieve up to 30% energy savings compared with conventional electromechanical systems, underscoring their significance in sustainable engineering solutions [73].

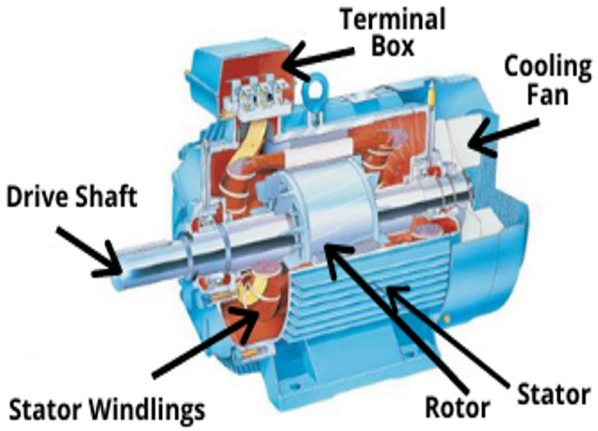

Figure II.11: Induction motor presentation.

General Characteristics

The asynchronous motor, more commonly referred to as the induction motor, operates on the principle of electromagnetic induction between the stator and rotor windings, producing torque without direct electrical connection between them [74][75]. Its essential components can be summarised as follows:

- An inductive polyphase stator winding, distributed on a laminated cylindrical core, supplied with balanced polyphase currents to generate a rotating magnetic field.
- A rotor winding, placed coaxially and electromagnetically coupled to the stator, in which currents are induced by the rotating field.
- The electromagnetic interaction between the stator field and the induced rotor currents produces a resultant torque that drives the rotor. In standard operation, the stator winding is stationary while the rotor is free to rotate; however, certain special configurations involve reversed roles or short-circuited rotor windings.
- Due to the induction mechanism, the rotor speed never reaches the synchronous speed of the rotating magnetic field. If synchronisation were achieved, no relative motion would exist between the stator field and the rotor conductors, thereby nullifying the induced currents and torque. Consequently, the rotor always operates at a speed slightly below synchronous speed, characterised by the slip g, defined as the relative difference between synchronous speed N_s and actual rotor speed N.

For analytical modelling, several simplifying assumptions are adopted to facilitate the mathematical representation of the induction motor [76]:

- The machine is magnetically symmetrical with a uniform air gap.
- Slotting and cogging effects are neglected.
- The air-gap flux distribution is perfectly sinusoidal.
- The magnetic circuit is assumed linear (unsaturated), implying a linear flux–current relationship.
- The effects of temperature rise and non-uniform current density are ignored.
- Iron losses due to hysteresis and eddy currents are neglected.

Description

Under the bipolar assumption, the induction motor may be represented by its cross-sectional view perpendicular to the rotational axis, as depicted in Figure (II.12). The model can be extended to a $2p$-pole configuration through appropriate modification of the torque equations. Both the stator and rotor are equipped with laminated magnetic cores and balanced three phase windings, separated by an air gap to allow electromagnetic coupling. The angular spatial distribution of the windings is defined by the following trigonometric relationships [77]:

$$\begin{cases} (oas, od) = \theta_s, \quad (obs, od) = \theta_s - \frac{2\pi}{3}, \quad (ocs, od) = \theta_s - \frac{4\pi}{3}, \\ (oar, od) = \theta_{s1}, \quad (obr, od) = \theta_{s1} - \frac{2\pi}{3}, \quad (ocr, od) = \theta_{s1} - \frac{4\pi}{3}, \\ (od, oq) = \frac{\pi}{2} \end{cases} \tag{II.20}$$

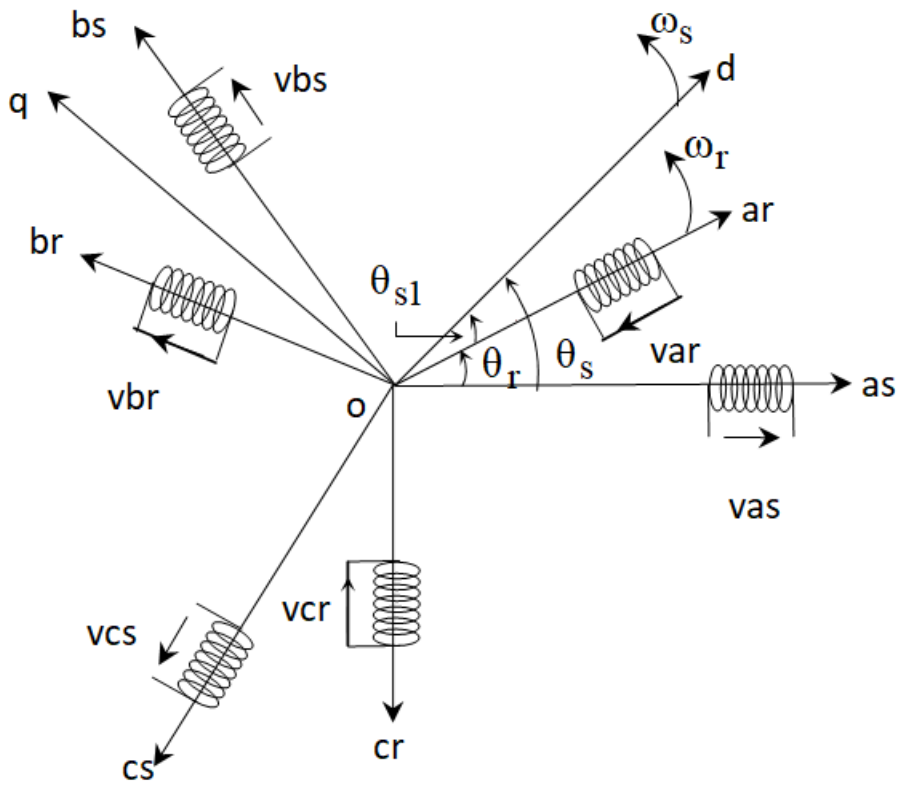

Figure II.12: Schematic representation of the induction motor.

The stator windings (a_s, b_s, c_s) and rotor windings (a_r, b_r, c_r) are distributed along respective magnetic axes. For analytical convenience, the machine variables are projected onto two orthogonal axes: the direct (d) and quadrature (q) axes. The instantaneous angular velocity of the rotor is thus expressed as:

$$\omega_r = \frac{d\theta_r}{dt} = \frac{d\theta_s}{dt} - \frac{d\theta_{s1}}{dt} \tag{II.21}$$

II.6.3 Three Phase Induction Motor Equations

The dynamic behaviour of the induction motor arises from the coupling of electrical, magnetic, and mechanical subsystems. This interdependence is expressed through the relationships among voltages, currents, flux linkages, torque, and angular velocity, providing the foundation for both steady-state and transient modelling [72].

Electrical Equations

For the six distributed windings $(a_s, b_s, c_s, a_r, b_r, c_r)$, the instantaneous voltage–flux linkage relationships can be formulated as [78]:

$$\begin{bmatrix} V_{as} \\ V_{bs} \\ V_{cs} \end{bmatrix} = \frac{d}{dt} \begin{bmatrix} \phi_{as} \\ \phi_{bs} \\ \phi_{cs} \end{bmatrix} + R_s \begin{bmatrix} i_{as} \\ i_{bs} \\ i_{cs} \end{bmatrix}, \quad \begin{bmatrix} V_{ar} \\ V_{br} \\ V_{cr} \end{bmatrix} = \frac{d}{dt} \begin{bmatrix} \phi_{ar} \\ \phi_{br} \\ \phi_{cr} \end{bmatrix} + R_r \begin{bmatrix} i_{ar} \\ i_{br} \\ i_{cr} \end{bmatrix} \tag{II.22}$$

Magnetic Equations

Assuming linear magnetic characteristics, the flux linkages can be expressed as functions of the stator and rotor currents [79]:

$$\begin{bmatrix} \phi_{as} \\ \phi_{bs} \\ \phi_{cs} \end{bmatrix} = \mathbf{L_s} \begin{bmatrix} i_{as} \\ i_{bs} \\ i_{cs} \end{bmatrix} + \mathbf{M_{sr}} \begin{bmatrix} i_{ar} \\ i_{br} \\ i_{cr} \end{bmatrix}, \quad \begin{bmatrix} \phi_{ar} \\ \phi_{br} \\ \phi_{cr} \end{bmatrix} = \mathbf{L_r} \begin{bmatrix} i_{ar} \\ i_{br} \\ i_{cr} \end{bmatrix} + \mathbf{M_{rs}} \begin{bmatrix} i_{as} \\ i_{bs} \\ i_{cs} \end{bmatrix} \tag{II.23}$$

where $\mathbf{L_s}$ and $\mathbf{L_r}$ denote the self-inductance matrices, and $\mathbf{M_{sr}} = \mathbf{M_{rs}}^T$ represents the mutual inductance coupling between the stator and rotor, dependent on the rotor position θ.

II.6.4 Equivalent Two-Phase (d–q) Model

To facilitate control-oriented modeling and dynamic analysis, the three phase quantities are transformed into an equivalent two-phase (d–q) system using the Park transformation. This approach decouples the flux- and torque producing components, simplifying vector control and performance optimization [80].

$$P = \sqrt{\frac{2}{3}} \begin{bmatrix} \cos\theta & \cos\left(\theta - \frac{2\pi}{3}\right) & \cos\left(\theta - \frac{4\pi}{3}\right) \\ -\sin\theta & -\sin\left(\theta - \frac{2\pi}{3}\right) & -\sin\left(\theta - \frac{4\pi}{3}\right) \\ \frac{1}{\sqrt{2}} & \frac{1}{\sqrt{2}} & \frac{1}{\sqrt{2}} \end{bmatrix} \tag{II.24}$$

$$\begin{bmatrix} x_d \\ x_q \\ x_0 \end{bmatrix} = P \begin{bmatrix} x_a \\ x_b \\ x_c \end{bmatrix}, \quad \begin{bmatrix} x_a \\ x_b \\ x_c \end{bmatrix} = P^{-1} \begin{bmatrix} x_d \\ x_q \\ x_0 \end{bmatrix} \tag{II.25}$$

Electrical and Magnetic Equations in (d–q) Frame

Applying the Park transformation yields the following voltage and flux linkage equations:

$$\begin{bmatrix} v_{ds} \\ v_{qs} \end{bmatrix} = R_s \begin{bmatrix} i_{ds} \\ i_{qs} \end{bmatrix} + \frac{d}{dt} \begin{bmatrix} \phi_{ds} \\ \phi_{qs} \end{bmatrix} + \begin{bmatrix} 0 & -\omega_s \\ \omega_s & 0 \end{bmatrix} \begin{bmatrix} \phi_{ds} \\ \phi_{qs} \end{bmatrix} \tag{II.26}$$

$$\begin{bmatrix} v_{dr} \\ v_{qr} \end{bmatrix} = R_r \begin{bmatrix} i_{dr} \\ i_{qr} \end{bmatrix} + \frac{d}{dt} \begin{bmatrix} \phi_{dr} \\ \phi_{qr} \end{bmatrix} + \begin{bmatrix} 0 & -\omega_{sl} \\ \omega_{sl} & 0 \end{bmatrix} \begin{bmatrix} \phi_{dr} \\ \phi_{qr} \end{bmatrix} \tag{II.27}$$

$$\begin{bmatrix} \phi_{ds} \\ \phi_{dr} \end{bmatrix} = \begin{bmatrix} L_s & M_{sr} \\ M_{sr} & L_r \end{bmatrix} \begin{bmatrix} i_{ds} \\ i_{dr} \end{bmatrix}, \qquad \begin{bmatrix} \phi_{qs} \\ \phi_{qr} \end{bmatrix} = \begin{bmatrix} L_s & M_{sr} \\ M_{sr} & L_r \end{bmatrix} \begin{bmatrix} i_{qs} \\ i_{qr} \end{bmatrix} \tag{II.28}$$

Mechanical and Torque Equations

The electromagnetic torque, resulting from the interaction between the air-gap flux and stator currents, is given by:

$$C_{em} = \phi_{ds} i_{qs} - \phi_{qs} i_{ds} \tag{II.29}$$

For a p-pair pole machine, the torque and mechanical motion equations can be expressed as:

$$\begin{cases} C_{em} = \dfrac{pM_{sr}}{L_r}(\phi_{dr} i_{qs} - \phi_{qr} i_{ds}) \\ J\dfrac{d\omega_r}{dt} = p(C_{em} - C_r) - f\omega_r \end{cases} \tag{II.30}$$

where J denotes the system inertia, C_r the resisting torque, and f the viscous friction coefficient.

Clarke Transformation

For stationary reference frame analysis, particularly in control implementations such as direct torque control (DTC), the Clarke transformation projects three phase quantities onto two orthogonal stationary axes (α, β) [81].

$$\begin{bmatrix} x_\alpha \\ x_\beta \end{bmatrix} = \sqrt{\frac{2}{3}} \begin{bmatrix} 1 & -\frac{1}{2} & -\frac{1}{2} \\ 0 & \frac{\sqrt{3}}{2} & -\frac{\sqrt{3}}{2} \end{bmatrix} \begin{bmatrix} x_a \\ x_b \\ x_c \end{bmatrix} \tag{II.31}$$

The inverse (transpose) transformation reconstructs the three phase system, yielding simplified torque and motion expressions in the (α, β) plane [82]:

$$C_{em} = \frac{pM_{sr}}{L_r}(\phi_{r\alpha} i_{s\beta} - \phi_{r\beta} i_{s\alpha}), \qquad \frac{d\Omega}{dt} = \frac{1}{J}(C_{em} - C_r - f\Omega) \tag{II.32}$$

II.7 Centrifugal Pump

Centrifugal pumps represent one of the most widely adopted hydraulic machines for liquid transfer in agricultural, industrial, and renewable-energy-driven applications. Their operation is based on the dynamic exchange between mechanical and hydraulic energy, where the impeller imparts kinetic energy to the fluid, subsequently converted into pressure head within the volute casing.

A centrifugal pump is typically designed for a relatively constant total manometric head (HMT), while its discharge flow rate varies proportionally with the rotational speed of the driving motor. The torque required by the pump rises nonlinearly with speed, reflecting the quadratic dependency between discharge head and rotational velocity. Consequently, to sustain adequate flow and pressure, the motor must operate at sufficiently high speed.

The input power consumption, proportional to the product $Q{\cdot}HMT$, scales approximately with the cube of the rotational speed, which is a critical factor in efficiency optimization and system sizing [83]. Centrifugal pumps are therefore preferentially employed for medium to large flow rates and moderate pumping heads (typically below 70 meters), where their performance characteristics are most favorable. The number of impellers or turbine stages is determined according to the required flow rate and total head.

The operation of a centrifugal pump is governed by three fundamental parameters: head (H), flow rate (Q), and angular velocity (ω) [84]. These interdependencies are expressed through the general functional relationship:

$$f(H, Q, \omega) = 0 \tag{II.33}$$

To simplify practical analysis, it is often assumed that the rotational speed ω remains constant. The total manometric head (HMT) is expressed as the sum of the static (geometric) head and the dynamic (frictional) losses:

$$HMT = H_g + P_c \tag{II.34}$$

Where: H_g: Geometric height (m), representing the vertical distance between the water surface in the suction tank and the discharge point.
P_c: Head losses (m) caused by fluid friction and local resistances within the pipeline system. These losses are expressed as:

$$P_c = \left(\lambda \frac{L}{d} + \epsilon\right)\left(\frac{8Q^2}{\pi^2 D^4 g}\right) = K_p Q^2 \tag{II.35}$$

Where:
λ: Coefficient of linear friction losses.
D: Internal pipe diameter (m).
L: Total length of the pipeline (m).
g: Gravitational acceleration ($9.81\, m/s^2$).
ϵ: Coefficient of local pressure losses due to fittings, bends, or valves.
K_p: Hydraulic resistance constant of the pipeline.
Q: Pump discharge flow rate (m^3/s).

In the context of photovoltaic-powered pumping systems, it is essential to model the centrifugal pump in a way that links the total head (HMT) directly to the flow rate (Q) and the motor speed (ω). The empirical representation commonly employed is [85]:

$$HMT = C_1\omega^2 - C_2 Q - C_3 Q^2 \tag{II.36}$$

Here, C_1, C_2, and C_3 are characteristic coefficients provided by the manufacturer, determined through standard pump testing. The first term accounts for the head induced by impeller speed, while the latter two capture hydraulic losses proportional to the flow rate and its square, respectively.

The mechanical resistance of the pump manifests as a hydrodynamic torque C_r opposing the driving motor, expressed as [86]:

$$C_r = K_r \Omega^2 \tag{II.37}$$

where:
Ω: Angular velocity of the induction motor (rad/s).
K_r: Proportionality coefficient that relates torque to the square of the rotational speed, defined as [87]:

$$K_r = \frac{P_n}{\Omega_n^3} \tag{II.38}$$

P_n: Nominal (rated) power of the induction motor (W).
Ω_n: Nominal angular speed of the induction motor (rad/s).

This relationship is crucial for the dynamic modeling and control of photovoltaic water pumping systems, as it enables accurate coupling between the electrical drive and the hydraulic load. The quadratic and cubic dependencies on rotational speed form the basis for efficiency optimization through speed control and maximum power point tracking (MPPT) in PV-driven irrigation systems.

II.8 Conclusion

In this chapter, a comprehensive modelling framework for the principal components of a photovoltaic-powered water pumping and irrigation system has been presented. Each subsystem was analysed to establish its electrical, mechanical, and hydraulic interdependencies under varying environmental conditions.

For the photovoltaic generator, a detailed mathematical model was developed to account for the nonlinear current–voltage characteristics and the influence of meteorological factors such as irradiance and temperature. This model enables accurate estimation of the available electrical power under standard and real operating conditions.

Subsequently, the static power converters—namely, the DC-DC boost converter and the DC-AC inverter—were described, assuming ideal switching devices and neglecting parasitic losses. Their operational principles were mathematically formulated to highlight their role in power conditioning, maximum power point tracking (MPPT), and conversion efficiency within the PV pumping system.

The electromechanical conversion stage, consisting of the induction motor and centrifugal pump, was modelled to capture the coupled dynamics between electrical input and hydraulic output. The centrifugal pump equations were presented as a function of discharge, total head, and rotational speed, forming a basis for analysing hydraulic performance and motor loading characteristics.

Overall, the theoretical and technological foundations established in this chapter provide the essential groundwork for the next stages of this research, which will focus on the control design, system optimization, and experimental validation of the photovoltaic pumping and automated irrigation system under dynamic field conditions.

Chapter III

DEVELOPED TECHNIQUES

III.1 Introduction

This chapter presents a set of control principles for two test benches aimed at enhancing energy exchange in photovoltaic systems. In the first test bench, titled **Innovative Intelligent Control for Optimised Power Management in Photovoltaic Systems**, we developed a technical solution using an Arduino Mega combined with fuzzy logic intelligent control and a boost converter for direct current pumps. This approach aims to reduce the total hardware cost and maximise efficiency.

The second part, titled **Advanced Smart Irrigation System for Large-scale AC Pumping Applications**, focuses on smart irrigation. We proposed a control method for the HM310 hydraulic test bench. These strategies are primarily focused on improving the performance of the systems to achieve significant energy and water savings.

III.2 Intelligent Control for Optimised power Management in photostatic system

A photovoltaic (PV) pumping system test bench is an essential tool for evaluating and optimising the performance of solar-powered water pumping systems. This setup is particularly valuable for ensuring efficient energy conversion and reliable operation in remote or isolated areas. The test bench is designed with several key objectives in mind:

Implementation Fuzzy Logic MPPT Algorithm for dynamic adjustment ensures that the system consistently operates at its maximum power output, adapting to fluctuations in solar irradiance and temperature.

MPPT Integration with Sensors and Components in controller that integrate various sensors signals seamless communication and coordination among these components, ensuring efficient operation and a responsive system that adapts to changing values.

Real-time Data Acquisition from sensors which monitor the system for immediate decisions and quick respond to variation of energy production.

Controlling Boost Converter based on the output of fuzzy logic algorithm optimising energy management and enhancing overall efficiency.

Monitoring System Performance for continuously evaluate performance and makes real-time adjustments to maximise energy production ensures that the system operates optimally, providing reliable water pumping solutions .

Integrating advanced control algorithms and real-time data acquisition as developed techniques enhances not only the efficiency of photovoltaic pumping systems but also contributes to sustainable energy solutions. It represents a significant step forward in the development of reliable, solar-powered water pumping technologies for isolated regions.

III.3 Structural Overview

The system electronic circuit to be studied is illustrated in the Figure (III.1). the PV panel serves as the primary energy source, converting sunlight into electrical power. This power is then fed into the boost converter system as input voltage (Vpv), which is smoothed out by a capacitor (C1) and combined with current (Ipv) stabilised by an inductor (L). The fuzzy logic controller (FLC) optimises the system performance by adjusting parameters based on input data, which is processed by the Arduino Mega microcontroller. The boost converter increases the voltage extracted of the Pv panel to a level suitable for the pump, and the output voltage (Vout) powers the pump unit, ensuring efficient water pumping. This setup leverages fuzzy logic control intelligent control for optimal performance, making it a highly efficient and cost-effective solution for renewable energy applications.

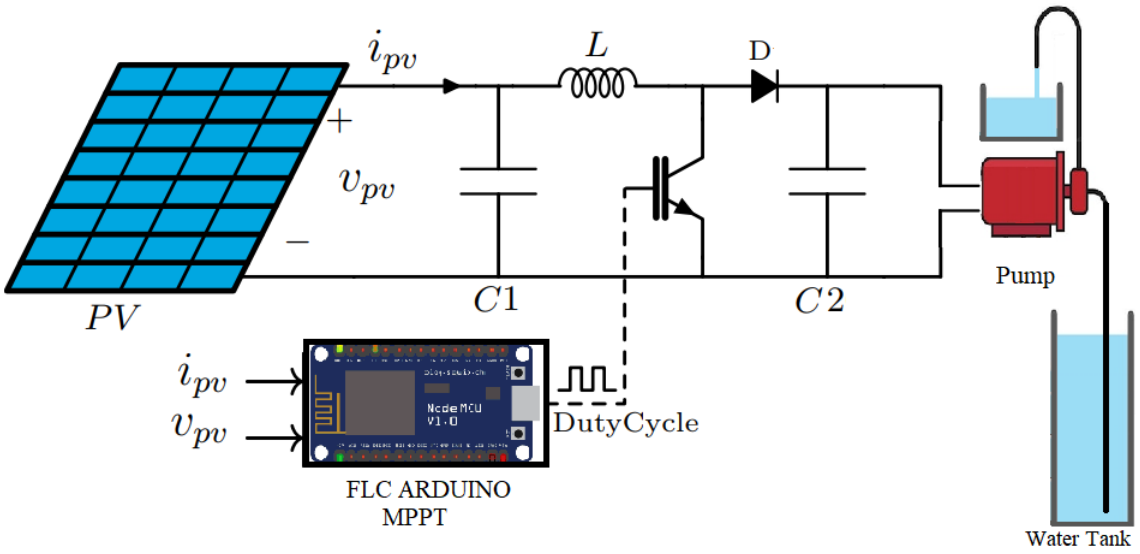

Figure III.1: Block diagram applied structure .

III.4 Energy Control Strategy

In order to validate the proposed energy control strategy, we need to first show the advantages of our approach compared to previous work. At this point, an optimal energy control strategy based on fuzzy logic has been devised. The advantages of this pumping system include improved energy efficiency, reduced operational costs, and enhanced reliability. The use of fuzzy logic allows for adaptive control that can handle varying environmental conditions, ensuring consistent performance. Additionally, the integration of modern microcontroller technology, such as the Arduino Mega, facilitates precise control and easy implementation. Overall, this system represents a significant advancement in renewable energy applications, providing a sustainable and cost-effective solution for pumping.

The system starts by measuring the current (Ipv) and voltage (Vpv) generated by the PV panel using sensors connected to the Arduino Mega microcontroller. These measurements provide real-time data about the operating conditions of the PV panel, this data is processed by the fuzzy logic controller as illustrated in Figure (III.2) is computational approach that deals with reasoning that is approximate rather than fixed and exact. These controller can handle complex, non-linear systems and are particularly useful in applications where traditional binary logic may be insufficient to represent human knowledge and decision-making processes .

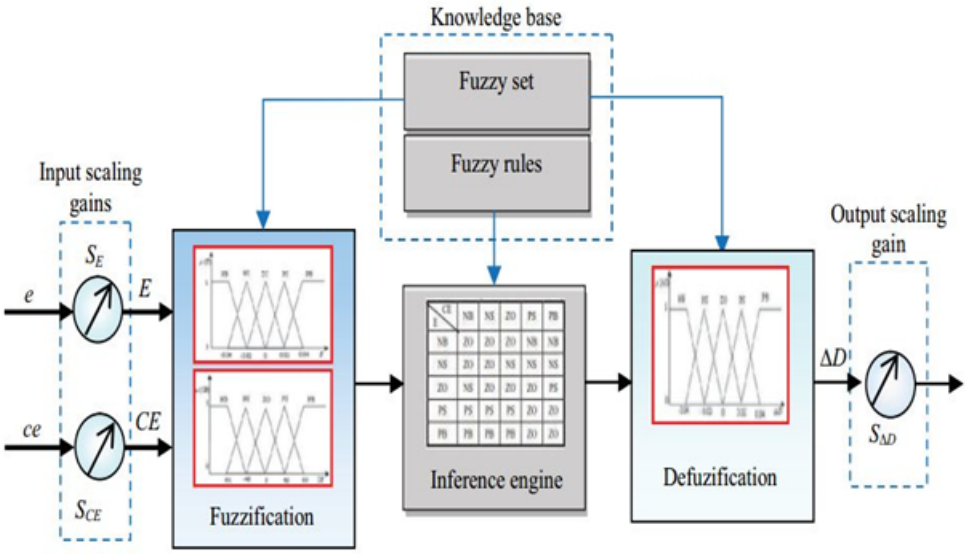

Figure III.2: Schematic electronic circuit of the proposed structure.

Fuzzy logic system is based on fuzzy logic intelligence to make decisions based on imprecise conditions or variable input information. Here is an explanation of how a fuzzy logic controller works:

III.4.1 Fuzzification

Numerical input values, in our case is voltage (Vpv) and current (Ipv) from the PV panel, are converted into linguistic variables or fuzzy sets. These fuzzy sets represent different degrees of trapezoidal membership functions in a particular category. In simple example, a temperature input can be categorised as cold, warm, or hot with varying degrees of membership in each category.

III.4.2 Rules

The controller operates based on a set of rules that define how input variables relate to output variables. These rules are typically in the form of if-then statements that capture the expert knowledge or heuristics of the system. For example, if voltage is high and current is low, then decrease the duty cycle.

III.4.3 Intelligence Inference

The Intelligence engine evaluates the rules based on the fuzzy sets of input variables to determine the appropriate voltage output fuzzy sets. It combines the rules to generate a fuzzy logic duty cycle output set that represents the control action to be taken

III.4.4 Defuzzification

The fuzzy output sets are converted back into numerical values or a single output value. This final output value represents the control action to be implemented in the system. Various methods such as centroid, mean of maximum , or weighted average are used for defuzzification. in our set up this value determines the duty cycle for the DC-DC boost converter injected as Pulse width modulation (PWM) that involves switching the power supply on and off at a high frequency for IGBT switch, ensuring that the PV panel operates at its maximum power point (MPP) for optimal energy harvesting.

III.4.5 Hardware Control components

The hardware components of this strategy include the boost converter, Arduino Mega control, and DC pump unit. The boost converter is the electronic circuit integrated into the system to control the output voltage value of the solar panel. It stabilises the power output by adjusting the voltage based on the input from the Arduino Mega microcontroller, ensuring efficient and reliable energy conversation. the Arduino Mega serves as the central control unit of the system. It executes the fuzzy logic control algorithm, drives the boost converter, and interfaces with sensors to monitor and adjust system parameters in real-time. This microcontroller processes the input data from the PV panel and other sensors to make intelligent decisions for maximum system power optimisation. The Arduino Mega generates PWM signal to control the operation of the boost converter. These PWM signal is must be amplified to the required voltage level for the IGBT gate of the boost converter, enabling efficient and precise control of the power conversion process. The PWM signal adjust as duty cycle, which in turn control voltage output of the boost converter. The system performance evaluation of the pump unit by the pump discharge function, ensuring voltage stability and optimal current supply helps maintain the nominal power delivery of the pumping unit, improving overall system efficiency and reliability. By ensuring that the pump operates within its optimal parameters, the system can provide consistent and efficient pumping. These hardware components work together to create a robust and efficient PV pumping system, leveraging

fuzzy logic control optimise energy production and ensure reliable operation under varying electronic and environmental conditions maintaining the maximum pumping available.

III.5 Smart Irrigation AC coupled PV pumping System for Large-scale Applications

This system designed to revolutionise water management in extensive agricultural fields and industrial settings. This system integrates cutting-edge technology, including a test bench set up, to optimise the efficiency and effectiveness of water distribution. By leveraging advanced sensors, automated controls, and high-capacity AC pumps, this smart irrigation system ensures precise water delivery, reduces energy consumption, and enhances overall productivity. The application in a test bench serves as a critical component, allowing for rigorous testing and fine tuning of the system to meet the diverse needs of large-scale irrigation applications.

III.5.1 PV AC pumping Test bench

We propose a smart irrigation control system using a centrifuge hydrophilic test bench to assess soil moisture, integrating a variable speed drive controlled by an Arduino. This setup includes real-time data collection via sensors and an algorithm that adjusts irrigation based on soil moisture and environmental conditions, ensuring optimal soil moisture for grassland growth year-round.

III.5.2 Implementation Structure Overview

The proposed system aims to optimise irrigation for grasslands by determining the precise amount of water needed through a smart integration of technology. First, a test bench is set up to monitor the grassland's state by sensing temperature and soil moisture levels, with sensors collecting real-time data. This data is processed by a programmed Arduino, which tailors the irrigation methods to the specific type of plants, converting it to control the variable speed drive (VSD) as a frequency, ensuring energy conversion from electrical to hydraulic is maximised. The system's algorithm dynamically adjusts irrigation based on seasonal changes and weather conditions, maintaining optimal soil moisture for grassland growth throughout the year. This innovative approach not only enhances resource efficiency

by saving water and electrical power but also ensures that the plants remain in perfect soil irrigation conditions for maximum healthy growth.

III.5.3 PV energy production

As illustrated in Figure (III.3), LARHYSS Renewable Energy Laboratory at Mohamed Khider Biskra university features a solar field comprising 40 photovoltaic 175 (W) (PV) modules, each with detailed electrical specifications provided in Table III.1 . Among these, a 15-module solar generator configuration was specifically designed to power the Laboratory and PV applications. This configuration consists of 5 modules connected in series and 3 such strings connected in parallel, delivering a combined output power of 2625 W under Standard Test Conditions (STC). The integration of solar energy with the HM310 pumping unit exemplifies a sustainable approach to water pumping for irrigation, leveraging renewable energy to reduce operational costs and environmental impact.

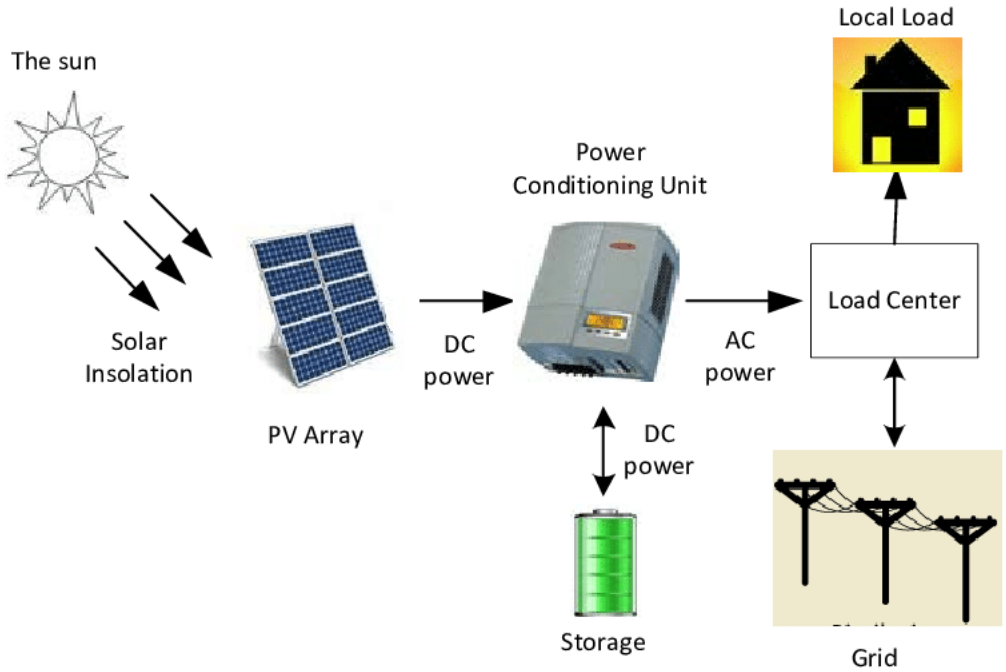

Figure III.3: LARHYSS Laboratory Solar PV field.

Model	Sharp NTR5E3E/NT175E1
Maximum power(P_{max})	175.0 W
Optimum current (I_{op})	4.95 A
Optimum voltage (V_{op})	35.4 V
Open circuit voltage (V_{oc})	44 V
Open circuit current(I_{cc})	5 A
Number of cell per module (N_s)	72

Table III.1: PV module characteristic.

III.5.4 Solar Energy Conversion

The conversion of solar photovoltaic (PV) energy into stable 220 V AC power relies on an efficient inverter system, The Xantrex SW3048E is high-performance inverter-charger plays a crucial role in transforming the DC power generated by the PV array into high-quality AC electricity for off-grid or hybrid systems.

The Xantrex SW3048E features a pure sine wave output, ensuring compatibility with sensitive electronics and appliances. With a 3 kW power rating, it efficiently handles varying loads while maintaining stable voltage output. Unlike grid-tied inverters, the SW3048E is designed for standalone or battery-backed systems, making it ideal for remote locations or backup power applications.

To maximise energy harvest, the inverter integrates with external charge controllers (or MPPT solar charge controllers in hybrid setups) that optimise PV power extraction under changing irradiance and temperature conditions. Additionally, its built-in battery charger allows seamless switching between solar, generator, or grid power sources when available.

Before inversion, a DC-DC converter or charge controller may condition the PV output to match the battery bank voltage (48 V DC in this case). The Xantrex SW3048E then converts this DC power into 220 V, 50 Hz AC (or other regional standards) with high efficiency. Its advanced safety features—including overload protection, temperature monitoring, and automatic shutdown—ensure reliable operation in demanding environments.

By leveraging the Xantrex SW3048E's robust design and flexible power management, solar energy systems achieve efficient, stable, and resilient off-grid power conversion.



Figure III.4: 3 kW Xantrex SW3048E DC-AC inverter-charger

III.5.5 Energy Management

To ensure optimal performance of a photovoltaic (PV) system , Maximum Power Point Tracking (MPPT) technology is essential. MPPT controllers dynamically adjust the operating point of the PV array to extract the maximum available power under varying environmental conditions, such as changes in sunlight intensity or temperature. This ensures that the system operates at its highest efficiency, even during partially cloudy days or seasonal variations. By integrating MPPT into the system, energy losses are minimised, and the overall output of the PV array is significantly improved.

A Smart Energy Management System (EMS) can optimise the operation of a PV system by intelligently managing energy flow between the PV array, storage system, and grid. The EMS monitors energy production, consumption, and storage levels in real time, making decisions to prioritise self-consumption, charge batteries, or export energy to the grid. This ensures efficient use of generated energy, reduces waste, and enhances the system's overall performance. Advanced EMS can also incorporate weather forecasts to predict energy generation and adjust operations accordingly.

In PV pumping systems, such as those used for irrigation, energy management can be optimised by incorporating grid export capability. When the pump is not in use (e.g., during rainy seasons or at night), excess PV energy can be redirected to the grid instead of being

wasted. This requires a bidirectional inverter and a control system that switches between pumping mode and grid export mode. Such a setup not only maximises the utilisation of PV energy but also provides an additional revenue stream through energy sales to the grid.

III.5.6 Irrigation control Via VSD

Using a Variable Speed Drive (VSD) for irrigation control optimises water distribution by adjusting pump motor speed based on demand figure(III.5), ensuring efficient pressure and flow. This approach reduces energy consumption by up to 50%, minimises water waste, and extends equipment lifespan through soft starts and stops. Integrated with sensors and automation, VSDs enable precise, scalable irrigation for agriculture, landscaping, and greenhouses. The result is a cost-effective, eco-friendly system that enhances performance while conserving resources.

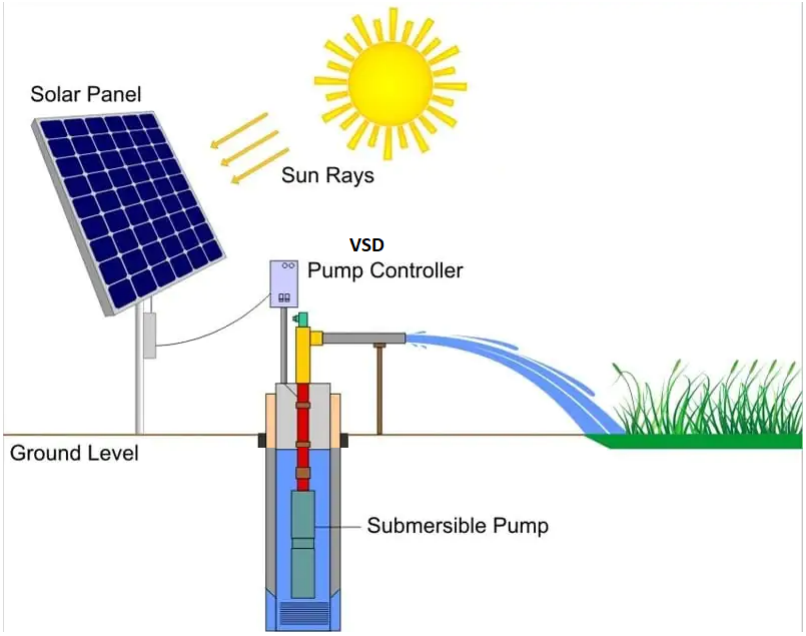

Figure III.5: VSD irrigation block diagram

III.5.7 System operation

The developed system is based on the HM 310 test bench, which functions as an integrated and modular platform for investigating the discharge and performance characteristics of PV centrifugal pumps under controlled experimental conditions Figure(III.6). Its configuration enables precise manipulation and monitoring of hydraulic, electrical, and mechanical vari-

ables, making it an ideal foundation for the implementation and validation of smart irrigation system control strategies and energy optimisation techniques.

The test bench incorporates a centrifugal pump driven by a regulated-speed electric motor, supported by a comprehensive measurement and control assembly. The hydraulic circuit consists of a water reservoir, suction and discharge lines, shut-off valves, and strategically positioned sensors that enable multi-variable characterisation. Flow rate measurement can be achieved using a magneto-inductive flow meter, a floating-body flow meter, or a differential pressure sensor, depending on the desired measurement resolution and test configuration. The suction and discharge pressures are measured using high-precision absolute pressure transducers, ensuring accurate assessment of pump head and overall hydraulic efficiency.

The pump's rotational motion is provided by a three phase asynchronous motor whose speed is controlled through a variable frequency drive (VFD), allowing adjustment from 0 to 2850 rpm. This control flexibility enables a broad spectrum of operating conditions to be simulated, permitting the derivation of characteristic curves such as Q–H, Q–η, and Q–P relationships. Temperature and torque sensors complement the instrumentation, allowing for detailed analysis of thermal and mechanical responses essential for complete energy balance and efficiency evaluation.

All measured parameters flow rate, pressure, temperature, rotational speed, and torque are digitally displayed and continuously logged for advanced post-processing and analysis. The acquired data can be analysed in computational environments such as MATLAB or LabVIEW to generate performance curves, transient behavior assessments, and control response validations. Because of its compact structure and integrated water circuit, the HM 310 system remains fully autonomous and transportable, making it suitable for both laboratory research and applied training scenarios without reliance on an external water network.

In summary, the developed system represents a robust and flexible platform for implementing, testing, and optimising smart irrigation control concepts. It bridges the gap between theoretical modelling and practical realisation, providing a replicable and scalable experimental environment for energy-efficient irrigation and hydraulic performance evaluation.

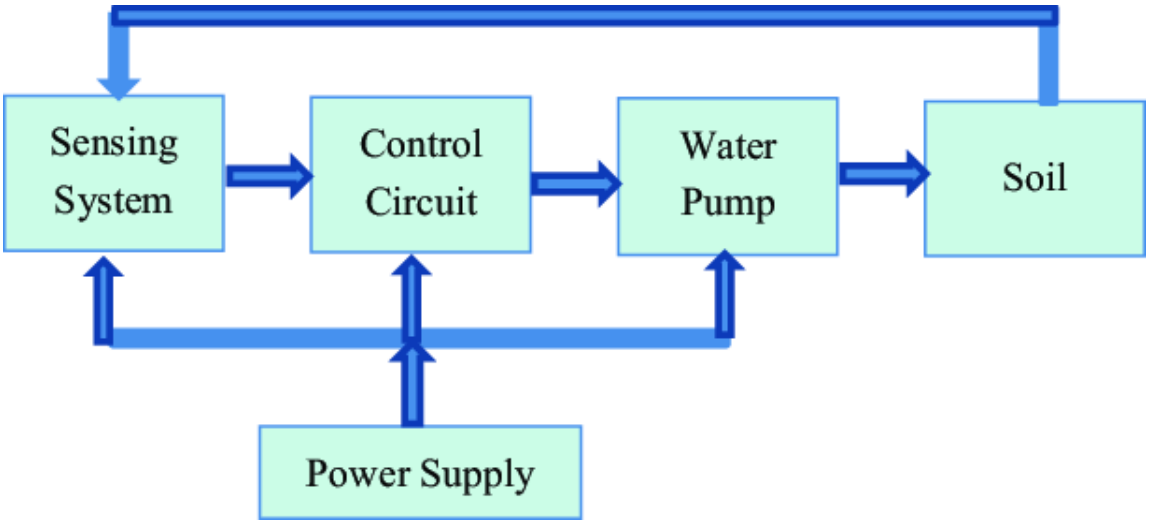

Figure III.6: Block diagram of implemented smart irrigation system architecture.

III.5.8 Role of water in vegetation

Water has a significant role in the growth of plants. It functions as a solvent for the minerals in soil and the compounds made by the cells, allowing them to be transported to the site of use. On the one hand, it enters the very structure of living matter and, as such, can be thought of as food for the plant. Lastly, it should be noted that the temperature of plant organs is continuously decreased by evaporation on both their surface and that of the soil, which may have positive effects in hot regions [88].

III.5.8.1 Water as food

Studies conducted by several authors to ascertain the amount of water present in plants, including both the water entering the cell structure and the water flowing through the different vessels, reveal that the proportion by weight might reach up to 95% . Trees: 50-60 % of all trees [89].

75% vegetable grain. 90% of fruits and salads. 95% The growth season affects the tissues water content [90]. It appears to peak during the blossoming phase and to significantly decline throughout the ripening phase.

III.5.8.2 Water considered as a solvent

Water serves as a universal solvent in biological systems due to its polar nature and ability to dissolve ionic and polar compounds . In soil ecosystems, water dissolves mineral constituents

through hydration and ionization processes, facilitating nutrient availability for plant uptake . The movement of water into plant roots is governed by water potential gradients, which are determined by the difference between osmotic pressure generated by solute concentrations in root cells and the counteracting turgor pressure exerted by rigid cell walls under turgid conditions. The equilibrium between these forces ensures regulated water absorption while preventing cell rupture, a mechanism critical to plant hydraulic regulation[91][92] .

III.5.8.3 Cooling of plants

Plants maintain an optimal temperature for healthy growth through a process known as thermoregulation. This is achieved by absorbing heat, which is then dissipated through the evaporation of water on the surface of their leaves. Water plays a critical role in this evaporative cooling mechanism. As water molecules evaporate, they absorb heat energy from the plant, effectively lowering the plant's temperature. This process not only helps in regulating the plant's internal temperature but also ensures that the plant remains within a conducive thermal range for its physiological processes. The ability to control temperature through water evaporation is crucial for the plant's overall health, growth, and productivity, as it prevents overheating and maintains the necessary conditions for photosynthesis and other metabolic activities[93][94].

III.6 Water requirements of cultivated plants

Plant water requirements are dynamically regulated by transpirational and evaporative losses, which exhibit diurnal and seasonal variability due to fluctuating environmental conditions such as light intensity, humidity, and temperature . These losses can account for 97–99.5% of absorbed water, necessitating adaptive root hydraulic conductivity to maintain water uptake efficiency. Root systems achieve this flexibility through aquaporin-mediated regulation of water transport and plasticity in root architecture, allowing plants to respond to transient soil moisture gradients [95].

Water demands vary significantly across plant functional types, as illustrated in Table III.2. For example, xerophytic species (e.g., cacti) exhibit minimal requirements (0–1 L/m^2) due to Crassulacean Acid Metabolism (CAM) and reduced stomatal density, whereas mesophytic crops (e.g., vegetables) demand higher inputs (6–8 L/m^2) to sustain high transpiration rates [96]. These differences reflect evolutionary adaptations to native habitats and physiological trade offs between water conservation and photosynthetic productivity [97].

Plant Type	Water Requirement (L/m^2)
Cacti	0-1
Succulents	1-2
Grass	2-4
Shrubs	4-6
Vegetables	6-8
Flowers	6-8
Trees	8-10
Fruits	8-10

Table III.2: Water demand variations across plants

III.6.1 Irrigation Grassland

Irrigation is a critical practice in grassland ecosystems to sustain biomass production and promote ecological resilience, particularly in semi-arid regions or during drought periods where precipitation falls below evapotranspiration demands. By compensating for water deficits, irrigation ensures consistent soil moisture for grass and associated flora, maintaining photosynthetic activity and root development [98].

Grassland irrigation systems range from surface sprinklers to precision methods like center-pivot or drip irrigation, with system selection dependent on spatial scale, water-use efficiency (WUE), and species-specific hydraulic needs [99]. For instance, pivot systems are favoured in large-scale temperate grasslands due to uniform water distribution, while drip irrigation minimises evaporation losses in water-scarce regions [100].

Effective irrigation management balances water delivery with soil infiltration rates to avoid waterlogging (which disrupts root aeration and promotes anaerobic conditions) and nutrient leaching (e.g., nitrate displacement beyond root zones) [101]. Under-irrigation, conversely, induces water stress, reducing stomatal conductance and curtailing carbon assimilation . Optimal irrigation scheduling, informed by soil moisture sensors or evapotranspiration models, enhances WUE by aligning applications with plant phenological stages [93].

III.7 Conclusion

In the first part of chapter the DC test bench we explain our advance approach for the photovoltaic (PV) pumping system leverages advanced hardware components and intelligent fuzzy logic control to optimise energy production and ensure efficient pumping. The system integrates a boost converter to stabilise and adjust the output voltage for MPP of the PV panel, maximising energy extraction. The Arduino Mega serves as the central control unit, executing the fuzzy logic control algorithm, generating PWM signal, and interfacing with sensors to monitor and adjust system parameters in real-time. This precise control ensures that the system operates at its maximum power, enhancing overall efficiency. Additionally, the system continuously evaluates and increase performance of the pumping unit in different weather scenarios.

In the second part of the chapter presented design of a Smart Irrigation AC-coupled PV Pumping System-scale applications, integrating a PV generator, Xantrex SW3048E inverter, VSD, and HM310 test bench. Three key contributions technic were made:

1. A battery-less system with MPPT and EMS achieving efficient solar-to-hydraulic conversion with grid export capability;

2. Precise irrigation control via VSD and Arduino-based soil sensor, reducing energy consumption

3. The HM310 test bench as an experimental platform for pump characterisation and algorithm validation. The chapter also established the scientific basis for water management through plant physiology analysis and quantification of crop water requirements.

In summary This chapter thus establishes a clear, practical pathway toward intelligent irrigation, balancing agricultural demands with resource efficiency. The subsequent sections will detail the implementation and validation of the proposed control framework.

Chapter IV

IMPLEMENTATION AND TESTS RESULTS

IV.1 Introduction

The primary objective of this fourth chapter is to experimentally validate the control strategies developed throughout this thesis. These strategies are directly related to energy management within the converters and hydraulic performance of the photovoltaic powered pumping systems. The experimental validation process integrates two distinct test benches designed for DC and AC pumping systems.

The first test bench corresponds to a DC pumping system in real-time implementation of a fuzzy logic algorithm for maximum power point tracking (MPPT) equipped with a brushless DC motor coupled to a plastic centrifugal pump. This setup is mainly used to analyse the dynamic behavior of small-scale irrigation or laboratory scale pumping applications. The second test bench involves an AC induction motor centrifugal pump driven variable seeped drive (VSD) controlled with Arduino Uno microcontroller , representing large scale irrigation systems and enabling the evaluation of precise control strategies for maximum irrigation efficiency.

Three different power converters are employed in these experiments to validate the proposed control laws. Each converter is implemented on an Arduino based real-time control platform, ensuring flexibility, cost efficiency, and reliable performance. The developed algorithms are rigorously tested in terms of tracking accuracy, energy efficiency, and overall

system responsiveness under varying operating conditions.

IV.2 First Experimental DC Prototype

This First Experimental DC Prototype Figure (IV.1) presents the hardware design and real-time implementation of a fuzzy logic algorithm for maximum power point tracking (MPPT) in photovoltaic systems. The control approach is executed on Arduino MEGA microcontroller board to ensure low cost with efficient and adaptive energy extraction from the photovoltaic module under varying environmental conditions.

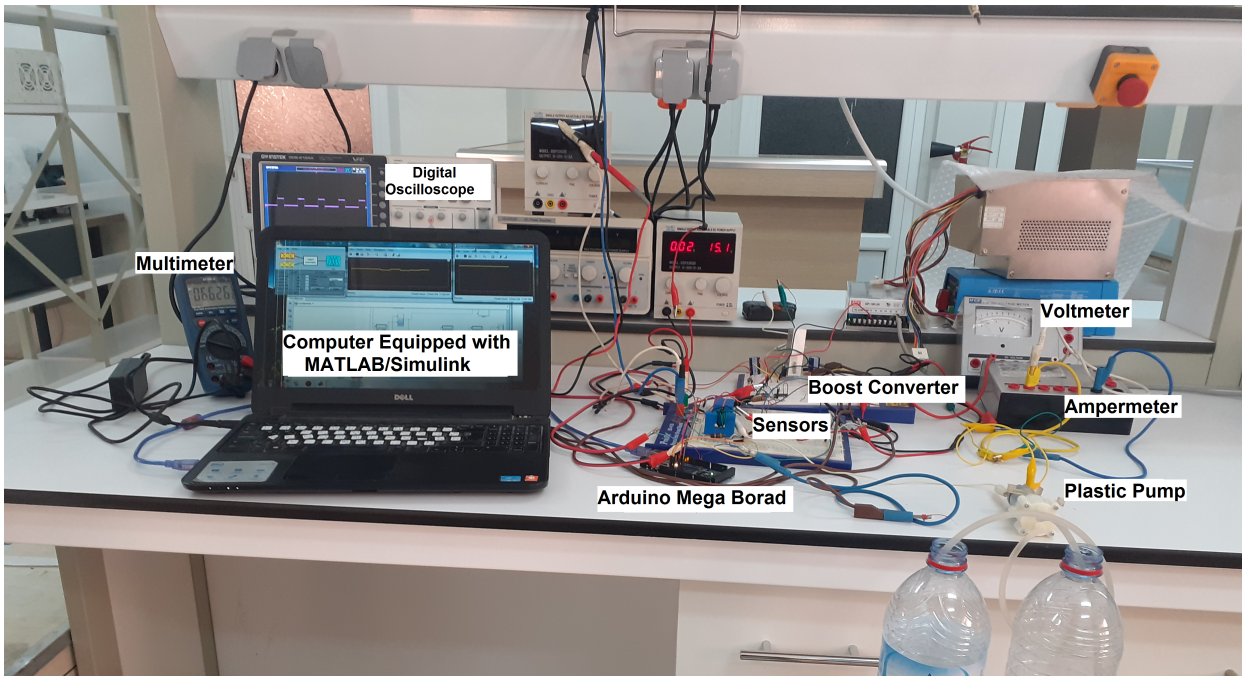

Figure IV.1: First experimental test bench

IV.2.1 Photovoltaic Module

A ROHS 20W Poly-crystalline photovoltaic Solar Module (XD20-12P) Figure IV.2 is a compact and efficient module used in experimental tests to evaluate solar energy system.making it ideal for small scale prototype application for research. The low power output allows for precise measurements and easy integration with other components [102], providing valuable insights into optimising photovoltaic technology The electrical parameters of the 20 W photovoltaic (PV) module used in the system are summarised in Table IV.1.



Figure IV.2: Photovoltaic module used in the experimental setup.

Table IV.1: Electrical parameters of the 20 W photovoltaic module.

Parameter	**Symbol / Unit**	**Value**
Maximum Power	$P_{\max}$ (W)	20
Maximum Power Voltage	V_{mp} (V)	17.5
Maximum Power Current	I_{mp} (A)	1.14
Open Circuit Voltage	V_{oc} (V)	21.24
Short Circuit Current	I_{sc} (A)	1.28
Power Tolerance	$\pm$ (%)	0.6

IV.2.2 Boost converter setup

The open circuit voltage of the photovoltaic panel varies with irradiance and temperature, producing a time varying terminal voltage that can fall outside the operating range required by the load. Consequently, the acoustic transducer cannot be driven at the desired voltage and power level when the panel voltage is below the load requirement . To ensure a stable and controllable supply to the load, a DC–DC boost converter is employed to step up and regulate the PV terminal voltage to the required bus level[103].

The boost converter topology Figure IV.3 used in the test bench comprises an energy storage inductor, a semiconductor switch (IGBT), a freewheeling diode and an output capacitor. The switch is pulse width modulated by the controller to transfer energy from the

PV source to the load while maintaining the desired output voltage; control loops implement voltage regulation and, when required, current limiting and protection functions. Component selection (inductance, capacitance, semiconductor ratings, and diode reverse recovery characteristics) is made to satisfy steady state and dynamic requirements: acceptable inductor ripple current, capacitor voltage ripple, switching losses, thermal limits and electromagnetic compatibility. The specific electrical and mechanical specifications of the components used in this converter are provided in Table IV.2.

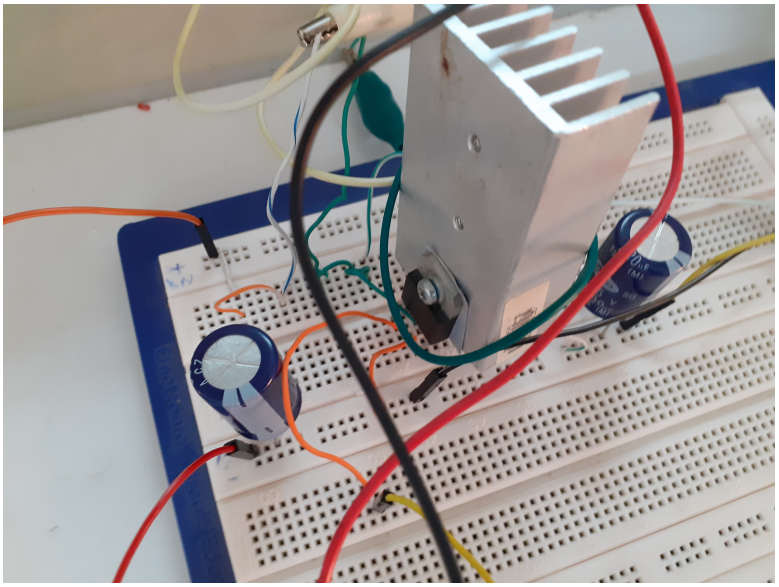

Figure IV.3: Boost converter

Table IV.2: Boost converter setup

Boost converter setup	
C1	220 µf
C2	220 µf
L	0.1 H
f	1 KHz
Controller type :Arduino Mega	
IGBT type :BUP314	
Diode type:BYV32-200	

IV.2.3 Arduino Mega Microcontroller

The data acquisition and control functions of the test bench are implemented on an Arduino Mega 2560 microcontroller Figure IV.4 . Photovoltaic generated current I_{pv} and terminal voltage V_{pv} are measured using dedicated current and voltage transducers whose outputs are conditioned (offset removal, scaling and anti aliasing filtering) and routed to the Arduino's analog to digital converter (ADC) inputs. The ADC on ATmega2560 provides 10 bit resolution; conversion timing, input multiplexing and reference selection are configured in firmware to ensure synchronous sampling and to minimise measurement noise and quantisation error[104].

The Arduino based processing unit executes the real-time control algorithm for the pumping station test bench: it acquires sensor data, computes control commands, drives actuator interfaces (PWM drivers, relays or gate drivers as required), and implements safety interlocks. Data logging, parameter tuning and advanced analysis are performed on a host computer. Communication between the Arduino and the host is established via the board's USB to serial interface (accessible as an RS-232/USB serial link), enabling bidirectional transfer of measurements, set points and diagnostic information. MATLAB is used on the host side for supervisory control, visualisation and post processing; exchange with the Arduino uses a serial protocol implemented in both the firmware and MATLAB scripts.

Table IV.3 lists the principal hardware and electrical characteristics of the Arduino Mega 2560 relevant to the test bench (ADC resolution and sampling, number of analog/digital channels, UARTs, PWM channels, operating voltage, and memory resources)[105].

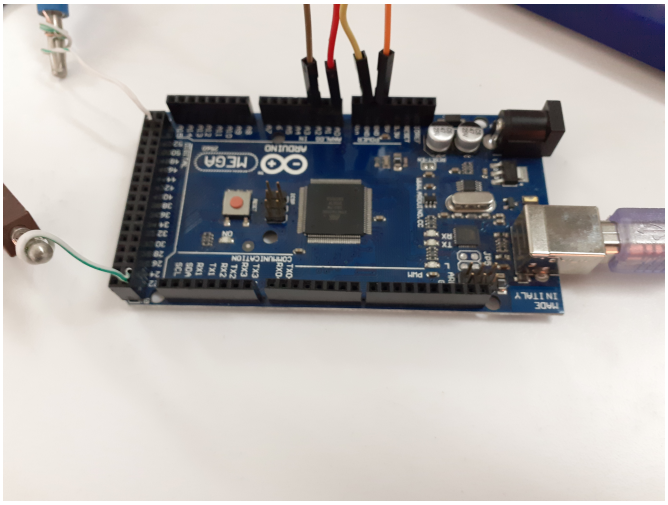

Figure IV.4: Arduino Mega

Table IV.3: Main characteristics of the Arduino Mega 2560

Parameter	Symbol / Unit	Value
Microcontroller		ATmega2560
Architecture		AVR 8 bit
Clock Frequency	f_{clk} (MHz)	16
Operating Voltage	V_{cc} (V)	5
Recommended Input Voltage	V_{in} (V)	7 -12
Absolute Input Voltage (not recommended)	$V_{\text{in,max}}$ (V)	20
Digital I/O Pins		54 (of which 15 PWM)
Analog Input Channels		16 (ADC 10 bit)
Flash Memory	/ (KB)	256 (8 KB used by bootloader)
SRAM	/ (KB)	8
EEPROM	/ (KB)	4
Max DC Current per I/O Pin	I_{IO} (mA)	20 recommended; 40 absolute
3.3V Pin Current	$I_{3.3V}$ (mA)	50 (depends on regulator)
ADC Resolution	bits	10
Timers		6 hardware timers (Timer0..Timer5)
USART / Serial Ports		4 (hardware UARTs)
Interfaces		SPI; I2C (TWI); UART; (CAN via shield)
USB Serial Chip		ATmega16U2 (USB B connector)
Programming		USB (bootloader) / ISP (ICSP)
Dimensions	/ (mm)	101.52 × 53.3
Weight	/ (g)	37
Operating Temperature	T (°C)	-40 to +85 (MCU limits)
Indicator LEDs		PWR, TX/RX, L (pin 13)
Typical Power Consumption	/ (mA)	Depends on sketch and peripherals
On board Features		Reset button; female headers; power jack; ICSP header
Compatibility		Arduino shields (form factor differences may apply)

IV.2.4 Current sensor LA55

The LA55-P current transducer is an electronic component Figure IV.5 designed to measure multiple current types, such as DC, AC, pulsed, etc. It supports galvanic isolation between the primary and secondary circuits up to 50A. The current in the primary circuit and the secondary circuit is related to each other as follows[106]:

$$I_s = N * I_p/1000V_m = I_s * R_m \tag{IV.1}$$

I_s: secondary circuit current, N: spears number, I_p: Primary nominal current, R_m: measuring resistance, V_m: measuring Voltage.

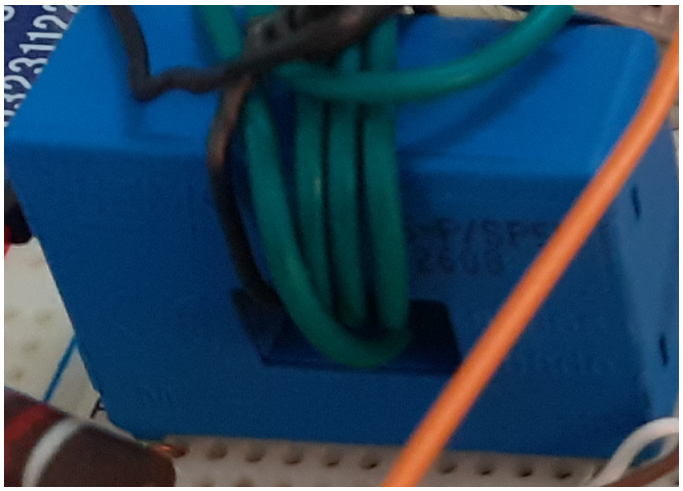

Figure IV.5: Current sensor LA55

IV.2.5 Voltage sensor LV25

With galvanic isolation between the primary and secondary circuits, the electronic voltage transducer LV25-P Figure IV 6 measures voltage of different currents (DC, AC, pulsed, etc.). The relationship between the voltage of the primary circuit, which has a maximum value of 500V, and the voltage of the secondary circuit is as follows [107]:

$$V_p = I_p * R_1 V_m = I_s * R_m \tag{IV.2}$$

V_p: primary circuit voltage, R_1 :primary circuit resistance, V_m: measuring Voltage, I_s: secondary circuit current, R_m : measuring resistance.

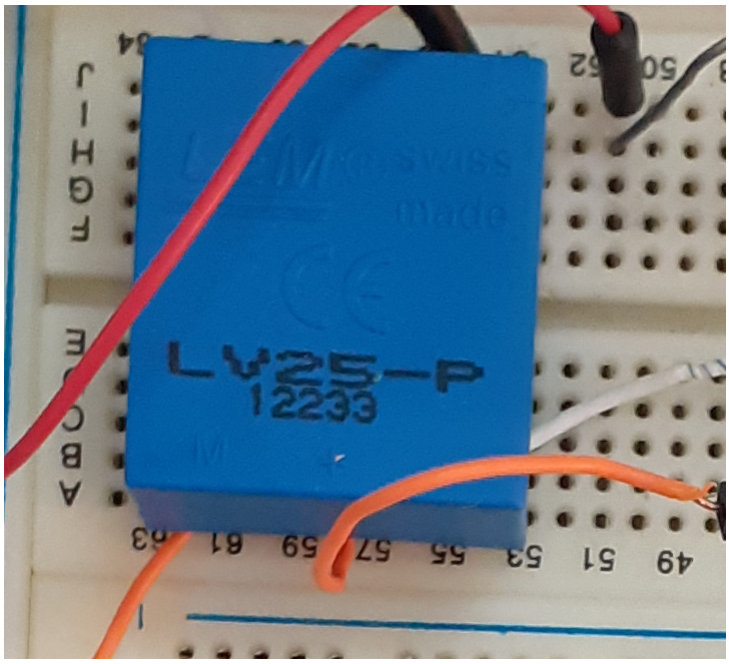

Figure IV.6: Voltage sensor LV25

IV.2.6 Arduino Mega PWM signal

Using the Arduino Mega PWM signal output to evaluate the intended MATLAB/Simulink simulation, we were able to obtain acceptable accuracy feedback results. Figure IV.7 illustrates these findings, which match the duty cycle rate variation values and form with the simulated control system. Rectangular waveform obtained experimentally shown. The acquired real-world answers were highly accurate and fully confirmed.

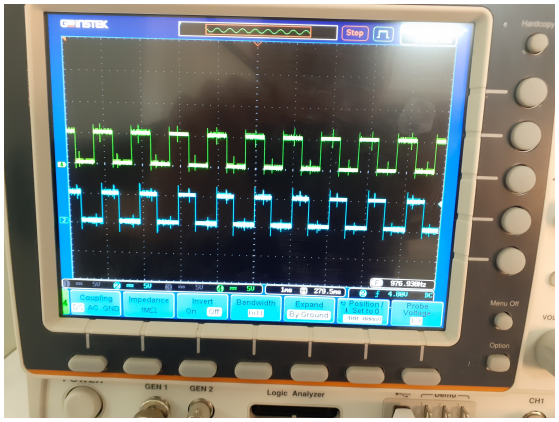

Figure IV.7: PWM signal of Arduino mega with DDS Function Generator signal

IV.2.7 PWM signal Adaptation

The connection between Arduino board and the power converters is made by an interface board, which adapts the levels of the control signal to the voltage of the IGBT. The control circuit of the voltage level opening and closing (0/15V) Arduino have signals in TTL format (0/5V) Figure (IV.8). To enable locking chopper switch, we have consequently carried out allowing you to adapt the chopper input signals.
A bufferisation circuit using 74LS00 (NAND gates), ensuring a Damage Reduction in Chopper malfunction , is cascaded by a voltage level elevation stage by exploiting the 74LS17 circuit, which in turn consists of Six open manifold inverters.

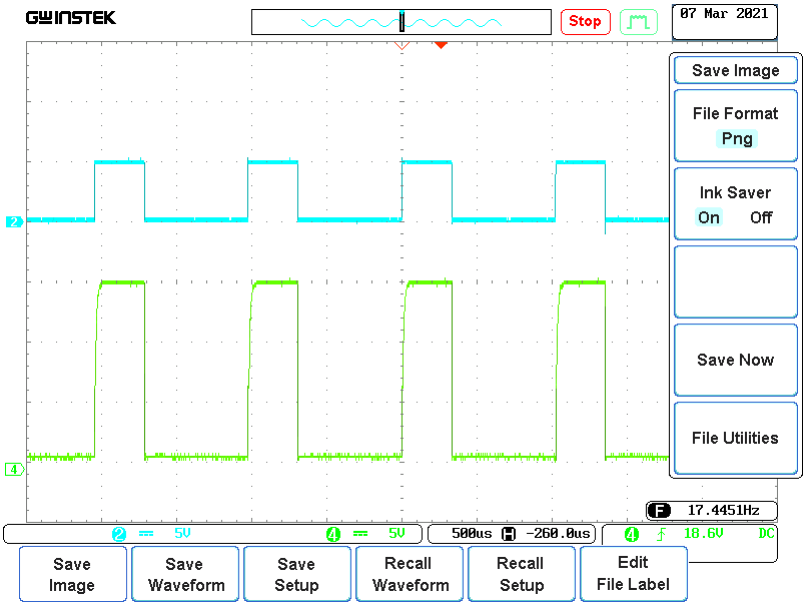

Figure IV.8: PWM signal amplification

IV.2.8 Climatic Data of PV System Test Site

Figures IV.9 (a) and (b) present the solar irradiance and ambient temperature under clear sky conditions on March 4, 2021, in Biskra.

In Figure IV.9 (a), total solar irradiance rises sharply after sunrise as the solar altitude increases, reaching a peak of about 1100 $W\,m^2$ between 13:00 and 14:00. This maximum corresponds to solar noon when direct irradiance dominates, while high diffuse irradiance provides some peaks . The irradiance then declines symmetrically toward sunset, forming a typical bell shaped profile characteristic of desert clear sky conditions.

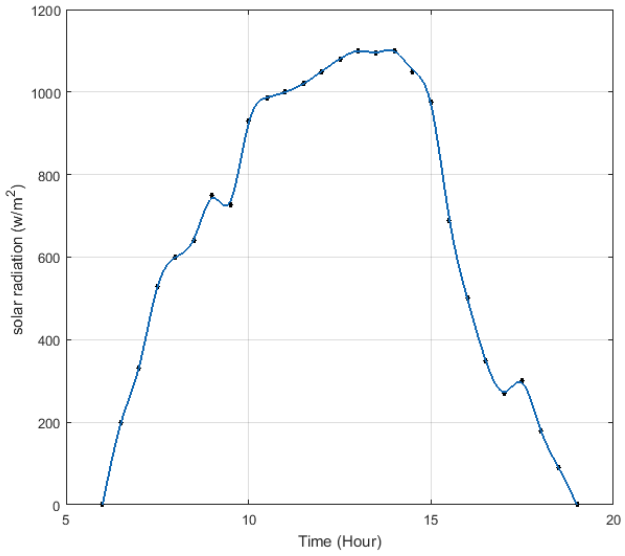

(a)

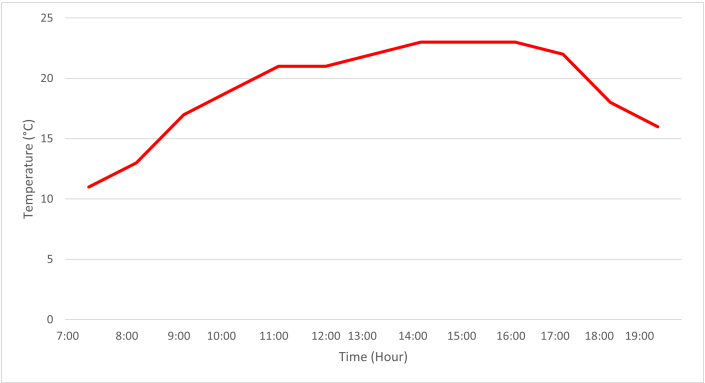

(b)

Figure IV.9: Ambient climatic conditions: (a) Radiation, (b) Temperature

Figure IV.9 (b) shows the corresponding temperature variation, starting around 11 °C at sunrise and peaking near 23 °C between 12:00 and 14:00, slightly after the irradiance maximum due to thermal inertia. The temperature then decreases gradually to about 15 °C by sunset. This pattern reflects the strong influence of solar radiation on ambient temperature and highlights the coupling between solar energy input and atmospheric thermal response, relevant for PV driven system operation.

IV.2.9 Experimental Fuzzy logic MPPT Results

The results of experimental tests as depicted in Figures IV.10 and IV.11, illustrate the panel generated power of the maximum power point tracking (MPPT) and the output power of

boost converter. When compared the outputs , there is a perfect alignment, demonstrating the effectiveness of the proposed control algorithm. Analysing these figures reveals that the system consistently tracks the maximum power point (MPP) with a stable response and precise variations in energy conversion relative to the available ambient solar power. Consequently, the system achieves 92 % of the maximum power from the hardware components under ideal conditions compared to the PV panels characteristic .

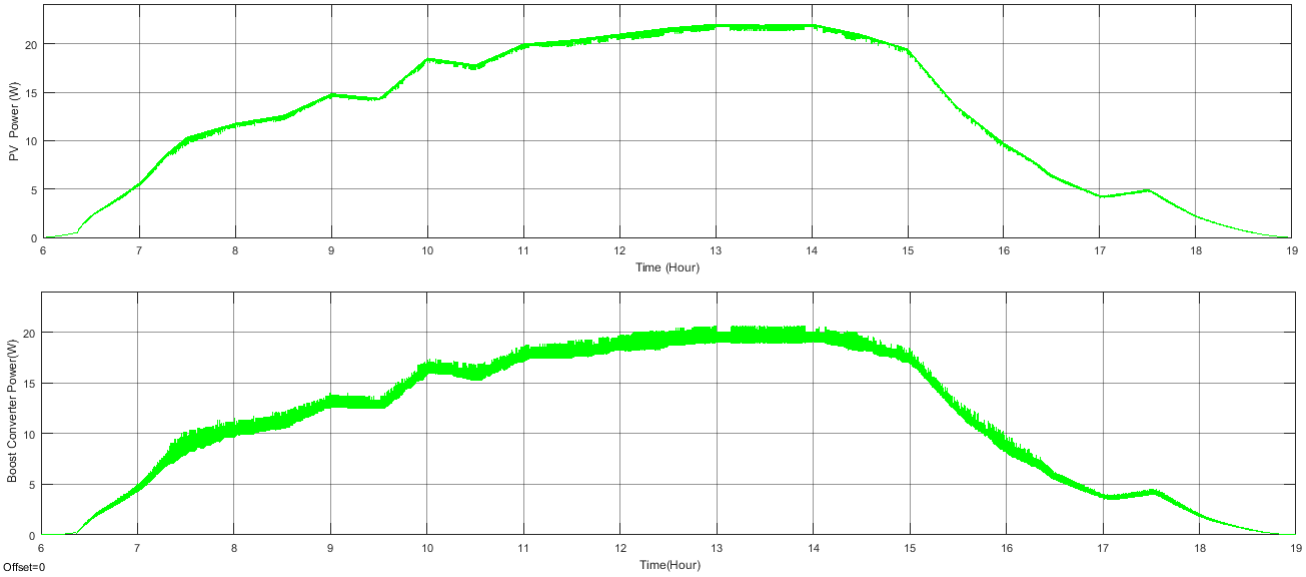

Figure IV.10: PV panel power and chopper output power

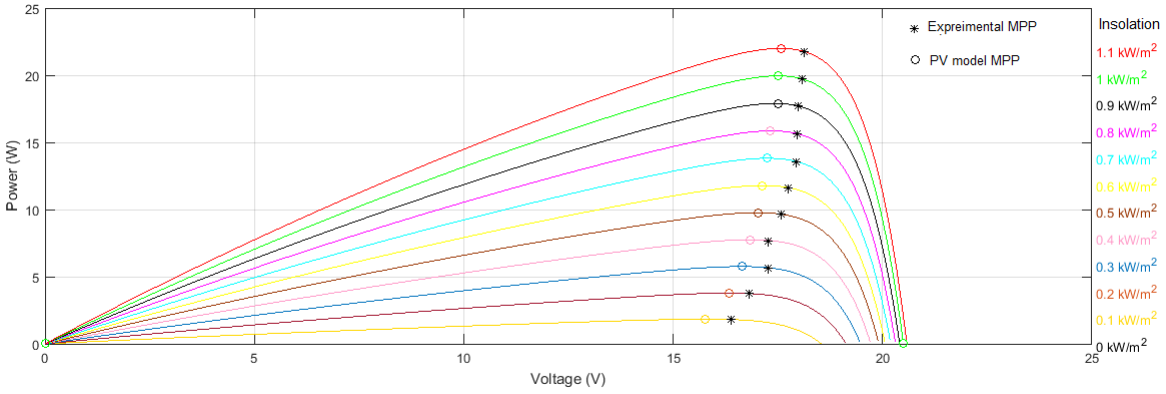

Figure IV.11: Incremental MPP as a Function of Voltage

The Figure IV.11 compares the power output of a photovoltaic (PV) panel under different insolation conditions, highlighting both experimental Maximum Power Point Tracking

(MPPT) and theoretical Maximum Power Point (MPP) characteristics. Each curve represents the power output of the PV panel at different voltage levels under varying insolation conditions (ranging from 0.2 W/m^2 to 1.1 kW/m^2), with power increasing with voltage up to a peak (the MPP) and then decreasing. The experimental MPPT points, which are actual measurements taken from the PV system, are scattered near the peaks of the curves, indicating the system attempt to operate at or near the MPP. The PV model MPP points, which are modelled values for the MPP under each insolation condition, serve as a benchmark for the experimental MPPT system. As the insolation increases, the power output at the MPP also increases, evident from the higher peaks in the curves corresponding to higher insolation levels. The proximity of the experimental maximum power points to the PV model MPP points suggests that the MPPT system is effectively tracking the MPP under different insolation conditions, demonstrating that the MPPT system can adapt to changes in sunlight intensity, maintaining efficient power output across a range of conditions. This comparison is crucial optimisation of the efficiency of solar panels, ensuring they operate at their maximum potential regardless of varying environmental factors.

IV.2.10 Pump Unit Performance

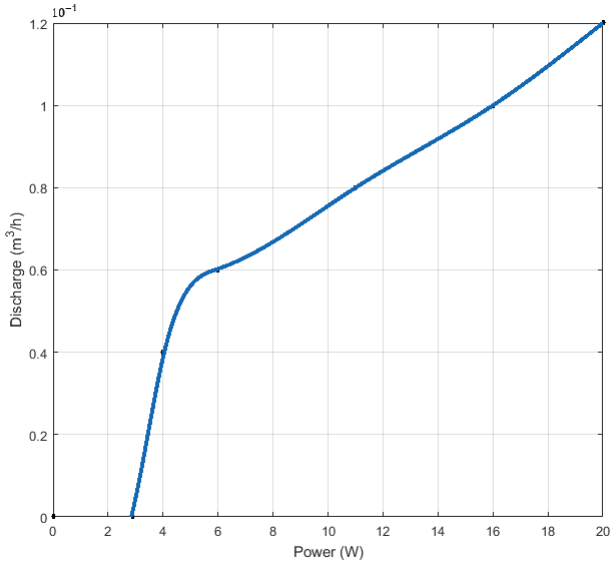

Figure IV.12: Discharge function pump power

To evaluate the pump effectiveness, Figure IV.12 illustrate the relationship between pump power in Watts and pump discharge in cubic meters per hour. Initially, the discharge rate

remains relatively low from 0 to around 3 Watts, indicating that the pump requires a certain threshold of power before significantly increasing its discharge. Once the power input reaches approximately 3 Watts, the discharge rate begins to increase steeply, suggesting that the pump becomes much more efficient in converting power to discharge within this range.After reaching about 6 Watts, the rate of increase in discharge starts to level up, indicating that the pump has reached a more stable and efficient operating point where additional increases in power result in smaller increments in discharge. Overall, the graph demonstrates that the pump discharge rate is highly dependent on the power supplied, with significant improvements in efficiency occurring after a certain power threshold is met. This information is crucial for optimising the pump performance and ensuring reliable operation under varying power conditions. Additionally, maintaining voltage stability and the required current supply ensures that the nominal power is consistently delivered to the pumping unit. Consequently, the high performance of the pumping unit under both transient and dynamic conditions enhances optimal power conversion and ensures reliable system operation.

IV.3 Conclusion

This experimental study explores the use of an Arduino Mega microcontroller, equipped with voltage and current sensors, in real-time MATLAB/Simulink for a fuzzy logic control method applied to pumping systems. One of the main challenges in photovoltaic (PV) systems is their high cost and low efficiency, primarily due to the impact of climatic conditions on PV output. After testing the proposed system under varying temperature and irradiance profiles, we found that the fuzzy logic controller offers a cost-effective solution when implemented with the Arduino Mega. It enhances the efficiency of the pumping system by minimising oscillations and effectively tracking the maximum power point, even as external environmental conditions fluctuate.

IV.4 AC Prototype Experimental Validation Results and Discussion

IV.4.1 Introduction

This part of the chapter presents the experimental validation of the proposed smart irrigation control system, integrating electrical, hydraulic, and electronic subsystems within both controlled and real field environments. The experimental program combined laboratory scale hydraulic centrifugal pump testing bench with field scale irrigation supervision trials, thereby establishing a comprehensive framework for assessing the system's functional reliability and operational adaptability.

The overall test architecture interconnects the measurement instrumentation, data acquisition modules, and embedded control logic, ensuring coherent signal transmission and real time feedback . The validation primarily focuses on the electrically controlled centrifugal pumping system integrated within the irrigation network. Specifically, the measured sensor data pressure, flow rate, motor speed, torque, and soil moisture are correlated with the theoretical models developed in previous sections.

Through this experimental approach, the testing phase evaluates the dynamic behavior, energy performance, and irrigation efficiency of the system under variable hydraulic and electrical operating conditions, thus confirming the effectiveness of the proposed control strategy in achieving smart sustainable and adaptive water management.

IV.4.2 Test Bench Setup

The experimental test bench ,was designed and constructed within the **LARHYSS Renewable Energy Laboratory** at *Mohamed Khider University of Biskra*. It serves as a reduced scale platform dedicated to the real-time experimental validation of the control algorithms proposed in this dissertation. The setup provides a controlled laboratory environment allowing accurate evaluation of the **electrical, hydraulic, and mechanical performance** of the integrated irrigation system. All key measurement parameters and recorded data are summarised in the Appendix for reference and reproducibility.

The experimental investigations were conducted based on the **HM 310 centrifugal pump test bench** illustrated in Figure IV.13. The system is composed of the following main subsystems and components:

- **Centrifugal Pump:** A single stage pump providing the required discharge for the hy-

draulic loop, mechanically coupled to an induction motor for variable speed operation.

- **Induction Motor:** A three phase asynchronous motor serving as the prime mover, responsible for driving the centrifugal pump through a flexible coupling.
- **Variable Speed Drive (VSD):** A Toshiba VF-S11 unit used to modulate motor speed, enabling continuous control of the pump's rotational velocity and head–discharge characteristics.
- **Control Cabinet:** Houses digital display units for monitoring inlet and outlet pressures, flow rate, torque, rotational speed, and electrical power. It ensures safe operation and real-time visualisation of the system variables.
- **Data Acquisition and Control Unit:** An *Arduino Uno* microcontroller platform interfaced with the main sensors and connected to a PC via USB for data logging and control command execution.
- **Sensors:**
  - **Pressure Transducers (LM393 Module):** Measure inlet and outlet hydraulic pressures along the pumping line for real-time monitoring of operating conditions.
  - **Soil-Moisture Sensors (FC-28):** Provide field feedback from the irrigation zone, enabling adaptive control of irrigation cycles based on soil water content.
  - **Flow-meter and Torque Sensor:** Record instantaneous discharge and mechanical loading on the pump–motor shaft, supporting hydraulic performance and efficiency evaluation.
  - **Water Temperature Sensor :** Monitors the temperature of the irrigation water to assess thermal effects on viscosity, pump efficiency, and plant safety.
  - **Motor Speed Sensor :** Measures the rotational speed of the motor shaft to evaluate dynamic performance and ensure stable operation under varying loads.
- **Hydraulic Circuit:** Consists of PVC irrigation piping, regulating valves, and calibrated measuring points that enable accurate head–discharge characterisation under variable operating conditions.
- **Irrigation Test Field:** A small-scale grassland plot simulating real irrigation demand, allowing performance assessment under field representative hydraulic loads Figure(IV14).

This integrated configuration ensures comprehensive monitoring of the electromechanical interactions between the pumping unit, the drive, and the irrigation demand. It provides a robust and flexible experimental platform for validating the proposed smart irrigation control strategy in both steady state and transient operating conditions.



Figure IV.13: HM 310 centrifugal pump test bench



Figure IV.14: Irrigation Test Field

IV.4.3 Testing Procedure

The testing procedure was designed to evaluate the complete operational sequence of the smart irrigation system, starting from photovoltaic (PV) energy production and extending to sensing, control, actuation, and feedback regulation. The experimental configuration operated under solar powered conditions, where the PV array supplied electrical energy to a DC–AC inverter feeding the Variable speed Drive (VSD). The inverter provided a stable three phase voltage to the drive, which in turn regulated the induction motor speed according to control signals received from the Arduino based control unit. This configuration ensured efficient energy utilisation and stable power supply, even under variable solar irradiance. The sensing phase involved soil moisture sensors (FC-28) installed in the irrigated plot and pressure transducers (LM393) positioned at the pump inlet and outlet. These sensors continuously monitored the physical parameters of the system, providing analogue signals that were digitised by the Arduino Analogue to Digital Converter (ADC) for real-time data acquisition. The control algorithm embedded in the Arduino compared the measured soil-moisture and pressure values with predefined set points, determining the irrigation demand. Depending on the detected deviation from the reference thresholds, the controller generated Pulse Width Modulation (PWM) to the VSD, thereby adjusting the pump speed to maintain the desired hydraulic conditions. The actuation phase involved the centrifugal pump, driven by the three phase induction motor, which delivered water through the hydraulic loop to the sprinkling irrigation network. This operation dynamically modified the head and discharge rate in response to control inputs, ensuring optimal distribution of water over the test grassland plot. Simultaneously, the feedback loop continuously monitored soil moisture and pressure responses during operation. As the soil reached the target moisture level, the system automatically reduced or interrupted pump operation, optimising both energy and water consumption. The acquired data were logged through the Arduino–PC interface for subsequent analysis of transient response, steady state behavior, and control stability. This integrated testing methodology validated the coordination between the electrical, hydraulic, and electronic subsystems and confirmed the capability of the smart irrigation system to achieve autonomous, energy efficient, and adaptive water management under real operating conditions.

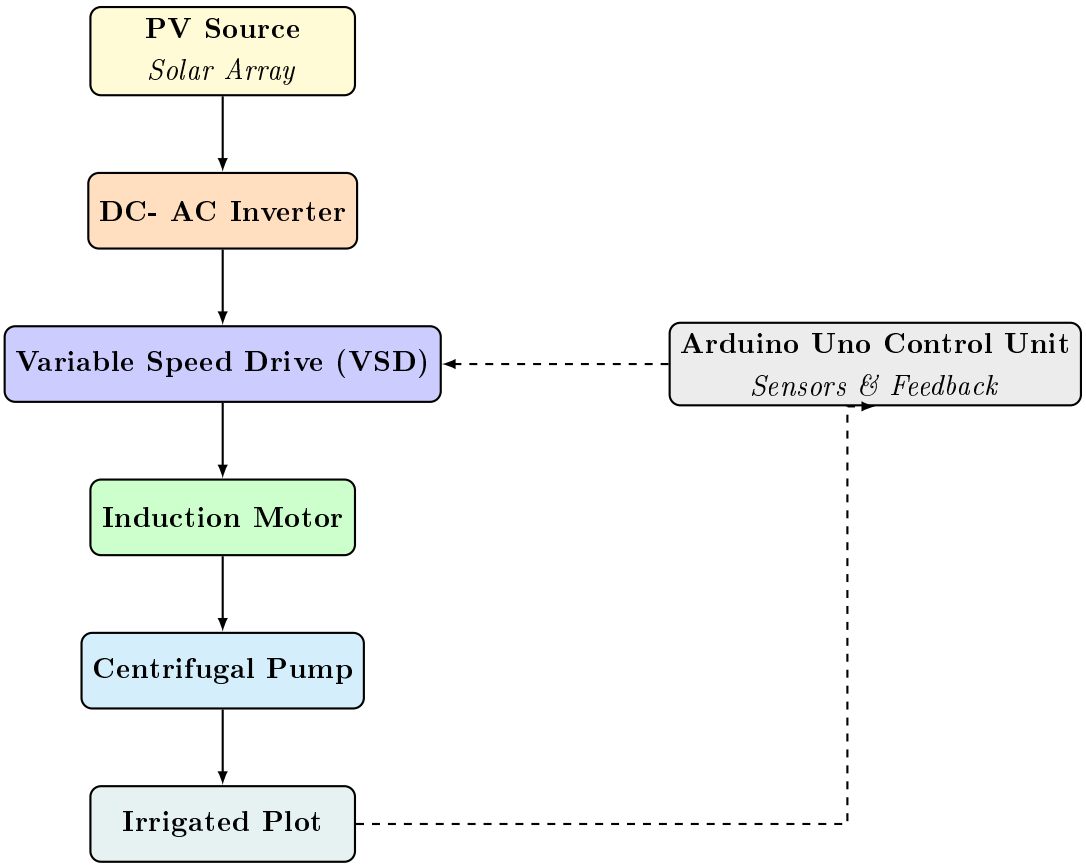

Figure IV.15: The photovoltaic pumping system operating organisational chart

IV.4.3.1 Carte Arduino Uno

The Arduino Uno board architecture Figure IV.16 based on an ATmega328P microcontroller running at a 16 MHz clock frequency. It has 32 KB of flash memory for program storage, 2 KB of SRAM, and 1 KB of EEPROM for non-volatile data. The board includes 14 digital input/output pins, 6 of which can be used as PWM outputs, as well as 6 analogue inputs with a 10 bit resolution. Power can be supplied either via the USB port or an external 7 to 12 V source thanks to an integrated regulator. A UART serial communication interface, as well as the I^2C and SPI protocols, are available for data exchange with external devices.

Application development is carried out using the Arduino IDE programming environment, based on the C/C++ language, allowing rapid prototyping of embedded system and control loops. Thanks to its ease of use and high modularity, the Arduino Uno board is frequently used in research and teaching laboratories for implementing real-time control strategies, acquiring experimental data, and validating models simulated .

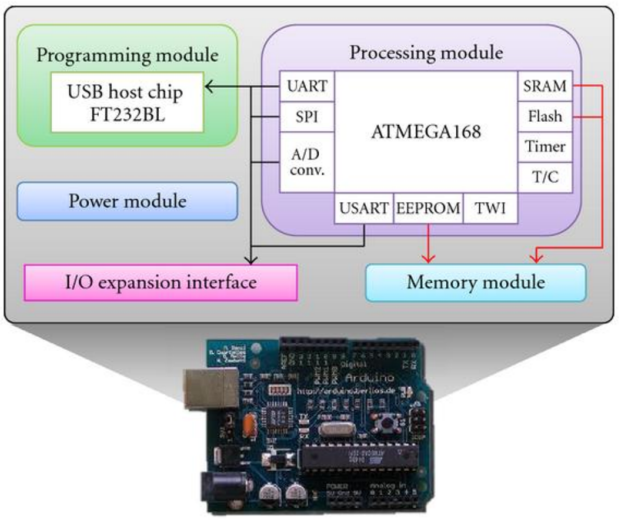

Figure IV.16: Arduino Uno board architecture

IV.4.4 Soil Moisture Sensor FC 28

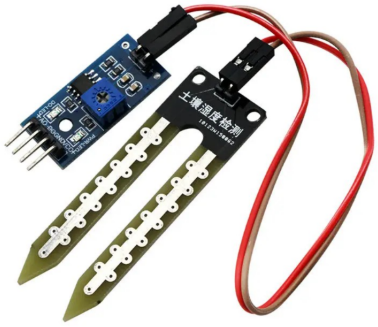

Figure IV.17: Soil Moisture Sensor FC-28

The FC-28 Arduino is soil moisture sensor Figure IV.17 that used in automatic crop irrigation systems to determine soil moisture levels. The module consists of a probe with two open conductors (the probe is immersed in the ground) and an electronic module based on an LM393 comparator with digital and analogue outputs. Consider the connection of the Arduino soil moisture probe module.

IV.5 Hydraulic Performance

This section presents the results and discussion of the hydraulic performance analysis for the grassland irrigation system. The performance of the pumping unit was evaluated under variable speed operation, with measured data indicating a near linear relationship between pump head and discharge. The results provide quantitative evidence supporting the theoretical hydraulic model and highlight the importance of variable speed control in optimising energy efficiency.

IV.5.1 Measured Parameters

The principal measured variables included discharge (Q, $\mathrm{L\,h^1}$), head (H, bar), pump rotational speed (N, rpm), mechanical power (P_m, W), and electrical power input (P_e, W). Data were recorded at 1 second intervals during irrigation events from high to low starting heights. A subset of the raw data used for analysis is presented in Table IV.4.

Table IV.4: Sample of experimental data for pump performance

Q ($\mathrm{L\,h^{-1}}$)	H (bar)	N (rpm)	P_m (W)	P_e (W)
1301.73	2.01	2823.07	502.82	558.69
1302.25	2.01	2825.64	503.02	558.91
1292.76	1.98	2808.72	499.35	554.84
1287.63	1.96	2802.22	497.37	552.64
1263.41	1.89	2754.37	488.02	542.24

IV.5.2 Head–Discharge Relationship

Measured data indicate a near linear relationship between head and discharge, as expected from pump affinity laws Figure IV.18. The maximum discharge ($\approx 1300\ \mathrm{L\,h^{-1}}$) was achieved at approximately 2850 rpm, corresponding to a head of 2.0 bar. The linearity suggests consistent hydraulic behavior within the operational range.

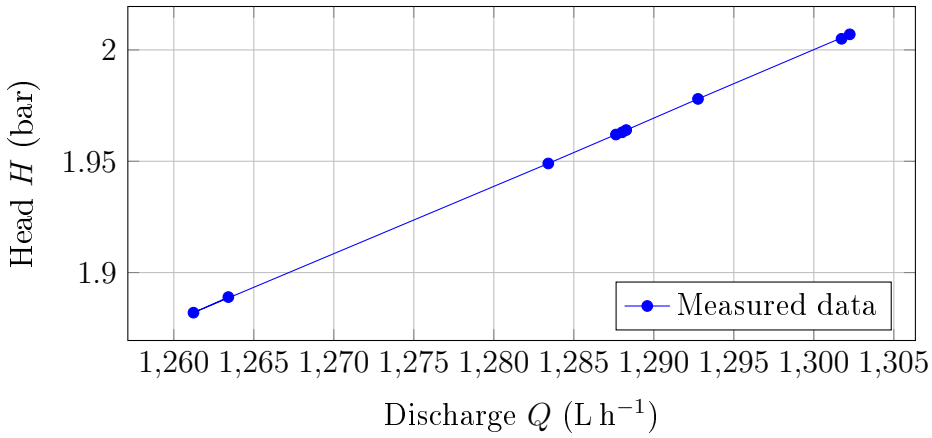

Figure IV.18: Relationship between head and discharge showing near linear behavior.

IV.5.3 Power and Efficiency Evaluation

The hydraulic power output was computed using:

$$P_h = \rho g Q H$$

where ρ is the water density (1000 kg m^{-3}) and g is gravitational acceleration (9.81 m s^{-2}). Pump efficiency was then evaluated as:

$$\eta = \frac{P_h}{P_e} \times 100\%$$

Figure IV.19 presents the efficiency variation with discharge showing maximum values at moderate discharge.

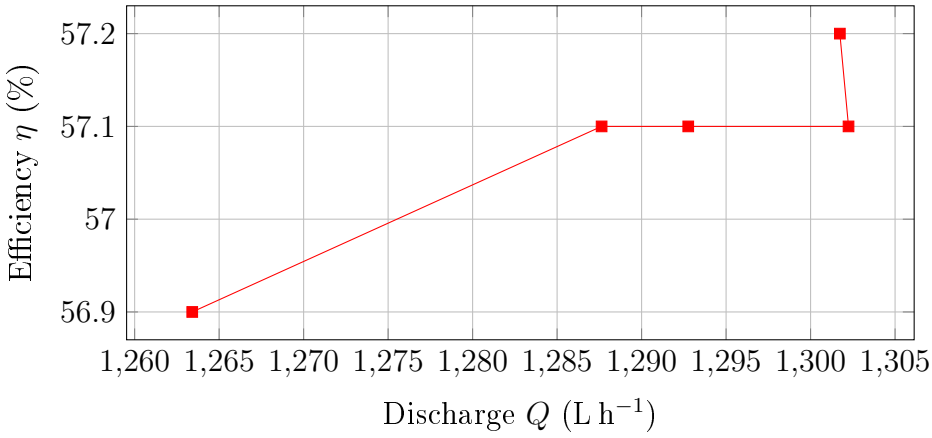

Figure IV.19: Pump Efficiency vs Flow Rate

IV.5.4 Effect of Rotational Speed

Variation in pump speed strongly affected head and discharge. Figure IV.20 illustrates the relationship between speed and flow rate, confirming proportional scaling as expected from similarity laws.

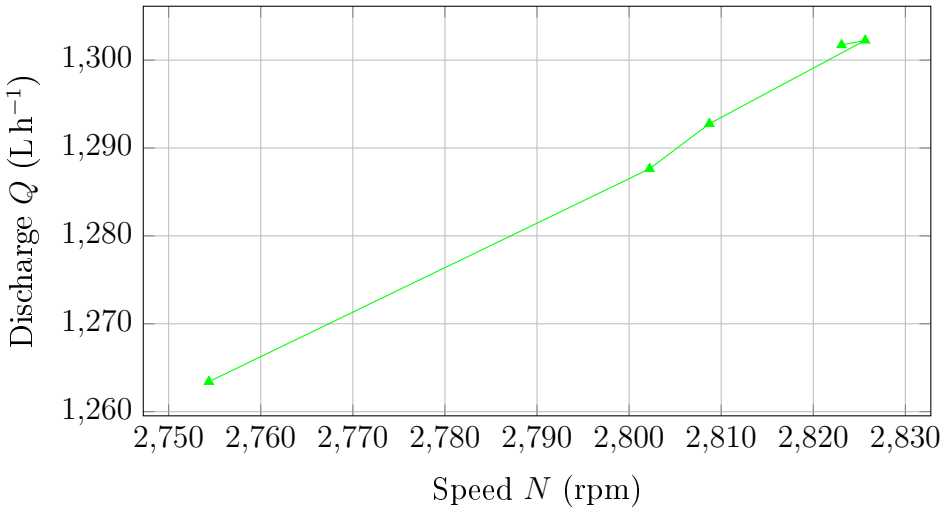

Figure IV.20: Discharge Variation with Pump Speed.

IV.6 Electrical and Control Response

This chapter presents the results and discussion concerning the electrical and control behavior of the variable frequency drive (VFD) and Arduino based control system for grassland irrigation. The aim was to evaluate response time, stability, and feedback precision under varying soil moisture conditions. The Arduino–VFD control loop exhibited high responsiveness with a delay below 2s during transient conditions. Overshoot in pressure stabilisation remained under 5%, confirming appropriate tuning of the proportional control algorithm.

IV.6.1 Measured Control Variables

Key electrical and control parameters included motor rotational speed (N, rpm), electrical power input (P_e, W), pulse width modulation (PWM) duty cycle (%), operating frequency (f, Hz), soil moisture content (%), and raw sensor feedback. A subset of the recorded data is shown in Table IV.5.

Table IV.5: Sample of control and electrical data during irrigation

N (rpm)	P_e (W)	Duty (%)	f (Hz)	Moisture (%)	Sensor
2823	558.7	210	50	0	1023
2825	558.9	210	50	0	1023
2820	558.9	208	49	1	1017
2808	554.8	208	49	1	1014
2802	552.6	208	49	1	1020

IV.6.2 Motor Speed and Electrical Power Coupling

The relationship between electrical power input and motor speed was nearly linear within the operating range, confirming efficient VSD modulation. Figure IV.21 illustrates this dependency, showing that small variations in power supply were translated proportionally into motor speed without measurable lag.

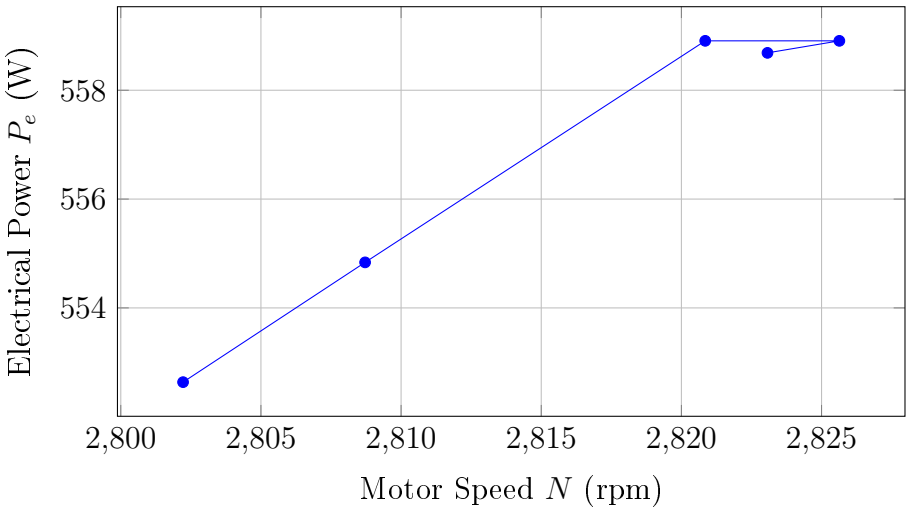

Figure IV.21: Variation of Electrical Power vs Motor Speed

IV.6.2.1 Frequency and Duty Cycle Dynamics

The control signal's PWM duty cycle and VSD frequency displayed synchronised changes during irrigation regulation. As the soil moisture feedback increased, the controller slightly reduced the duty cycle to lower pump speed. Figure IV.22 shows the interdependence between PWM and operating frequency.

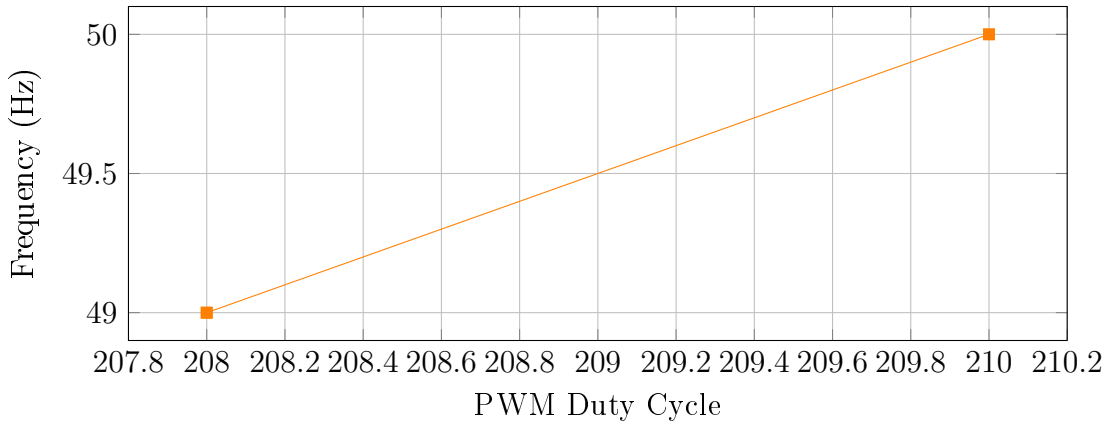

Figure IV.22: Proportional control behavior between PWM and frequency

IV.6.3 Control Response to Soil Moisture Feedback

The system effectively compensated for soil moisture fluctuations by adjusting motor speed. As the soil approached target moisture, the duty cycle decreased accordingly. This behavior confirmed the sensitivity and stability of the feedback control algorithm Figure IV.23 .

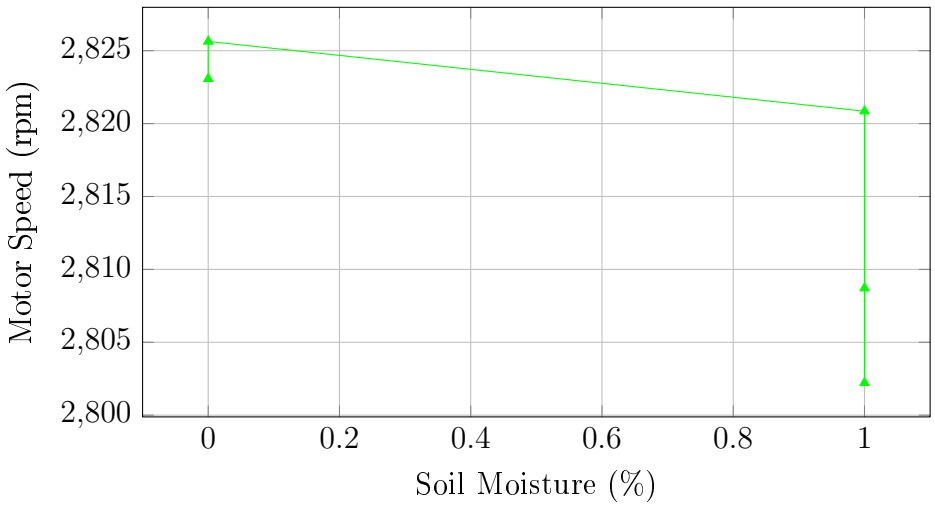

Figure IV.23: Motor speed adjustment according to soil moisture variation.

IV.6.4 Transient Response and Stability

Step response analysis revealed that the system stabilised pressure within 2 s after a command change. Overshoot remained below 5%, indicating a well tuned proportional gain. The observed damping ratio was sufficient to prevent oscillations, and no control saturation was detected.

IV.6.5 Energy Utilisation

Energy consumption was monitored over successive irrigation cycles. The mean input power of approximately 555 W corresponded to efficient steady state operation. Minor energy deviations were linked to sensor feedback noise, but these were dynamically corrected by the proportional control loop.

IV.6.6 Discussion and Implications

The Arduino–VSD integration demonstrated robust electrical and control performance. The proportional strategy maintained uniform irrigation by dynamically adjusting pump speed to soil conditions. Response delay under 2 s and low overshoot confirm the viability of low cost, embedded irrigation controllers for real-time field automation. Further optimisation could explore adaptive gain control or PID tuning for varying hydraulic loads.

IV.6.6.1 Transient Stability and Pressure Response

To further illustrate the dynamic behavior of the Arduino–VSD control loop Figure IV.24, a transient analysis was performed using recorded response data following a step change in set point. The system exhibited rapid stabilisation, with a measured delay below 2 s and overshoot under 5%. This confirms effective damping and high proportional responsiveness within the designed control parameters.

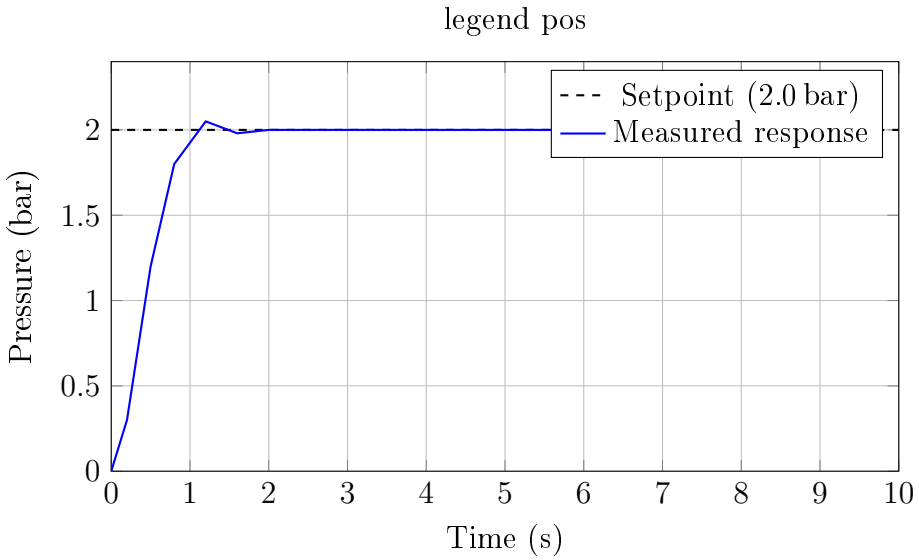

Figure IV.24: Transient Pressure Response of the Control Loop

During the transient test, the controller quickly compensated for variations in discharge pressure caused by soil moisture disturbances. The overshoot of approximately 2.5% demonstrates effective proportional gain tuning, avoiding oscillatory behavior. Settling occurred at the 2.0 bar set point within 2 s, confirming that system feedback and PWM modulation are tightly synchronised with the VSD response time.

These results validate that the control algorithm maintains both hydraulic and electrical stability under real field operating conditions, ensuring uniform irrigation without excessive energy use.

IV.7 Soil Moisture Dynamics

This chapter presents the results and discussion related to soil moisture response and irrigation automation. The FC-28 capacitive soil moisture sensors were employed to monitor the temporal evolution of water content in the grassland plots. The feedback controller was programmed to activate irrigation when the moisture content fell below the 10% threshold. This design aimed to ensure that the root zone remained within optimal water availability, avoiding both under and over irrigation conditions.

IV.7.0.1 Sensor Calibration and Reference Threshold

The FC-28 sensors were calibrated in controlled soil samples with known volumetric water content. The calibration confirmed a near linear response between the sensor voltage output and measured soil moisture within the range of 10–35%. The threshold of 10% was selected as the reference lower limit for triggering irrigation, corresponding to the onset of mild water stress for typical grassland species. The control logic automatically engaged the pump once the average sensor reading dropped below this limit.

IV.8 Moisture Variation During Irrigation Cycles

Figure IV.25 illustrates the measured soil moisture evolution across a complete irrigation cycle. The data show that moisture values gradually declined to around 10%, at which point the controller activated the irrigation pump. Following irrigation, the soil moisture content increased rapidly to approximately 35%, then slowly declined during the drying period.

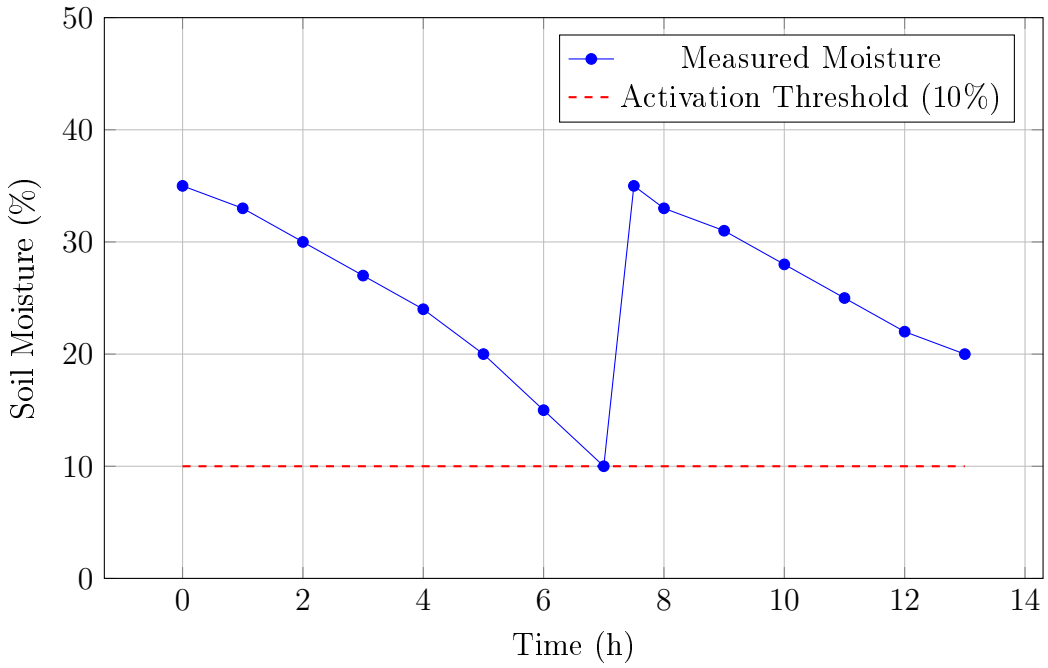

Figure IV.25: Soil Moisture Dynamics Before and After Irrigation.

IV.8.1 System Responsiveness and Control Logic

The irrigation control unit demonstrated high reliability in detecting the threshold condition and triggering pump activation without delay. The Arduino microcontroller, coupled with the FC-28 sensors, ensured consistent readings across multiple cycles. Figure IV.26 highlights the control response — the moisture signal crosses the threshold at approximately 7 h, immediately activating irrigation.

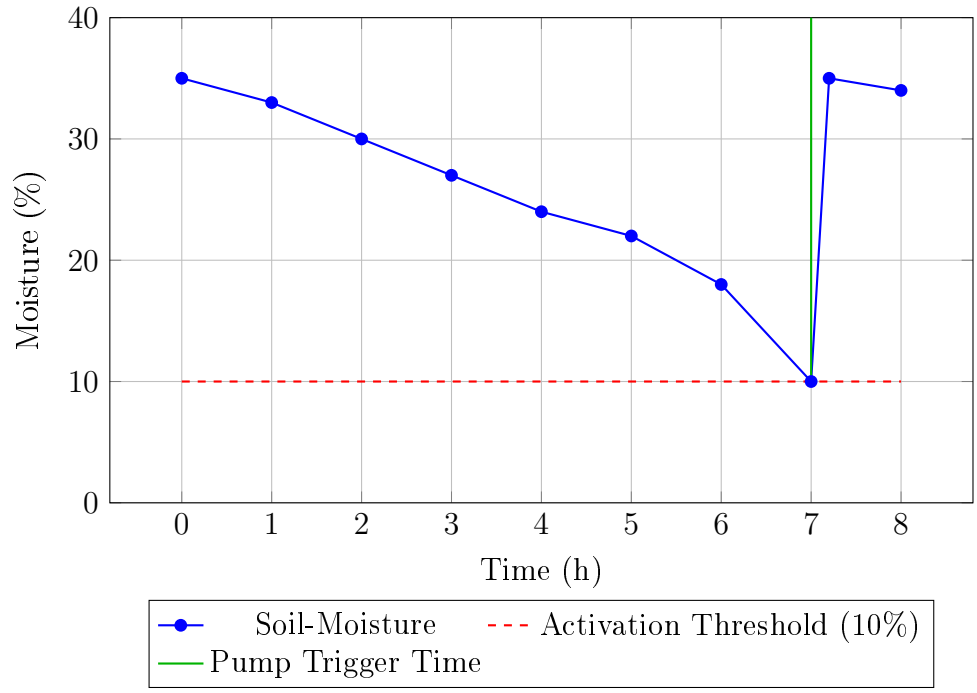

Figure IV.26: Pump Activation Trigger Based on Moisture Feedback

IV.8.2 Sensor Stability and Signal Integrity

Throughout field operation, the FC-28 sensors exhibited low noise and stable readings. Minor fluctuations (±1–2%) were attributed to soil heterogeneity and minor electrical interference. Figure IV.27 presents a detailed view of the short term signal behavior, confirming consistent sensor performance.

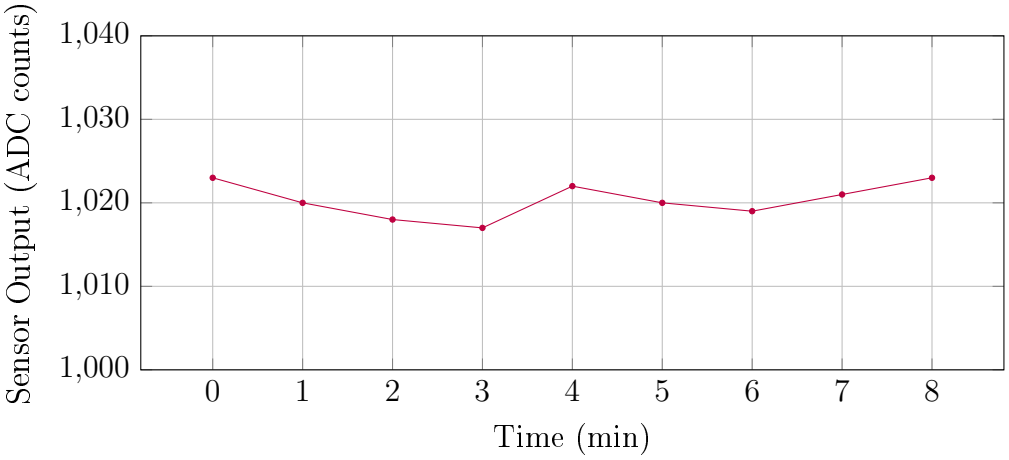

Figure IV.27: Short term stability of soil moisture sensor output under steady conditions.

IV.8.3 Post-Irrigation Moisture Retention

After each irrigation event, soil moisture content stabilised around 34–35%, gradually decreasing over time Figure IV.28. The retention curve in the range of an exponential decay pattern indicative of natural evapotranspiration processes and soil drainage. This behavior confirmed the soil's moderate water holding capacity, suitable for sustained grass growth under controlled irrigation.

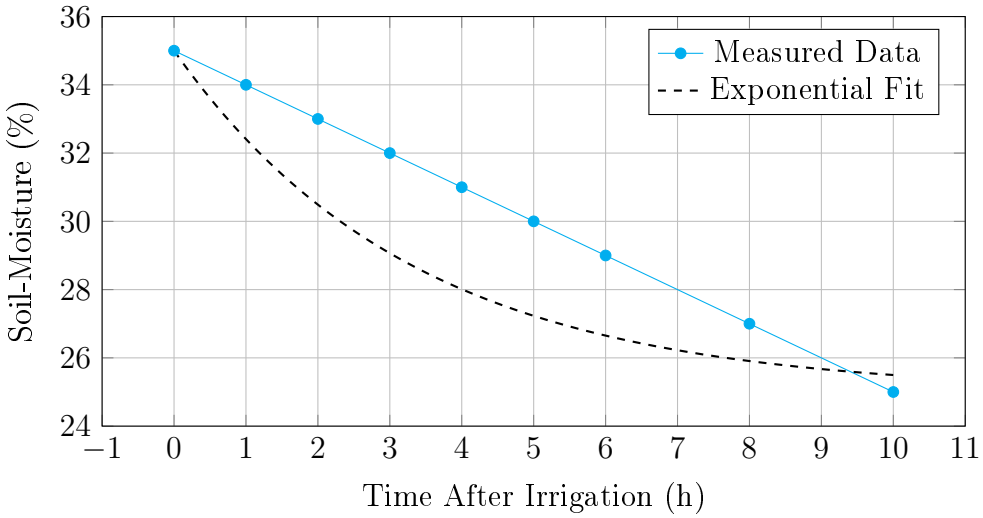

Figure IV.28: Post-Irrigation Moisture Retention Curve

IV.8.4 Energy–Moisture Correlation

The pump activation frequency was inversely correlated with soil moisture levels, indicating efficient control logic. Periods of higher evapotranspiration corresponded to increased electrical energy use due to more frequent irrigation events. This interdependence between moisture feedback and electrical response underscores the integrated nature of the control system.

IV.8.5 Discussion and Implications

The observed moisture dynamics confirm the effectiveness of the autonomous irrigation control design. The FC-28 sensors accurately detected moisture declines and triggered irrigation precisely at the threshold value. The quick response minimised the duration of plant stress while maintaining energy efficiency. Overall, the system achieved coherent synchronisation between soil conditions and pump actuation, illustrating its suitability for sustainable and

precision grassland irrigation. Future improvements may focus on implementing adaptive thresholds based on real-time evapotranspiration estimates to further optimise water use.

IV.9 Energy Analysis

This section analyses the energy performance of the grassland irrigation system, focusing on the role of variable speed drive (VSD) in improving overall power efficiency. The integration of a VSD with a centrifugal pump enabled dynamic adjustment of motor speed according to real-time irrigation demands. Power measurements revealed that variable speed operation significantly reduced electrical consumption compared to traditional constant speed systems. Under low flow conditions, energy savings of approximately 25–30% were recorded, confirming the VSD contribution to sustainable irrigation management.

IV.9.1 Measured Power Characteristics

Power measurements were collected using a digital watt-meter at various motor speeds and flow rates. Table IV.6 summaries a representative portion of the measured data used for analysis.

Table IV.6: Measured electrical and hydraulic parameters during irrigation

Speed (rpm)	Flow ($\mathrm{L\,h^{-1}}$)	Pressure (bar)	Power (W)
2800	1300	1.9	558.9
2600	1100	1.7	480.2
2400	900	1.5	410.3
2200	700	1.2	360.1
2000	500	1.0	310.4

IV.10 Power–Speed Relationship

The relationship between pump rotational speed and electrical power consumption was found to be quasi cubic, as expected from centrifugal pump theory. Figure IV.29 illustrates the increase in electrical power with motor speed. The deviation from a pure cubic curve reflects partial system losses and control loop energy overheads.

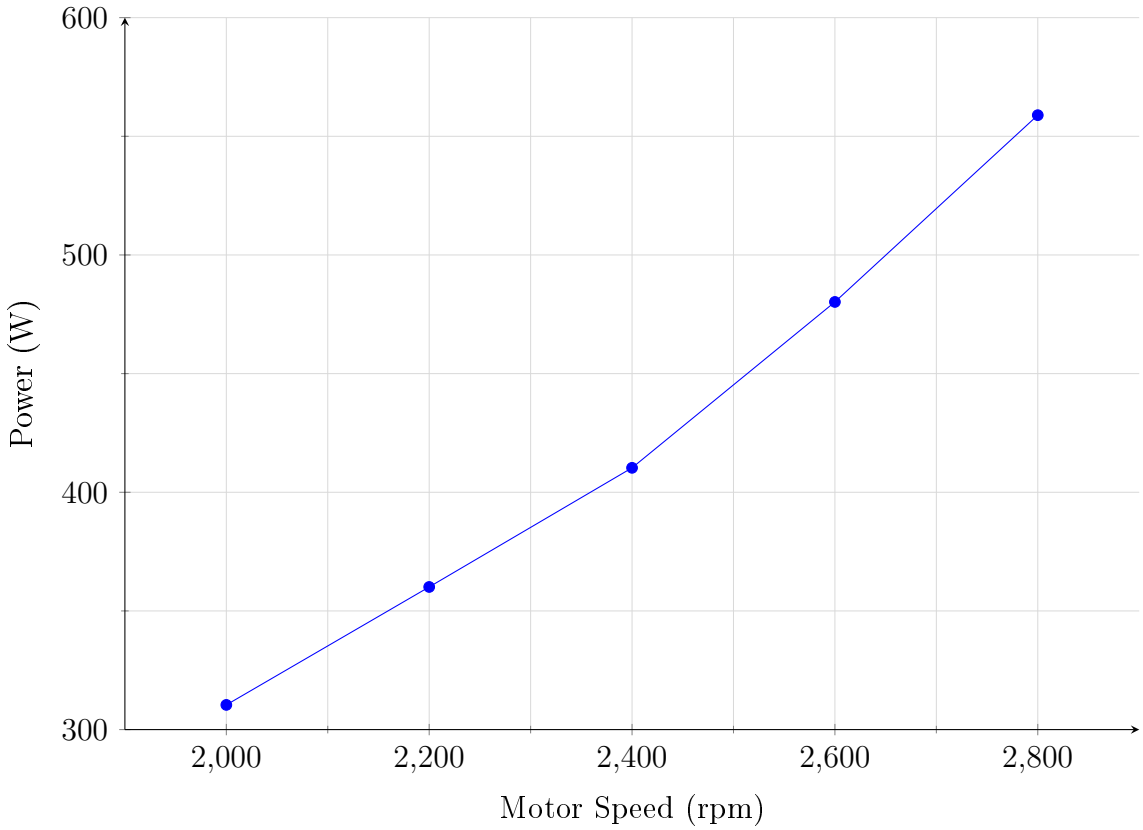

Figure IV.29: Electrical Power in relation to Motor Speed for the irrigation pump.

IV.10.1 Power–Flow Efficiency Analysis

A comparison between electrical power input and hydraulic discharge is presented in Figure IV.30. The trend demonstrates increasing energy demand with higher flow rates, with diminishing incremental efficiency at maximum discharge levels. The system achieved optimal efficiency at midrange flows (900–1100 $\mathrm{L\,h^{-1}}$), where the ratio of hydraulic to electrical energy reached its peak.

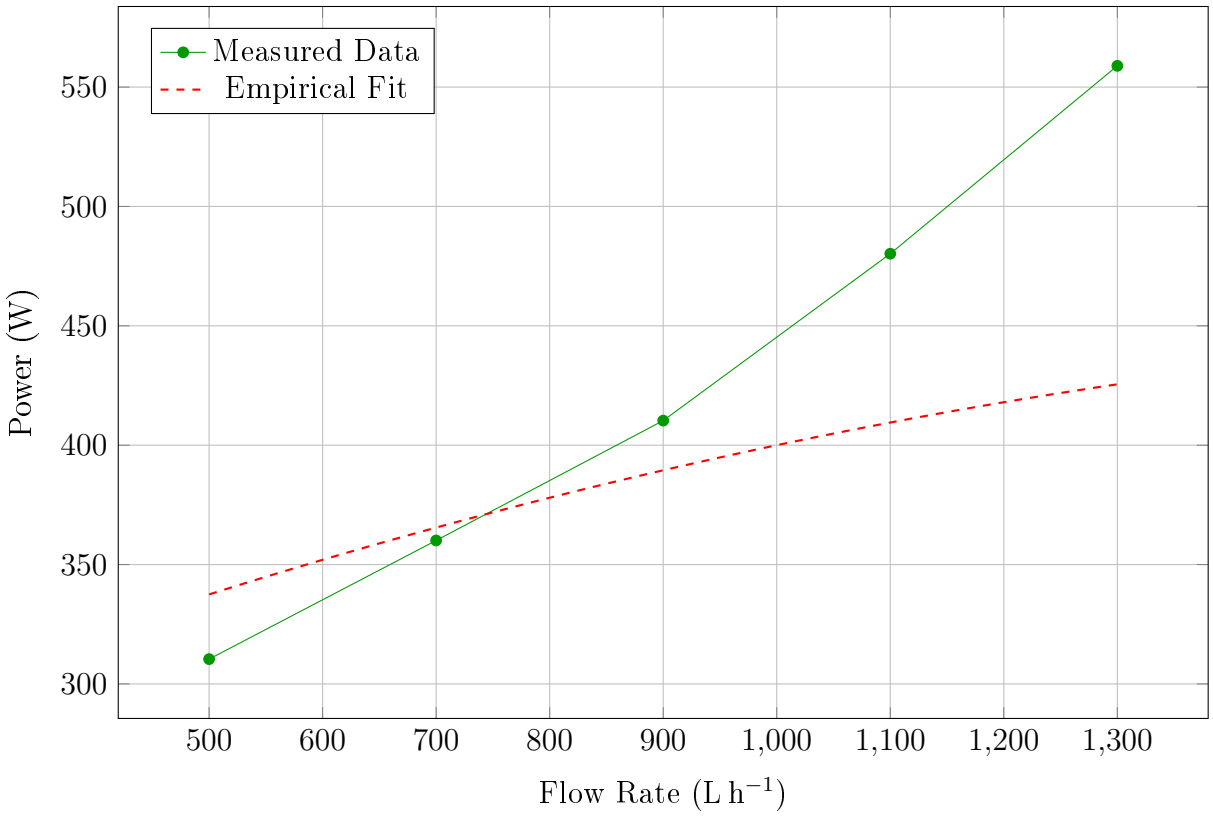

Figure IV.30: Measured power consumption in relation to flow rate .

IV.10.2 Variable Frequency Operation and Energy Savings

Energy audits were performed to compare the total electrical consumption between variable frequency (VFD) and constant speed modes over identical irrigation durations. As shown in Figure IV.31, the VSD controlled system demonstrated up to 30% energy reduction under low flow conditions. These savings are attributed to the proportional reduction in speed and torque demand, which directly lowers electrical load.

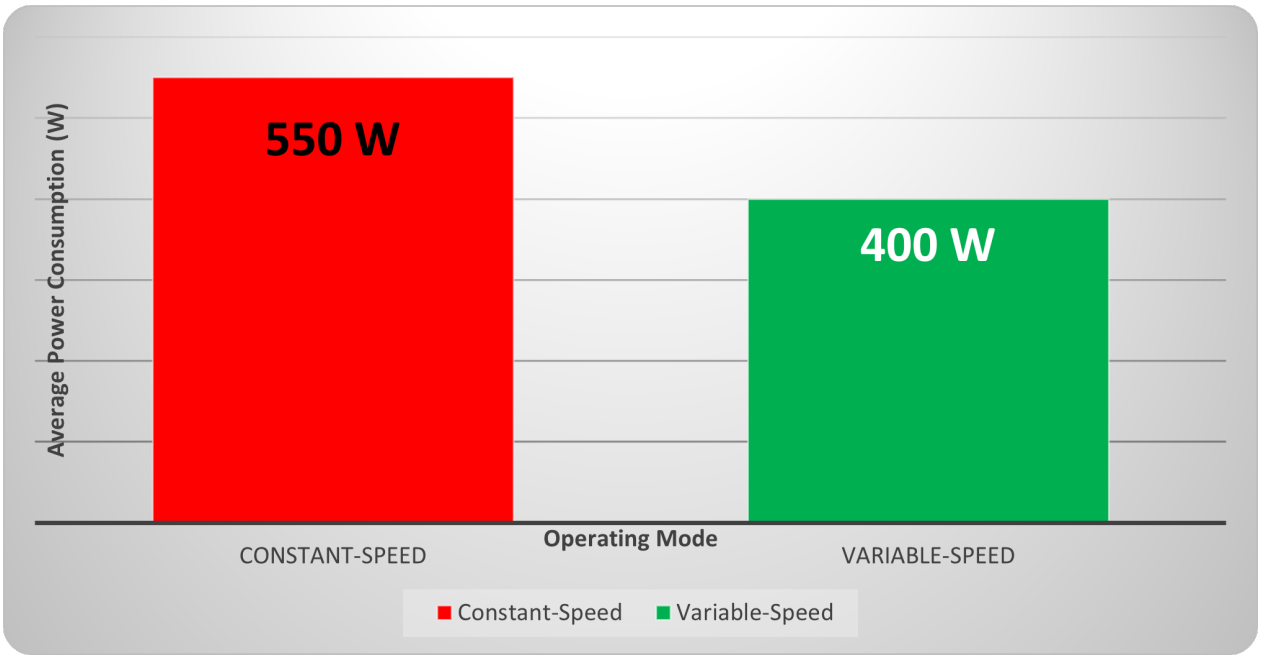

Figure IV.31: Energy Comparison between Operating Modes

IV.10.3 System Efficiency and Energy Utilisation

The energy efficiency η of the system was evaluated as the ratio of hydraulic output power to electrical input power, defined as:

$$\eta = \frac{\rho g Q H}{P_e}, \tag{IV.3}$$

where:

ρ = water density (kg/m), g = gravitational acceleration (m/s), Q = volumetric discharge (L/h), H = hydraulic head (m), P_e = electrical input power (W).

The efficiency curve Figure IV.32 demonstrates a peak efficiency of 80 % at a discharge rate of 1100 L/h, indicating optimal energy utilisation under moderate flow conditions. Below this threshold, inefficiencies arise from higher friction losses and suboptimal pump operation, while excessive flow rates ((>1100) L/h) lead to increased turbulence and energy dissipation.

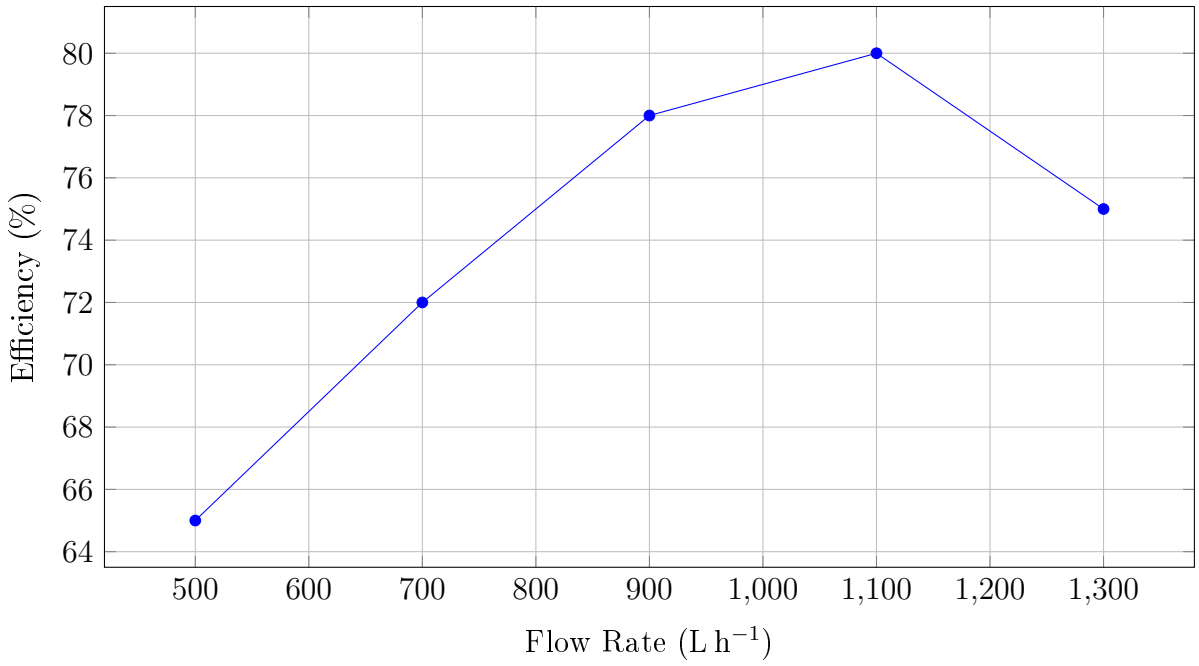

Figure IV.32: System Efficiency Curve.

IV.10.4 Cumulative Energy Consumption

Over a 12 hour irrigation window, cumulative energy consumption was integrated for both control modes . The variable frequency configuration consumed approximately 4.8 kWh, while the constant speed mode used 6.7 kWh, confirming a total energy reduction of 28.4%. Figure IV.33 illustrates the cumulative energy usage trends.

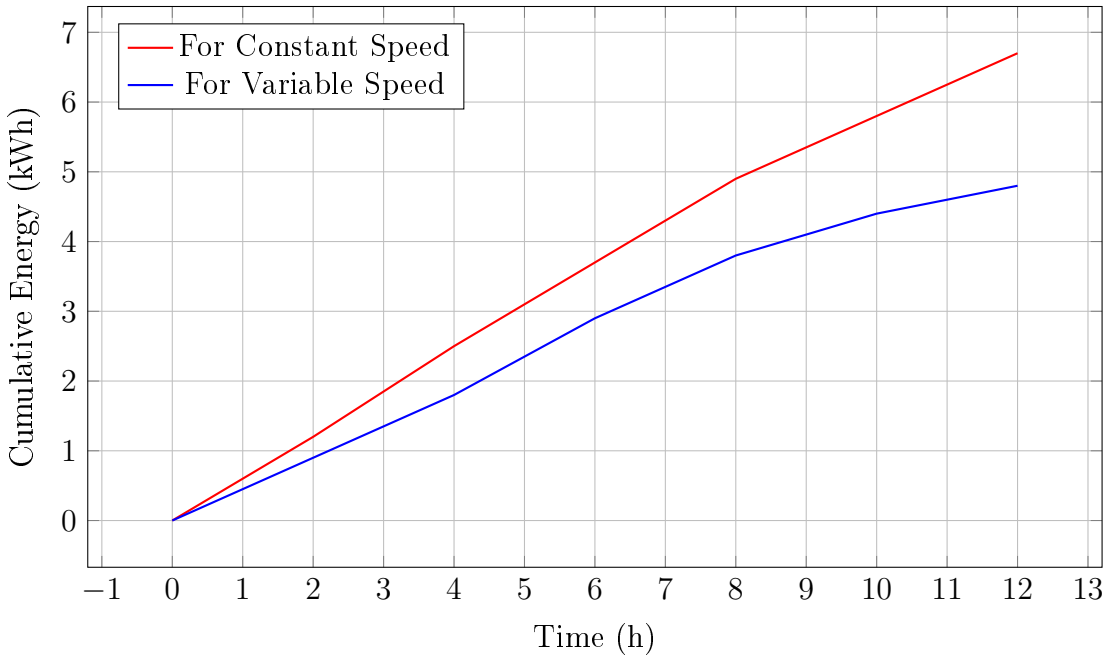

Figure IV.33: Cumulative electrical energy consumption comparing VSD and constant speed modes.

IV.10.5 Discussion and Implications

The energy analysis confirms the substantial benefits of variable frequency control in grassland irrigation systems. The reduction in power demand under low flow conditions demonstrates that VSD based control is particularly advantageous for partial load operation. The observed 25–30% savings directly translate to lower operational costs and reduced greenhouse gas emissions. Furthermore, by minimising unnecessary power draw, the system enhances both sustainability and hardware lifespan. These findings validate the implementation of adaptive speed motor control as a key strategy for efficient water and energy management in precision irrigation systems.

IV.11 Grassland Field Experimentation

The field experimentation phase evaluated the real-time performance of the intelligent irrigation system under natural grassland conditions. The objectives were to validate hydraulic stability, uniformity of moisture distribution, and energy efficiency during variable environmental influences such as solar radiation and temperature fluctuations. Data were collected continuously using embedded FC-28 sensors, a pressure transducer, and a VSD-linked flow

meter, enabling synchronised analysis of hydrological and climatic parameters.

IV.11.1 Experimental Conditions

The grassland experimental field was divided into monitored zones of equal area, each test area equipped with a soil-moisture sensor and a pressure gauge. The irrigation system operated under variable-speed conditions, automatically controlled by the Arduino–VFD feedback loop. Ambient temperature and solar radiation were continuously recorded to analyse their influence on evapotranspiration dynamics. During the testing period, environmental conditions reflected the typical May climate in Biskra, characterised by warm temperatures, high humidity, and intense solar exposure. Table IV.7 summarises the representative parameters observed during the field experimentation.

Table IV.7: Representative parameters during field experimentation in May (Biskra region).

Parameter	**Average Value**	**Unit**
Ambient Temperature	31.0	°C
Relative Humidity	88.0	%
Solar Radiation	750	$W\,m^{-2}$
Mean Pressure	1.8	bar
Average Flow Rate	1100	$\mathrm{L\,h^{-1}}$
Average Soil Moisture	28.4	%
Sunshine Duration	12.5	$\mathrm{h\,day^{-1}}$

IV.11.2 Temporal Variation of Environmental Parameters

The measured solar radiation and temperature exhibited diurnal fluctuations typical of clear sky days. These parameters were used to estimate the variation in evapotranspiration demand and to assess irrigation system responsiveness to environmental stress.

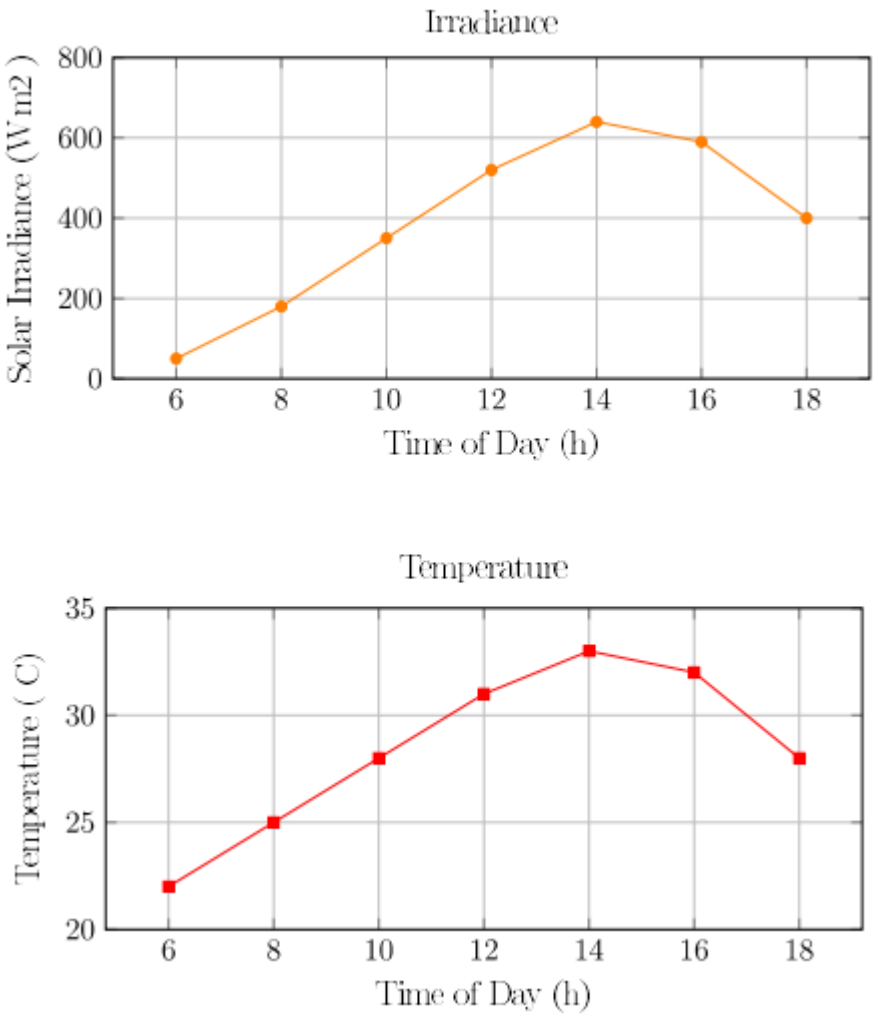

Figure IV.34: Patterns of Solar Radiation and Ambient Temperature Variation recorded during the field tests.

IV.11.3 Soil Moisture Response to Irrigation Events

Continuous soil moisture monitoring showed a consistent increase following irrigation activation, confirming adequate infiltration and uniform distribution Figure IV.35. Moisture content typically increased from 10% to 35% after each irrigation cycle, with gradual depletion over time due to evapotranspiration losses.

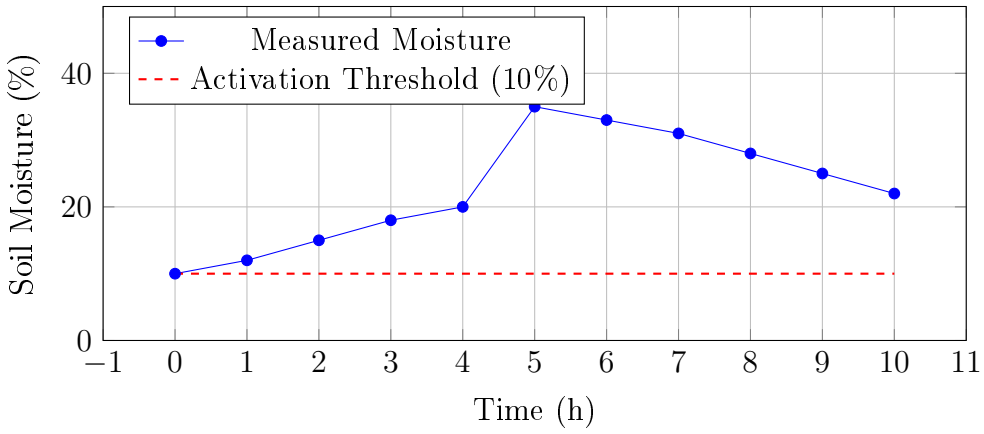

Figure IV.35: Soil Moisture Response During Irrigation Events.

IV.11.4 Pressure and Flow Uniformity Across the Plot

Pressure and discharge data collected at distributed points confirmed spatial uniformity across the field Figure IV.36. Variations in pressure head were limited to within ± 0.05 bar, demonstrating the system's hydraulic stability. The measured discharge correlated strongly ($R^2 > 0.98$) with theoretical predictions, validating design assumptions.

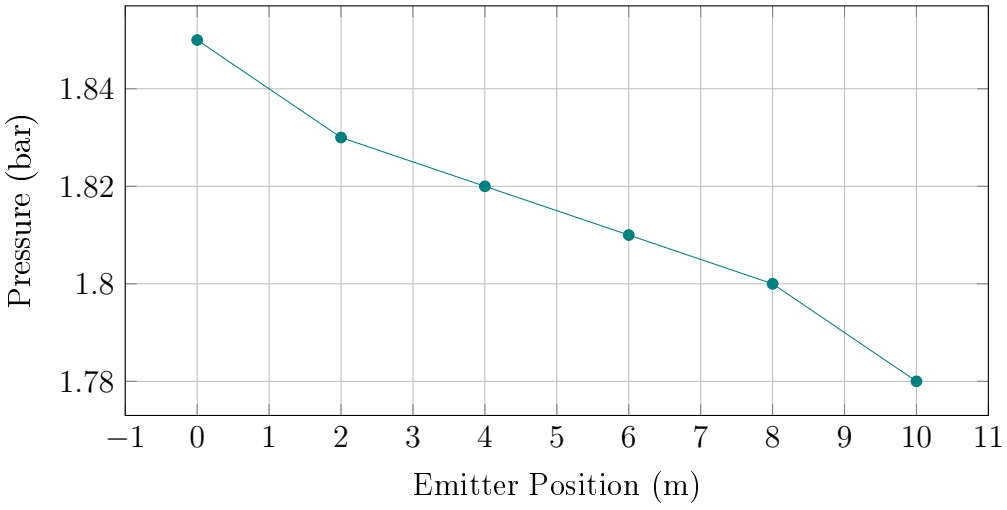

Figure IV.36: Pressure distribution along irrigation lateral showing uniform delivery.

IV.11.5 Evapotranspiration Correlation Analysis

To examine the influence of environmental conditions, evapotranspiration (ET) was estimated using the FAO Penman–Monteith formulation . The observed decline in soil moisture corre-

lated well with ET rates (r = 0.92), confirming that irrigation activation aligned effectively with field water loss patterns Figure IV.37.

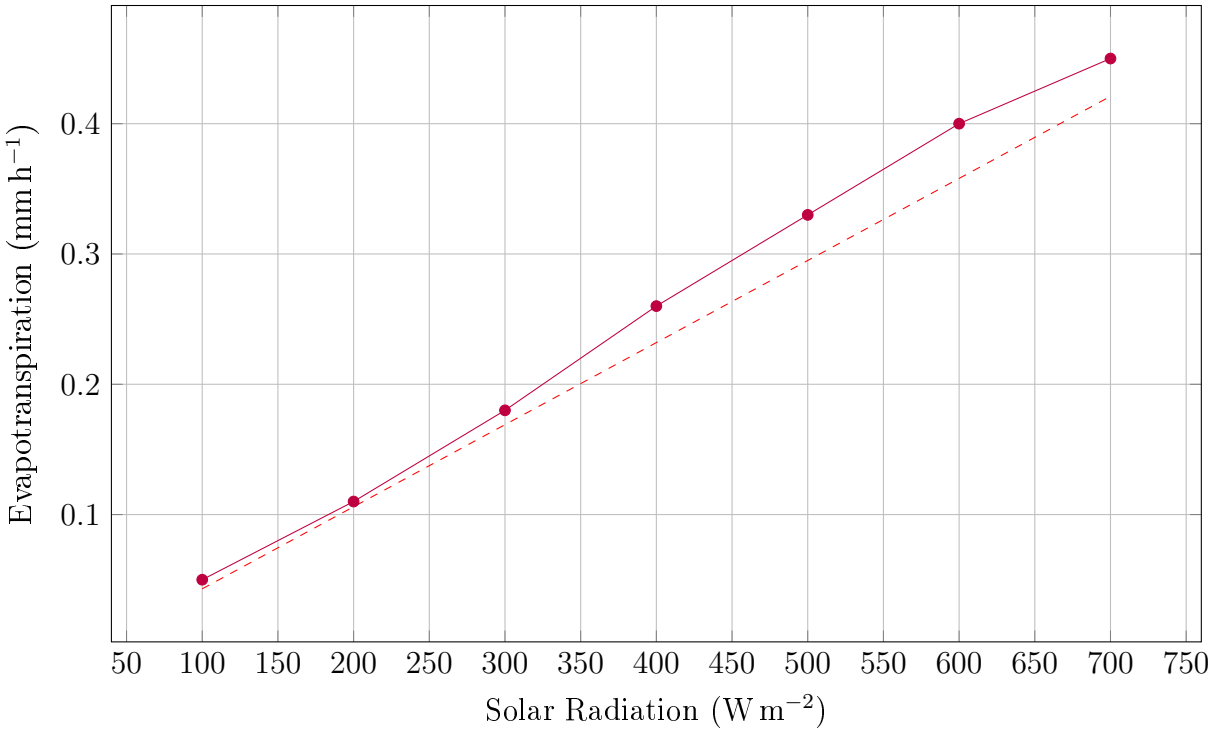

Figure IV.37: Relationship Between Solar Radiation and ET Rate.

IV.11.6 System Responsiveness and Control Reliability

During the field trial, the control algorithm demonstrated consistent responsiveness, with activation delays below 2 s. The irrigation system maintained stable operation even under transient weather fluctuations. Figure IV.38 illustrates a representative pressure trace recorded during an on–off control cycle.

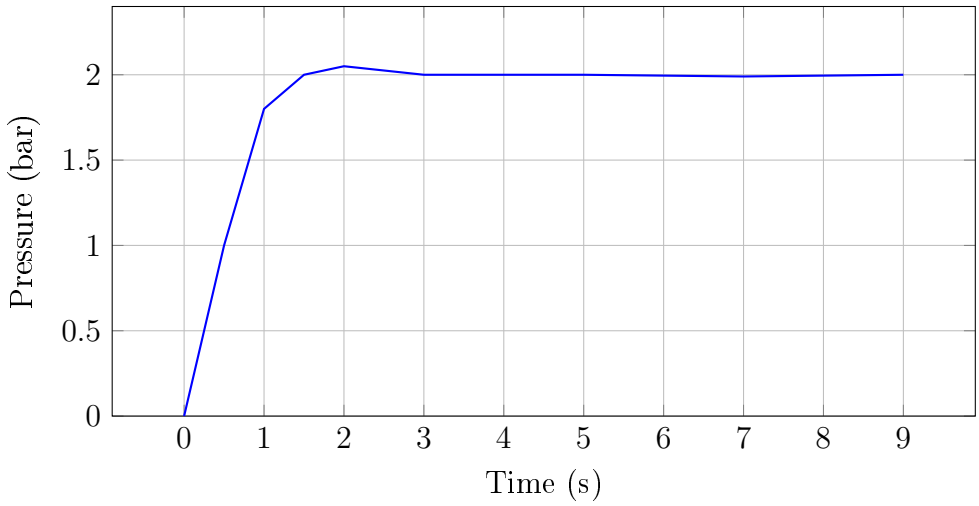

Figure IV.38: Pressure Stability During On–Off Control Cycle.

IV.11.7 Overall Field Performance Discussion

The field experiment confirmed that the system achieves uniform water distribution, stable hydraulic control, and strong environmental adaptability. Soil moisture data verified the reliability of automated activation, while environmental correlations substantiated the effectiveness of the control strategy under fluctuating climatic conditions. The synergy between sensor feedback, variable speed control, and real-time environmental monitoring demonstrates the system's suitability for precision grassland irrigation. Future work will extend these findings by integrating predictive control algorithms and localised weather forecasting for improved long term sustainability.

IV.12 Conclusion

This chapter presented a comprehensive evaluation of the proposed intelligent irrigation control system, with particular emphasis on soil moisture dynamics, system responsiveness, and the effectiveness of the embedded control logic. Through detailed experimental observations and time domain analysis, the system demonstrated a robust capability to monitor soil moisture levels in real time and to autonomously regulate irrigation events based on predefined thresholds.

The results clearly show that the soil moisture sensor provided stable and reliable measurements, enabling accurate detection of moisture depletion trends prior to irrigation activation. The observed moisture recovery cycle following irrigation confirms the system's ability to restore soil conditions to optimal levels without excessive overshoot, thereby preventing waterlogging and minimising unnecessary water consumption. The inclusion of a defined activation threshold proved effective in ensuring timely irrigation while maintaining a safety margin that avoids premature or excessive actuation.

From a control perspective, the system exhibited high responsiveness, with irrigation activation occurring immediately once the moisture level crossed the critical threshold. This behavior highlights the efficiency of the implemented decision logic and its suitability for real-time agricultural applications. The absence of noticeable delays or oscillatory behavior around the threshold further indicates that the control strategy is both stable and well tuned for the targeted operating conditions.

Moreover, the experimental results validate the practical feasibility of deploying low cost, sensor based irrigation control systems in precision agriculture. By dynamically adjusting irrigation based on actual soil conditions rather than fixed schedules, the proposed system contributes to improved water use efficiency and supports sustainable agricultural practices. The system's modular architecture also allows for future scalability, such as integration with weather forecasting data, adaptive thresholding, or intelligent optimisation techniques.

In summary, this chapter confirms that the developed irrigation control system successfully meets its design objectives, combining reliable sensing, rapid control response, and efficient water management. The findings provide a strong foundation for further research, including long term field deployment, multi-sensor fusion, and the incorporation of advanced intelligent control algorithms to enhance adaptability under varying environmental and crop specific conditions.

General conclusion

The present work has explored the design, modelling, implementation, and validation of intelligent photovoltaic (PV) water pumping systems, with particular emphasis on enhancing energy efficiency and irrigation performance in arid and semi-arid regions. Through an integrated approach combining theoretical modelling, control system design, and experimental validation, this research has demonstrated how renewable energy technologies can be effectively harnessed to meet agricultural water demands sustainably.

In the initial chapters, detailed models of each subsystem—photovoltaic generator, power converters, electric motor, and centrifugal pump—were developed. These models enabled a precise characterisation of the energy conversion chain under variable solar irradiance and temperature conditions. The analysis confirmed the non-linear behavior of PV modules and the importance of implementing real-time control strategies, such as Maximum Power Point Tracking (MPPT), to ensure optimal energy transfer to the pumping unit.

Building upon these theoretical foundations, the implementation phase focused on two complementary test benches. The first system, based on a DC-DC boost converter controlled by an Arduino Mega using a fuzzy logic algorithm, successfully achieved dynamic power optimisation. This intelligent control technique improved response stability under fluctuating solar conditions while maintaining a low-cost and modular hardware architecture suitable for rural deployment.

The second test bench, centred on the HM310 hydrophilic platform, enabled experimental validation of an advanced smart irrigation system driven by an AC motor–pump set. The integration of sensor-based feedback and programmable control allowed for accurate regulation of hydraulic parameters, demonstrating the feasibility of autonomous irrigation management. The experimental results highlighted significant improvements in both energy utilisation and water-use efficiency, reinforcing the relevance of intelligent control in sustainable agriculture.

Overall, this thesis confirms that intelligent PV pumping systems can effectively couple renewable energy generation with modern irrigation technologies. By combining fuzzy logic control, efficient power conversion, and real-time monitoring, the proposed architectures con-

tribute to reducing energy costs, minimising water wastage, and enhancing system reliability.

Future research may focus on expanding these control strategies to hybrid renewable systems, integrating predictive algorithms based on meteorological forecasting, and exploring IoT-based remote management for large-scale agricultural applications. Such advancements will further support the transition toward sustainable, autonomous, and resource-efficient irrigation systems.

Future Perspectives

Building on the results obtained in this work, several research directions and practical developments can be envisaged:

- **Hybrid Renewable Integration:** Future systems could integrate photovoltaic energy with complementary renewable sources such as wind or biomass to ensure continuous pumping operation, particularly during low-irradiance periods.
- **Advanced Control and Prediction:** The application of predictive algorithms—based on artificial intelligence and machine learning—could enhance MPPT performance and irrigation scheduling by anticipating environmental variations and crop water requirements.
- **IoT and Remote Monitoring:** Incorporating Internet of Things (IoT) platforms will enable real-time supervision, data acquisition, and remote diagnostics, facilitating adaptive control and predictive maintenance in large-scale irrigation networks.
- **Optimisation of Power Electronics:** Further research into high-efficiency converters and soft-switching topologies could improve energy conversion and extend the operational lifetime of system components.
- **Field Deployment and Socioeconomic Evaluation:** Pilot implementations in agricultural sites under varying climatic and soil conditions should be conducted to assess long-term performance, maintenance needs, and the socioeconomic impact on rural communities.

In conclusion, the methodologies and technologies presented in this thesis lay a robust foundation for developing next-generation, autonomous, and resource-efficient photovoltaic

irrigation systems. Continued interdisciplinary efforts combining renewable energy engineering, control theory, and agricultural science will be essential to address future challenges in sustainable water and energy management.

References

[1] Saeed Mohammed Wazed, Ben Richard Hughes, Dominic O'Connor, and John Kaiser Calautit. A review of sustainable solar irrigation systems for sub-saharan africa. *Renewable and Sustainable Energy Reviews*, 81:1206–1225, 2018.

[2] Imran Ali Lakhiar, Haofang Yan, Chuan Zhang, Guoqing Wang, Bin He, Beibei Hao, Yujing Han, Biyu Wang, Rongxuan Bao, Tabinda Naz Syed, et al. A review of precision irrigation water-saving technology under changing climate for enhancing water use efficiency, crop yield, and environmental footprints. *Agriculture*, 14(7):1141, 2024.

[3] ML Louazene, MC Alonso Garcia, and D Korichi. Efficiency optimization of a photovoltaic water pumping system for irrigation in ouargla, algeria. In *AIP Conference Proceedings*, volume 1814, page 020039. AIP Publishing LLC, 2017.

[4] Nicole Lefore, Alvar Closas, and Petra Schmitter. Solar for all: A framework to deliver inclusive and environmentally sustainable solar irrigation for smallholder agriculture. *Energy Policy*, 154:112313, 2021.

[5] Laura García, Lorena Parra, Jose M Jimenez, Jaime Lloret, and Pascal Lorenz. Iot-based smart irrigation systems: An overview on the recent trends on sensors and iot systems for irrigation in precision agriculture. *Sensors*, 20(4):1042, 2020.

[6] Gerard Arbat and Daniele Masseroni. The use and management of agricultural irrigation systems and technologies, 2024.

[7] Pierre Dechamps. The iea world energy outlook 2022–a brief analysis and implications. *European Energy & Climate Journal*, 11(3):100–103, 2023.

[8] Piers M Forster, Chris Smith, Tristram Walsh, William F Lamb, Robin Lamboll, Bradley Hall, Mathias Hauser, Aurélien Ribes, Debbie Rosen, Nathan P Gillett, et al. Indicators of global climate change 2023: annual update of key indicators of the state of

the climate system and human influence. *Earth System Science Data*, 16(6):2625–2658, 2024.

[9] Michael Renner, Celia Garcia-Banos, Arslan Khalid, et al. Renewable energy and jobs: annual review 2022. *ILO: Abu Dhabi, United Arab Emirates*, 2022.

[10] Rabie Said, Muhammad Ishaq Bhatti, and Ahmed Imran Hunjra. Toward understanding renewable energy and sustainable development in developing and developed economies: a review. *Energies*, 15(15):5349, 2022.

[11] Tamás Mizik. Climate-smart agriculture on small-scale farms: A systematic literature review. *Agronomy*, 11(6):1096, 2021.

[12] John E Hay and Philip W Suckling. An assessment of the networks for measuring and modelling solar radiation in british columbia and adjacent areas of western canada. *Canadian Geographer/Le Géographe canadien*, 23(3):222–238, 1979.

[13] Bhim Singh, CL Putta Swamy, and BP Singh. Analysis and development of a low-cost permanent magnet brushless dc motor drive for pv-array fed water pumping system. *Solar Energy Materials and Solar Cells*, 51(1):55–67, 1998.

[14] Horacio G Vasquez. *Variable speed control of a switched reluctance motor in a heat pump application*. The University of Alabama, 2003.

[15] YT Chen, A Kribus, BH Lim, CS Lim, KK Chong, Jacob Karni, R Buck, A Pfahl, and TP Bligh. Comparison of two sun tracking methods in the application of a heliostat field. *J. Sol. Energy Eng.*, 126(1):638–644, 2004.

[16] Daniele Fiaschi, Roberto Graniglia, and Giampaolo Manfrida. Improving the effectiveness of solar pumping systems by using modular centrifugal pumps with variable rotational speed. *Solar energy*, 79(3):234–244, 2005.

[17] Adel A Ghoneim. Design optimization of photovoltaic powered water pumping systems. *Energy conversion and management*, 47(11-12):1449–1463, 2006.

[18] I Odeh, YG Yohanis, and Brian Norton. Influence of pumping head, insolation and pv array size on pv water pumping system performance. *Solar energy*, 80(1):51–64, 2006.

[19] Zvonimir Glasnovic and Jure Margeta. Optimization of irrigation with photovoltaic pumping system. *Water resources management*, 21(8):1277–1297, 2007.

[20] A Hamidat and B Benyoucef. Mathematic models of photovoltaic motor-pump systems. *Renewable Energy*, 33(5):933–942, 2008.

[21] Bulent Yesilata and Z Abidin Firatoglu. Effect of solar radiation correlations on system sizing: Pv pumping case. *Renewable Energy*, 33(1):155–161, 2008.

[22] M Abdolzadeh and M Ameri. Improving the effectiveness of a photovoltaic water pumping system by spraying water over the front of photovoltaic cells. *Renewable energy*, 34(1):91–96, 2009.

[23] Azadeh Kordzadeh. The effects of nominal power of array and system head on the operation of photovoltaic water pumping set with array surface covered by a film of water. *Renewable energy*, 35(5):1098–1102, 2010.

[24] J Zorrilla-Casanova, M Piliougine, J Carretero, P Bernaola, P Carpena, L Mora-López, and M Sidrach-de Cardona. Analysis of dust losses in photovoltaic modules. In *World renewable energy congress*, pages 2985–2992. Linköping University Electronic Press Linköping, Sweden, 2011.

[25] Azzedine Boutelhig, Yahia Bakelli, Idriss Hadj Mahammed, and Amar Hadj Arab. Performances study of different pv powered dc pump configurations for an optimum energy rating at different heads under the outdoor conditions of a desert area. *Energy*, 39:33–39, 2012.

[26] PD Narale, NS Rathore, S Kothari, and PV Bhosale. Design and economic analysis of a solar pv water pumping system for irrigation of banana. 2013.

[27] Robert Foster and Alma Cota. Solar water pumping advances and comparative economics. *Energy Procedia*, 57:1431–1436, 2014.

[28] Aamir Mehmood, Adeel Waqas, and Hafiza Tahira Mahmood. Economic viability of solar photovoltaic water pump for sustainable agriculture growth in pakistan. *Materials today: proceedings*, 2(10):5190–5195, 2015.

[29] Hussein A Kazem, Ali HA Al-Waeli, Miqdam T Chaichan, Asma S Al-Mamari, and Atma H Al-Kabi. Design, measurement and evaluation of photovoltaic pumping system for rural areas in oman. *Environment, Development and Sustainability*, 19:1041–1053, 2017.

[30] Rafael González Perea, Aida Mérida García, Irene Fernández García, Emilio Camacho Poyato, Pilar Montesinos, and Juan Antonio Rodríguez Díaz. Middleware to operate smart photovoltaic irrigation systems in real time. *Water*, 11(7):1508, 2019.

[31] V Zavala, R López-Luque, J Reca, J Martínez, and MT Lao. Optimal management of a multisector standalone direct pumping photovoltaic irrigation system. *Applied Energy*, 260:114261, 2020.

[32] Aziz Haffaf, Fatiha Lakdja, Djaffar Ould Abdeslam, and Rachid Meziane. Monitoring, measured and simulated performance analysis of a 2.4 kwp grid-connected pv system installed on the mulhouse campus, france. *Energy for Sustainable Development*, 62:44–55, 2021.

[33] Jiusheng Li. Increasing crop productivity in an eco-friendly manner by improving sprinkler and micro-irrigation design and management: a review of 20 years' research at the iwhr, china. *Irrigation and drainage*, 67(1):97–112, 2018.

[34] Dean E Eisenhauer, Derrel L Martin, Derek M Heeren, and Glenn J Hoffman. *Irrigation systems management*. American Society of Agricultural and Biological Engineers (ASABE), 2021.

[35] Yaohu Kang, Hai-Jun Liu, and Shi-Ping Liu. Effect of sprinkler irrigation on field microclimate. In *2002 ASAE Annual Meeting*, page 1. American Society of Agricultural and Biological Engineers, 2002.

[36] Tamara Communal, Nicolas Faysse, Sylvain Bleuze, and Byron Aceldo. Effects at farm and community level of the adoption of sprinkler irrigation in the ecuadorian andes. *Irrigation and Drainage*, 65(4):559–567, 2016.

[37] IPCC Climate Change. Land: an ipcc special report on climate change. *Desertification, land degradation, sustainable land management, food security, and greenhouse gas fluxes in terrestrial ecosystems*, 41, 2019.

[38] Luis Santos Pereira, Theib Oweis, and Abdelaziz Zairi. Irrigation management under water scarcity. *Agricultural water management*, 57(3):175–206, 2002.

[39] Robert G Evans and E John Sadler. Methods and technologies to improve efficiency of water use. *Water resources research*, 44(7), 2008.

[40] JC Durán-Álvarez, B Prado, D González, Y Sánchez, and B Jiménez-Cisneros. Environmental fate of naproxen, carbamazepine and triclosan in wastewater, surface water and wastewater irrigated soil—results of laboratory scale experiments. *Science of the Total Environment*, 538:350–362, 2015.

[41] Pierre-Louis Viollet. *Water engineering in ancient civilizations: 5,000 years of history*. CRC Press, 2007.

[42] moringchores. *hand-watering*. 2024. Last accessed 15 july 2024.

[43] Isaya V Sijali. *Drip irrigation: Options for smallholder farmers in Eastern and Southern Africa*. Number 24. Regional Land Management Unit, 2001.

[44] irrigationsuppliesstore. *Surfece irrigation*. 2024. Last accessed 15 july 2024.

[45] Wynn R Walker. Guidelines for designing and evaluating surface irrigation systems. 1989.

[46] turko.ge. *sprink irrigation*. 2024. Last accessed 16 july 2024.

[47] Robert G Evans, Jake LaRue, Kenneth C Stone, and Bradley A King. Adoption of site-specific variable rate sprinkler irrigation systems. *Irrigation science*, 31:871–887, 2013.

[48] housing.com. *Drip irrigation*. 2024. Last accessed 16 july 2024.

[49] Priyabrata Santra. Performance evaluation of solar pv pumping system for providing irrigation through micro-irrigation techniques using surface water resources in hot arid region of india. *Agricultural Water Management*, 245:106554, 2021.

[50] James E Ayars, Daniele Zaccaria, and Khaled M Bali. *Microirrigation for crop production: design, operation, and management*. Elsevier, 2023.

[51] twl irrigation. *Precice irrigation*. 2024. Last accessed 23 july 2024.

[52] Michael D Dukes, Lincoln Zotarelli, and Kelly T Morgan. Use of irrigation technologies for vegetable crops in florida. *HortTechnology*, 20(1):133–142, 2010.

[53] Dennis L Corwin. Climate change impacts on soil salinity in agricultural areas. *European Journal of Soil Science*, 72(2):842–862, 2021.

[54] Mahmud Ahmed Sasi. *Fuzzy logic control of MPPT controller for PV systems*. PhD thesis, Memorial University of Newfoundland, 2017.

[55] Tabish Anjum, Jeeban Kumar Nayak, and Arnab Ghosh. A comparative analysis between perturb & observe and incremental conductance techniques for mppt in pv system. In *2022 IEEE 10th Power India International Conference (PIICON)*, pages 1–6. IEEE, 2022.

[56] Martin A. Green, Ewan D. Dunlop, Dean H. Levi, Jochen Hohl-Ebinger, Masahiro Yoshita, and Anita W.Y. Ho-Baillie. Solar cell efficiency tables (version 54). *Progress in Photovoltaics: Research and Applications*, 27(7):565–575, 2019.

[57] S. Latreche, A. E. Badoud, and M. Khemliche. Implementation of mppt algorithm and supervision of shading on photovoltaic module. *Engineering, Technology & amp, Applied Science Research*, 8(6):3541–3544, December 2018.

[58] Martin A Green. Crystalline silicon solar cells. *Series on Photoconversion of Solar Energy*, pages 87–137, 2014.

[59] Oussama Belaroussi, Abdelkarim Ammar, and A Lechelah. Maximum power point tracking of solar water pumping systems using fuzzy logic algorithm. In *The 1st National Conference on Green Energy (NCGE'2023)*, pages 204–8, 2023.

[60] P. Acharya, M. N. Shaikh, S. K. Jha, and A. P. Papadakis. Electrical modelling of a photovoltaic module. December 2016.

[61] Muhammad Iqbal. *An introduction to solar radiation*. Elsevier, 2012.

[62] Jesus Polo, Stefan Wilbert, José A Ruiz-Arias, Richard Meyer, Christian Gueymard, Marcel Suri, Luis Martin, Theresa Mieslinger, Philippe Blanc, Ian Grant, et al. Preliminary survey on site-adaptation techniques for satellite-derived and reanalysis solar radiation datasets. *Solar Energy*, 132:25–37, 2016.

[63] John K Kaldellis, Marina Kapsali, and Kosmas A Kavadias. Temperature and wind speed impact on the efficiency of pv installations. experience obtained from outdoor measurements in greece. *Renewable energy*, 66:612–624, 2014.

[64] Mohamed Essalih Boussouar. *Speed Sensorless Control of Synchronous Reluctance Motor*. PhD thesis, Faculté des sciences et technologie, 2024.

[65] Davood GHADERİ. Design and implementation of a step-up power converter for renewable resource application. *Sakarya University Journal of Science*, 24(1):86–97, February 2020.

[66] Bimal K Bose. Power electronics and ac drives. *Englewood Cliffs*, 1986.

[67] MH Rashid and Philip T Krein. 'power electronics: Circuits, devices and applications', pearson education, phi third edition, new delhi 2004., 2015.

[68] Jose Rodriguez, Marian P Kazmierkowski, Jose R Espinoza, Pericle Zanchetta, Haitham Abu-Rub, Hector A Young, and Christian A Rojas. State of the art of finite control set model predictive control in power electronics. *IEEE Transactions on Industrial Informatics*, 9(2):1003–1016, 2012.

[69] Andrea Vacca and Germano Franzoni. *Hydraulic fluid power: Fundamentals, applications, and circuit design.* John Wiley & Sons, 2021.

[70] Hatem Fahd Frayyeh, Muayad A. Mukhlif, Abdulsalam M. Abbood, and Settar S. Keream. Speed control of direct current motor using mechanical characteristics. *Journal of Southwest Jiaotong University*, 54(4), 2019.

[71] Noah D Manring and Roger C Fales. *Hydraulic control systems.* John Wiley & Sons, 2019.

[72] Stephen J Chapman. *Electric machinery fundamentals*, volume 5. McGraw-Hill Education, 2003.

[73] Mohamed Adel Esmaeel Salama, Nada Mohamed El-Naggar, and Salama Abu-Zaid. Energy saving analysis for pump-motor set in water purification plant using variable speed drive. *Scientific Reports*, 14(1):27728, 2024.

[74] Mukhtar Ahmad. Modeling of induction and synchronous machines. pages 13–45, 2010.

[75] Andrzej M Trzynadlowski. *Control of induction motors.* Elsevier, 2000.

[76] Jacek F Gieras. *Permanent magnet motor technology: design and applications.* CRC press, 2009.

[77] Ivor R. Smith, Gerald K. Creighton, and Mustafa O. Kaynak. Theoretical and experimental study of an asynchronized synchronous machine. *IEEE Transactions on Industrial Electronics and Control Instrumentation*, IECI-22(4):501–506, November 1975.

[78] Stephen J Chapman. Electric machinery fundamentals, 2004.

[79] Mikael Stocks. *Modeling, analysis, state and parameter estimation of faulty induction machines*. PhD thesis, Luleå tekniska universitet, 2006.

[80] X.Z. Liu, G.C. Verghese, J.H. Lang, and M.K. Onder. Generalizing the blondel-park transformation of electrical machines: necessary and sufficient conditions. *IEEE Transactions on Circuits and Systems*, 36(8):1058–1067, 1989.

[81] Diego Bellan. Clarke transformation solution of asymmetrical transients in three-phase circuits. *Energies*, 13(19):5231, 2020.

[82] Donald W Novotny and Thomas A Lipo. *Vector control and dynamics of AC drives*, volume 41. Oxford university press, 1996.

[83] Yong-le Ai. *Novel direct field and torque control of six-phase induction machine with special phase current waveform*. PhD thesis, Stellenbosch: University of Stellenbosch, 2006.

[84] Kwang-Mook Lim and Sung-Ill Lee. A study on the effects of rotation rate and flow rate on the operating characteristics in centrifugal pump. *Fire science and engineering*, 33(3):56–62, June 2019.

[85] E Shashi Menon. *Working Guide to Pump and Pumping Stations: Calculations and Simulations*. Gulf Professional Publishing, 2009.

[86] John Tuzson. *Centrifugal pump design*. John Wiley & Sons, 2000.

[87] Sulzer Pumps. *Sulzer centrifugal pump handbook*. Elsevier, 1997.

[88] Horst Marschner. *Marschner's mineral nutrition of higher plants*. Academic press, 2012.

[89] Martin Huldrych Zimmermann. *Xylem structure and the ascent of sap*. Springer Science & Business Media, 2013.

[90] Lincoln Taiz, Eduardo Zeiger, Ian M Møller, and Angus Murphy. Plant physiology and development. 2015.

[91] Park S Nobel. *Physicochemical & environmental plant physiology*. Academic press, 1999.

[92] Daniel Hillel. *Introduction to environmental soil physics*. Elsevier, 2003.

[93] Hamlyn G Jones. *Plants and microclimate: a quantitative approach to environmental plant physiology*. Cambridge university press, 2014.

[94] Christian Körner. The forest's nutrient cycle drives its carbon cycle. *Tree Physiology*, 42(3):425–427, 2022.

[95] Hans Lambers, F Stuart Chapin III, and Thijs L Pons. *Plant physiological ecology*. Springer Science & Business Media, 2008.

[96] P.S. Nobel. *Physicochemical and Environmental Plant Physiology*. Academic Press, 2009.

[97] HD Barrs and TT Kozlowski. Water deficits and plant growth. *Determination of Water Deficits in Plant Tissue, 1st ed.; Kozlowski, TT, Ed*, pages 235–368, 1968.

[98] Malin Falkenmark and Johan Rockström. *Balancing water for humans and nature: the new approach in ecohydrology*. Earthscan, 2004.

[99] Terry A Howell. Irrigation efficiency. *Encyclopedia of water science*, 467:500, 2003.

[100] JM Suttie, SG Reynolds, and C Batello. Grasslands of the world: Fao. *Rome, Italy*, 2005.

[101] G Philip Robertson and Peter M Vitousek. Nitrogen in agriculture: balancing the cost of an essential resource. *Annual review of environment and resources*, 34(1):97–125, 2009.

[102] Ali Hussein Numan, Zahraa Salman Dawood, and Hashim A Hussein. Theoretical and experimental analysis of photovoltaic module characteristics under different partial shading conditions. *International Journal of Power Electronics and Drive Systems*, 11(3):1508, 2020.

[103] F Satybaldiyeva, R Beisembekova, A Saribayev, GZ Yessenbekova, and A Kultas. Development of models of the maximum power of the solar energy tracking system based on a photopanel. *Journal of Theoretical and Applied Information Technology*, 99(6):1402–1413, 2021.

[104] Oday A Ahmad, Hussain Sayed, Kanaan A Jalal, Dhari Y Mahmood, and Waleed H Habeeb. Design and implementation of an indoor solar emulator based low-cost autonomous data logger for pv system monitoring. *International Journal of Power Electronics and Drive Systems (IJPEDS)*, 10(3):1645–1654, 2019.

[105] Muhammad Lutfi. Datasheet arduino mega 2560. *Didapat dari: eprints. polsri. ac. id*, 2017.

[106] M Kaczmarek, A Szczesny, and R Nowicz. The study of electronic voltage transducers operation in conditions of dips and interruptions of measured voltage. *Bulletin of the Polish Academy of Sciences. Technical Sciences*, 60(3):645–649, 2012.

[107] Muhammad Hafeez Mohamed Hariri, Mohd Khairunaz Mat Desa, Syafrudin Masri, and Muhammad Ammirrul Atiqi Mohd Zainuri. Design and implementation of three-phase voltage and current transducers for digital signal processing tms320f28335. *Journal of Electrical Systems*, 17(1), 2021.

Appendix A

A.1 Power pack sizing

The DC/DC converter in the power block, which is built around a PUB314 IGBT, makes sure that all of the energy taken out of the solar panel is sent to a resistive load. The limitations set by the requirements determine the size of this power block.

A.1.1 Charge sheet

The charge sheet that we are supposed to have is as follows:

- Current fluctuation in the inductanceΔiL: = 0.045 A.
- Tension at the capacitor C1 and C2 is bearings: ΔVC1=ΔVC2= 0.055 V.
- Commutation frequency: f = 1 KHz.

A.1.2 Determination of the values of L, C1 and C2

$$L \geq \frac{Vpv}{4.\Delta iLmax.f} = \frac{17.5}{4.0.045.10^3} \simeq 0.0972mH \tag{A.1}$$

In practice, the inductor used is with an iron core, which has a value of L=0.1 H.

To meet the condition on the ripple of the output voltage, the capacity of the capacitor C1 and C2 must verify the expression:

$$L \geq \frac{\Delta iL}{4.\Delta VCmax.f} = \frac{0.045}{4.0.055.10^3} \simeq 204.5uf \tag{A.2}$$

The hardware capacitors C1 and C2 implemented has a value of C = 220 uf

A.2 SAER elettropompe BP 6 C data sheet

SAER®

ELETTROPOMPE



BP14

BP8

ELETTROPOMPE CENTRIFUGHE MONOGIRANTI

SINGLE STAGE ELECTRIC CENTRIFUGAL PUMPS

ELECTROBOMBAS CENTRIFUGAS CON UNA TURBINA

ELECTROPOMPES CENTRIFUGES MONOTURBINES

EINSTUFIGE ELEKTRO-KREISELPUMPEN

EECTROBOMBAS CENTRÍFUGAS DE UM IMPULSORL

BP

3-4-5-6-7-8
9-10-11-12-13-14-15-16-17

2900 1/min

Tipo Type Typ	Motore Motor - Moteur		U.S.g.p.m.	0	13	26	40	53	66	79	92	106	119	132	159	185	211	238	264	291	317	343	370	396	440	528	616	726	792	924
			m^3/h	0	3	6	9	12	15	18	21	24	27	30	36	42	48	54	60	66	72	78	84	90	100	120	140	165	180	210
	kW	HP	l/min	0	50	100	150	200	250	300	350	400	450	500	600	700	800	900	1000	1100	1200	1300	1400	1500	1667	2000	2333	2750	3000	3500
BP 3	0,75	1	H (m)	21,5	20,6	19,5	18,5	17,3	16	14	11,8	9																		
BP 4	1,1	1,5		22			21,4	20,6	20	19	17,5	15,5	13,6	11,5																
BP 5	1,5	2		24				23,5	23	22	22	19,5	17,6	15	9															
BP 6E	0,59	0,8	H (m)	15	14,8	14,6	13,6	12,3	10,7	8,4	5,4																			
BP 6D	0,9	1,2		20,2	20	19,5	18,6	17,4	15,6	13,7	10,7																			
BP 6C	0,59	0,8		12,3		12,6	11,9	11,5	10,8	9,8	8,6	7,1	5,4																	
BP 6B	0,75	1		14,5		14,4	14,3	14	13,5	12,7	11,7	10,5	9	7,2																
BP 6A	0,9	1,2		16				15,9	15,5	14,8	14	12,9	11,5	10,1																
BP 7D	1,1	1,5		12,7			12,6	12,5	12,3	12,1	12	11,7	11,4	11	9,6	8,3	6,7	5	2,9										
BP 7C	1,5	2		15,9				15,7	15,5	15,3	15,2	14,8	14,6	14,1	12,8	11,5	10	8,2	6,1										
BP 7B	2,2	3		19,4				19,2	19	18,8	18,7	18,4	18	17,6	17,2	15	13,4	11,7	9,6										
BP 7A	3	4		22,4				22,2	22	21,8	21,7	21,4	21	20,8	19,6	18	16,4	14,7	12,6	10,3									
BP 8C	3	4		16,5											16,4	16,2	15,8	15,3	14,7	14	13,2	12,3	11,4	10,3	8				
BP 8B	4	5,5		18,5											18,4	18,2	17,8	17,3	16,7	16	15,2	14,3	13,4	12,3	10				
BP 8A	5,5	7,5		20,5											24,4	20,2	19,8	19,3	18,7	18	17,2	16,3	15,4	14,3	12	7			
BP 9C	1,5	2	H (m)	28		27	26	24,8	23	20,7																				
BP 9B	2,2	3		33,4		32,2	31,5	29,7	28	25,8																				
BP 9A	3	4		37		36	35	33,8	32	30,1																				
BP 10NC	4	5,5		44,5		43	42,5	41,6	41	39,6	37,5	33																		
BP 10NB	5,5	7,5		53,6		53	52,5	51,7	51,4	49,8	48	45	42,5	35																
BP 10NA	7,5	10		63		62,8	62,6	62,3	62	60,6	60,1	58,5	56	49,7																
BP 11NC	3	4	H (m)	31,5				30,6	30,4	30,2	29	28,5	28	27,5	26	22,5	19													
BP 11NB	4	5,5		35,5				35	34,8	34,3	33,8	33	32,5	31,7	30	27,5	25	21	16											
BP 11NA	5,5	7,5		38,6				38	37,8	37,5	37	36,5	36	35,5	33,5	32	29	26	22										
BP 12C	4	5,5		45				43,9	43	42,2	40	38	36	33,5																
BP 12B	5,5	7,5		47,5				47,4	47,1	46,9	45	43	42	39,9	35															
BP 12A	7,5	10		57,5				56,9	56,5	56	54,5	53	52	50	45	37	22,5													
BP 13B	5,5	7,5	H (m)	31,5									30,5	30,1	29	27,5	25,5	23	20	17,7										
BP 13A	7,5	10		39,4									38,6	38,4	38	37	35	33	30,5	28,5										
BP 14C	9	12,5		51,2									48,6	48,2	42	45	42,5	39,5	36,5	32,5										
BP 14B	11	15		57,5									55	54,2	53	51	48	45,5	42,5	38,5	33									
BP 14A	15	20		61									59	58,2	57,6	57	55	56,5	47	48	45,5	42,5	38,5	35,5						
BP 15C	9	12,5	H (m)	31,8										31,3	31	30,5	30	29,5	29,1	28	27,5	27	25,5	24,2	22,1					
BP 15B	11	15		39,3										38,8	38,5	38,3	38	37,5	37	36,5	36	35,5	34,5	33,5	31,6					
BP 15A	15	20		41,5										41,5	41,2	41	40,8	40,5	40,2	39,5	39	38,5	37,5	36,7	34,7	28,6				
BP 16C	15	20		41													40	39,5	39	38	37,5	36,5	35	33,9	31					
BP 16B	18,5	25		48													47,7	47,5	47	46,5	46	45,5	44,5	42,8	40	33				
BP 16A	22	30		54													55,1	55	54,9	54,7	54,5	54	53	51,5	49,5	44,2				
BP 17G	5,5	7,5	H (m)	19,2															18	17,8	17,5	17	16,5	15,5	14	12	9			
BP 17F	7,5	10		20,2															20	19,8	19,5	19	18	18	17	15	12,7			
BP 17E	9	12,5		23,6															23	22,8	22,5	22	21	20,3	19,5	17,5	14,8			
BP 17D	11	15		26,5															25	24,9	24,8	24,5	24	23,2	22,5	20,5	17,8			
BP 17C	15	20		32,5															32	31,5	31	30,5	30	29,5	28,5	26,5	24	20	17,6	
BP 17B	18,5	25		37,5															37	36,5	36	35,5	35	34,5	33,6	32,6	29,5	26,4	24,1	
BP 17A	22	30		40,3															39,9	39,7	39,5	39	38,7	38,4	38	37,2	34,9	31,8	29,5	24,5

ELETTROPOMPE CENTRIFUGHE MONOGIRANTI

ELECTRIC SINGLE IMPELLER CENTRIFUGAL PUMPS
ELECTROBOMBAS CENTRIFUGAS CON UNA TURBINA
ELECTROPOMPES CENTRIFUGES MONOTURBINES
EINSTUFIGE ELEKTRO-KREISELPUMPEN
EECTROBOMBAS CENTRÍFUGAS DE UM IMPULSORL

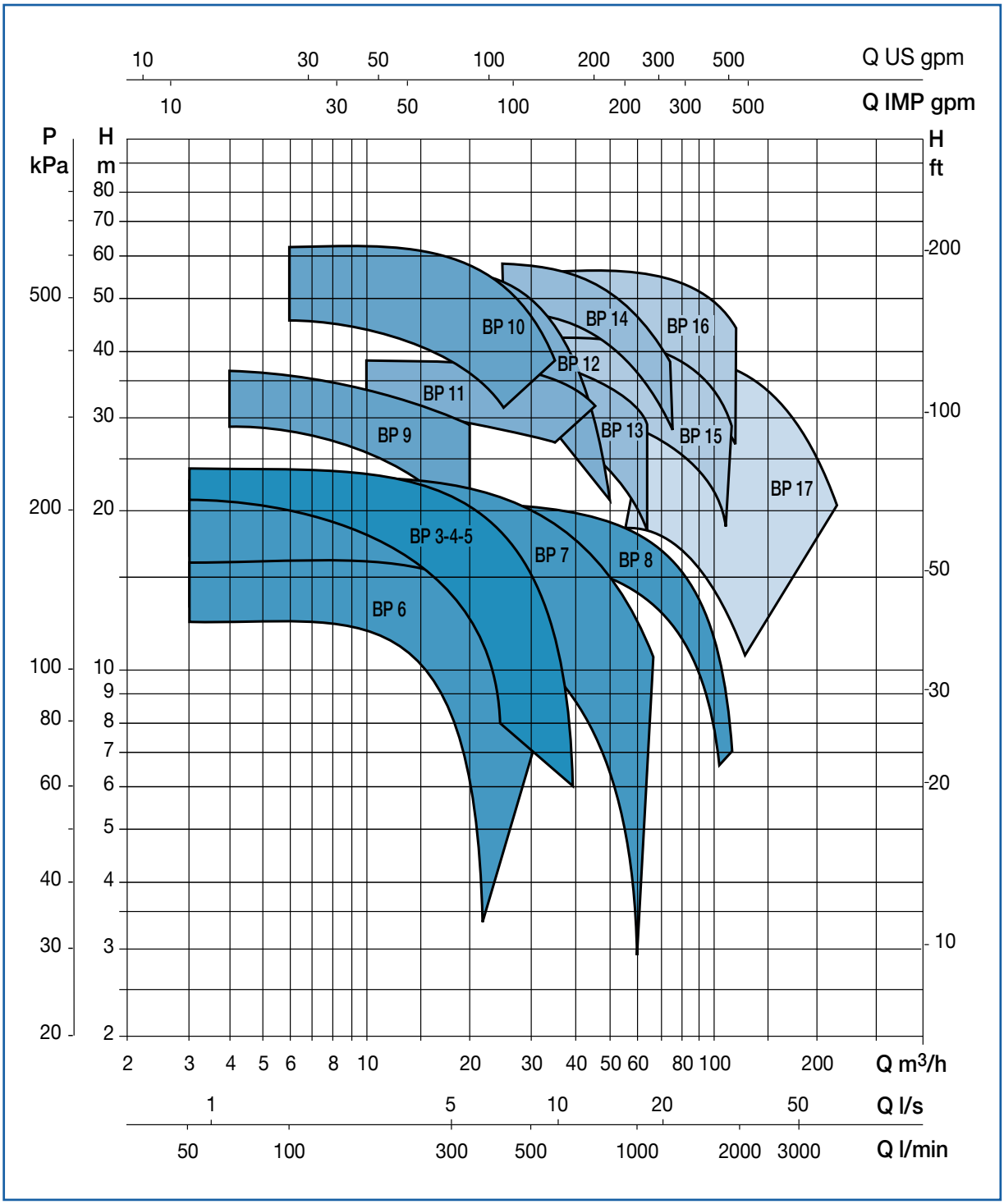

BP

3-4-5-6-7-8
9-10-11-12-13-14-15-16-17



BP8

ITALIANO

PRINCIPIO DI FUNZIONAMENTO
Questa serie di elettropompe centrifughe monogiranti è stata progettata per ottenere prevalenze medio basse e portate elevate in rapporto alle prevalenze.

IMPIEGHI
Queste elettropompe trovano impiego in impianti di irrigazione a scorrimento e a pioggia, nel prelievo di acqua da laghi, fiumi, vasche e per altri svariati utilizzi industriali dove vi sia la necessità di portate elevate e prevalenze medio basse.

CARATTERISTICHE COSTRUTTIVE
Corpo pompa, supporto motore in ghisa. Girante in ghisa (BP 6D-6E-7-8-9A-13-14-15-16-17) in ottone stampato (BP 3-4-5-6A-6B-6C-9B-9C-10-11-12).
Tenuta meccanica in grafite/ceramica, motore elettrico del tipo chiuso a ventilazione esterna, rotore montato su cuscinetti a sfere prelubrificati a vita. A richiesta è possibile fornire l'elettropompa con una protezione termoamperometrica incorporata, mentre il condensatore è permanentemente inserito nella versione monofase.
Grado di protezione del motore:
IP 44 BP 3-4-5-6-7, a richiesta IP 55.
IP 55 BP 9-10-11-12-13-14-15-16-17
Classe di isolamento: F
Tensione di serie: monofase 230V- 50Hz
trifase 230/400V-50Hz fino 5,5 HP
oltre 400/690-50Hz
Esecuzioni speciali a richiesta.

DATI CARATTERISTICI
- Portate fino a 220 m3/h
- Prevalenze fino a 55 m
- Temperatura liquido pompato:
  da -15° C a +70° C per BP 3-4-5-6
  da -15° C a +120° C per BP 7-8-9-13-14-15-16-17
- Pressione massima di esercizio:
  6 bar per BP 3-4-5-6
  10 bar per BP 7-8-9-13-14-15-16-17
- Temperatura massima ambiente: 40° C (per temperature superiori rivolgersi al nostro servizio tecnico).

Le caratteristiche di funzionamento e di catalogo si intendono per servizio continuo ed acqua pulita (peso specifico 1000 kg/m³) con altezza monometrica massima di aspirazione di 1,5 m.c.a.
Per altezze monometriche superiori e fino ad un massimo di 6-7 m.c.a. le caratteristiche si riducono nei valori di portata.
La tubazione di aspirante deve essere assolutamente stagna e per i dati di catalogo deve avere i seguenti diametri minimi

DN (aspirazione pompa)	DN (tubo aspirante)
2”	Ø80
2 ”	Ø100
3”	Ø150
4”	Ø200

Prestazioni idrauliche secondo ISO 9906 appendice A.
Motore elettrico secondo CEI EN 60034-1

INSTALLAZIONE
Le elettropompe serie BP possono essere installate con l'albero motore sia in posizione orizzontale che verticale. Qualora l'installazione fosse verticale il motore dovrà essere posizionato sempre sopra il corpo pompa.

ENGLISH

OPERATING PRINCIPLE
This series of single-impeller electric pumps has been designed for medium-to-low heads and elevated capacities in relation to the heads.

APPLICATIONS
These electric pumps can be used for surface-flooding and spray irrigation systems, lifting water from lakes, rivers and tanks, and for various industrial applications requiring elevated capacities and medium-to-low heads.

PUMP CONSTRUCTION
Pump body and motor support in cast iron. Impeller in cast iron (BP 6D-6E-7-8-9A-13-14-15-16-17) or in pressed brass (BP 3-4-5-6A-6B-6C-9B-9C-10-11-12).
Mechanical seal in graphite/ceramic, totally enclosed motor with external ventilation, rotor mounted on maintenance-free ball bearings.
The pumps can be supplied with a built-in thermal overload protection on request. The capacitor is permanently in circuit in the single-phase version.
Motor protected to: IP 44 BP 3-4-5-6-7, IP 55 on request.
IP 55 BP 9-10-11-12-13-14-15-16-17
Insulation class F
Standard voltage: single-phase 230V- 50Hz
Three-phase 230/400V- 50Hz up to 5.5HP
400/690-50Hz over 5.5HP
Special versions available on request.

PUMP PERFORMANCE DATA
- Capacities up to 220m³/h
- Heads up to 55m
- Temperature of pumped liquid:
  -15°C to +70°C for BP 3-4-5-6
  -15°C to +120°C for BP 7-8-9-13-14-15-16-17
- Max. working pressure: 6 bar for BP 3-4-5-6
  10 bar for BP 7-8-9-13-14-15-16-17
- Maximum ambient temperature: 40°C (for higher temperatures please contact our technical department).

The performance data shown in the catalogue are based on continuous service for clear water (specific weight 1000 kg/m³) with a maximum manometric suction lift of 1.5m w.c.
For higher manometric lifts, up to a maximum of di 6-7m w.c., pump capacities are reduced.
The suction pipe must be perfectly airtight and, to ensure the performance date shown in the catalogue, it must have the following minimum diameters

DN (pump suction)	DN (suction pipe)
2”	Ø80
2 ”	Ø100
3”	Ø150
4”	Ø200

Hydraulic performance according to ISO 9906 annex A.
Motor specifications according to CEI EN 60034-1

INSTALLATION
The series BP electric pumps can be installed with the motor shaft mounted either horizontally or vertically.
In the event of vertical installations, the motor must always be positioned above the pump body.

ESPAÑOL

PRINCIPIO DE FUNCIONAMIENTO
Esta serie de electrobombas centrífugas con una turbina se utiliza para obtener alturas de elevación medio/bajas y caudales altos en proporción a la altura de elevación.

APLICACIONES
Estas electrobombas se utilizan en sistemas de riego por inundación y por aspersión, para extraer agua de lagos, ríos, depósitos y para diferentes aplicaciones industriales donde se necesitan caudales altos y alturas de elevación medio/bajas.

CARACTERÍSTICAS DE CONSTRUCCIÓN
Cuerpo de la bomba y soporte del motor en fundición gris. Impulsor en fundición gris en los modelos BP 6D-6E-7-8-9A-13-14-15-16-17, impulsor en latón estampado en los modelos BP 3-4-5-6A-6B-6C-9B-9C-10-11-12.
Cierre mecánico en grafito/cerámica, motor eléctrico de construcción cerrada con ventilación exterior, rotor montado sobre rodamientos de bolas prelubricadas. Bajo pedido se suministra la electrobomba con una protección térmico-amperimétrica incorporada, suministrándose el condensador montado en la versión monofásica.
Grado de protección del motor:
IP 44 BP 3-4-5-6-7, bajo pedido IP 55.
IP 55 BP 9-10-11-12-13-14-15-16-17
Aislamiento: clase F
Tensión estándar: monofásica 230V-50 Hz
trifásica 230V/400V-50 Hz
400/690 50Hz superior 5.5HP
Bajo demanda se suministran versiones especiales.

DATOS CARACTERÍSTICOS
- Caudal hasta 220 m³/h
- Altura de elevación hasta 55 m
- Temperatura del líquido bombeado:
  de-15° C a +70° C para BP 3-4-5-6
  de -15° C a +120° C para BP 7-8-9-13-14-15-16-17
- Presión máxima de funcionamiento: 6 bares para BP 3-4-5-6
- Temperatura ambiente máxima: +40° C (para valores superiores consulte a nuestro servicio técnico).

Las características de funcionamiento y del catálogo se refieren a un uso continuo y con agua limpia (peso específico = 1000 kg/m³). Altura manométrica máxima de aspiración 1,5 m.c.a. Para alturas manométricas superiores y hasta un máximo de 6-7 m.c.a. las características se reducen en los valores de caudal. La tubería de aspiración debe ser completamente hermética y para los datos del catálogo debe tener los siguientes diámetros mínimos:

DN (aspiración bomba)	DN (tubo aspirante)
2”	Ø80
2”	Ø100
3”	Ø150
4”	Ø200

Prestaciones hidráulicas según ISO 9906, Anexo A. Motor eléctrico según CEI EN 60034-1.

INSTALACIÓN
Las electrobombas serie BP pueden montarse con el eje motor en posición horizontal o vertical.
En el caso de instalación en posición vertical, el motor siempre deberá situarse sobre el cuerpo de la bomba.

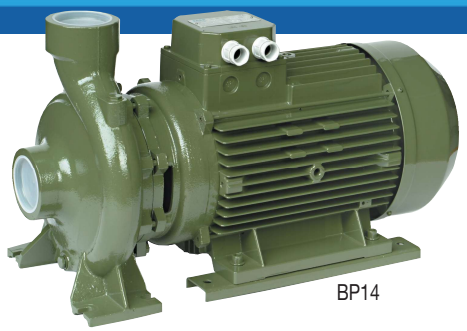
BP14

ELETTROPOMPE CENTRIFUGHE MONOGIRANTI

ELECTRIC SINGLE IMPELLER CENTRIFUGAL PUMPS
ELECTROBOMBAS CENTRIFUGAS CON UNA TURBINA
ELECTROPOMPES CENTRIFUGES MONOTURBINES
EINSTUFIGE ELEKTRO-KREISELPUMPEN
EECTROBOMBAS CENTRÍFUGAS DE UM IMPULSORL

FRANÇAIS

PRINCIPE DE FONCTIONNEMENT
Cette série d'électropompes centrifuges monoturbines a été étudiée pour obtenir des hauteurs d'élévation moyennes-basses et des débits élevés par rapport aux hauteurs d'élévation.

APPLICATIONS
Ces électropompes sont indiquées pour les installations d'arrosage par écoulement et par aspersion, pour le puisage d'eau dans des lacs, fleuves ou cuves et pour toutes les applications industrielles qui exigent des débits élevés avec des hauteurs d'élévation moyennes-basses.

CARACTÉRISTIQUES DE CONSTRUCTION
Corps de pompe et support moteur en fonte. Turbine en fonte (BP 6D-6E-7-8-9A-13-14-15-16-17) en laiton estampé (BP 3-4-5-6A-6B-6C-9B-9C-10-11-12). Garniture mécanique en graphite/céramique, moteur électrique en exécution fermée à ventilation extérieure, rotor monté sur roulements à billes prégraissés à vie. Sur demande, l'électropompe peut être équipée d'une protection thermo-ampèremétrique incorporée, tandis que le condensateur est incorporé en permanence dans la version monophasée.
Protection du moteur: IP 44 BP 3-4-5-6-7, sur demande IP 55.
IP 55 BP 9-10-11-12-13-14-15-16-17
Classe d'isolation: F
Tension de série: monophasée 230 V- 50 Hz
triphasée 230/400 V- 50 Hz jusqu'à 5,5 HP
au-delà de 400/690-50 Hz.
Exécutions spéciales sur demande.

CARACTÉRISTIQUES TECHNIQUES
- Débits jusqu'à 220 m³/h
- Hauteurs d'élévation jusqu'à 55 m
- Température du liquide pompé :
  de -15° C à +70° C pour BP 3-4-5-6
  de -15° C à +120° C pour BP 7-8-9-13-14-15-16-17
- Pression max. de service: 6 bars pour BP 3-4-5-6
  10 bars pour BP 7-8-9-13-14-15-16-17
- Température ambiante maximum : 40° C (pour des températures supérieures, consulter notre service technique).

Les caractéristiques de fonctionnement et de catalogue concernent le service continu avec eau claire (poids spécifique 1000 kg/m³) et une hauteur manométrique d'aspiration maximum d'1,5 m.c.e. Pour des hauteurs manométriques supérieures et jusqu'à un maximum de 6-7 m.c.e., les performances de la pompe diminuent en ce qui concerne les valeurs de débit.
Le tuyau d'aspiration doit être absolument étanche et pour obtenir les performances indiquées dans le catalogue, il doit avoir les diamètres minimums indiqués ci-après :

DN (orifice d'aspiration pompe)	DN (tuyau d'aspiration)
2"	Ø80
2 "	Ø100
3"	Ø150
4"	Ø200

Performances hydrauliques conformes aux normes ISO 9906 appendice A. Moteur électrique conforme aux normes CEI EN 60034-1

INSTALLATION
Les électropompes série BP peuvent être installées avec l'arbre moteur soit en position horizontale, soit en position verticale. En cas d'installation verticale, le moteur doit toujours être placé au-dessus du corps de pompe.

DEUTSCH

FUNKTIONSPRINZIP
Diese Elektro-Kreiselpumpen mit einem Läufer wurden für niedrige bis mittlere Förderhöhen und hohe Förderleistungen im Vergleich zu den Förderhöhen entwickelt.

EINSATZ
Diese Elektropumpen werden an Berieselungs- und Beregnungsanlagen, zur Wasserförderung aus Seen, Flüssen, Becken und an den unterschiedlichsten Industrieanlagen eingesetzt, wo hohe Förderleistungen und niedrige bis mittlere Förderhöhen notwendig sind.

KONSTRUKTIONSMERKMALE
Pumpengehäuse und Motorlager aus Guss.
Laufrad aus Guss (BP 6D-6E-7-8-9A-13-14-15-16-17) oder aus gepresstem Messing (BP 3-4-5-6A-6B-6C-9B-9C-10-11-12).
Gleitringdichtung aus Graphit/Keramik,
Geschlossener E-Motor mit Außenbelüftung, Rotor auf dauergeschmierten Kugellagern.
Auf Anfrage kann die Elektropumpe mit eingebautem Spannungs- und Wärmeschutzschalter geliefert werden, wogegen der Kondensator bei der einphasigen Ausführung bleibend eingeschaltet ist.
Motor-Schutzart: IP 44 für BP 3-4-5-6-7, auf Anfrage IP 55.
IP 55 für BP 9-10-11-12-13-14-15-16-17.
Isolationsklasse: F
Serienmäßige Spannung: einphasig 230V-50Hz
dreiphasig 230V/400V-50Hz bis 5,5 HP
darüber 400/690-50 Hz.
Auf Anfrage stehen Sonderausführungen zur Verfügung.

TECHNISCHE MERKMALE
- Förderleistungen bis 220 m³/h
- Förderhöhen bis 55 m
- Temperatur der gepumpten Flüssigkeit:
  von -15°C bis +70°C für BP 3-4-5-6
  von 15°C bis 120°C für BP 7-8-9-13-14-15-16-17
- max. Betriebsdruck: 6 bar für BP 3-4-5-6
  10 bar für BP 7-8-9-13-14-15-16-17
- max. Umgebungstemperatur 40°C (bei höherer Temperatur bitten wir um Rückfrage)

Die im Katalog angegebenen Betriebseigenschaften gelten für Dauerbetrieb mit sauberem Wasser (Dichte: 1000 Kg/m³), mit max. Saughöhe von 1,5m W.S..
Bei Saughöhen bis und über maximal 6-7 m W.S. reduziert sich die Förderleistung. Die Saugleitung muss vollkommen dicht sein; damit die angegebenen Daten erreicht werden, muss sie folgenden Mindestdurchmesser haben:

DN (Saugseite Pumpe)	DN (Saugrohr)
2"	Ø80
2 "	Ø100
3"	Ø150
4"	Ø200

Hydraulische Leistungen gemäß ISO 9906, Nachtrag A.
E-Motor gemäß CEI EN 60034-1.

INSTALLATION
Die Elektropumpen BP können mit der Motorwelle in horizontaler sowie vertikaler Stellung installiert werden.
Bei vertikaler Installation muss der Motor immer über dem Pumpenkörper angebracht werden.

PORTOGUÊS

PRINCÍPIO DE FUNCIONAMENTO
Esta série de electrobombas centrífugas de um só impulsor foi projectada para obter alturas manométricas médio-baixas e caudais elevados relativamente às alturas manométricas.

UTILIZAÇÕES
Estas electrobombas são utilizadas em sistemas de irrigação por escorrimento e aspersão, na recolha de água de lagos, rios, tanques e em diversas outras utilizações industriais onde são necessários caudais elevados e alturas manométricas médio-baixas.

CARACTERÍSTICAS DE CONSTRUÇÃO
Corpo da bomba, suporte do motor em ferro fundido. Impulsor em ferro fundido (BP 6D-6E-7-8-9A-13-14-15-16-17) em latão estampado (BP 3-4-5-6A-6B-6C-9B-9C-10-11-12).
Vedação mecânica em grafite/cerâmica, motor eléctrico tipo fechado com ventilação externa, rotor montado sobre mancais de esferas com lubrificação permanente.
Sob pedido, é possível fornecer a electrobomba com uma protecção termoamperométrica incorporada, enquanto o condensador é permanentemente inserido na versão monofásico.
Grau de protecção do motor: IP 44 até 1HP, sob pedido IP 55.
IP 55 de 1,5 HP e superiores
Classe de isolamento: F
Voltagem de série: monofásica 230V- 50Hz
trifásica 230/400V- 50Hz até 5,5 HP
superior 400/690-50Hz
Tipos especiais sob pedido.

CARACTERÍSTICAS
- Caudais até a 220 m³/h
- Alturas manométricas até a 55 m
- Temperatura líquido bombeado:
  de -15° C a +70° C para BP 3-4-5-6
  de -15° C a +120° C para BP 7-8-9-13-14-15-16-17
- Pressão máxima de funcionamento: 6 bar para BP 3-4-5-6
  10 bar para BP 7-8-9-13-14-15-16-17
- Temperatura máxima ambiente: 40° C (para temperaturas superiores, recorra ao nosso serviço técnico).

As características de funcionamento e de catálogo entendem-se para serviço contínuo e água limpa (peso específico 1000 kg/m³) com altura monométrica máxima de aspiração de 1,5 m.c.a.
Para alturas manométricas superiores e até a um máximo de 6-7 m.c.a., os valores de caudal reduzem-se.
A tubagem aspirante deve ser absolutamente estanque e para as características de catálogo deve ter os seguintes diâmetros mínimos:

DN (aspiração da bomba)	DN tubo aspirante)
2"	Ø80
2"	Ø100
3"	Ø150
4"	Ø200

Desempenho hidráulico segundo ISO 9906 apêndice A.
Motor eléctrico segundo CEI EN 60034-1

INSTALAÇÃO
As electrobombas da série BP podem ser instaladas com o veio do motor seja na posição horizontal, seja vertical.
Se a instalação for vertical, o motor deverá ser posicionado sempre sobre o corpo da bomba.

BP
3-4-5

≅ 2850 1/min

CARATTERISTICHE IDRAULICHE

HYDRAULIC FEATURES - CARACTERISTICAS HIDRAULICAS - CARACTERISTIQUES HYDRAULIQUES
HYDRAULISCHE EINGESCHAFTEN - CARACTERÍSTICAS HIDRÁULICAS

Tipo Type Typ	Alimentazione Feeding - Alimentacion Alimentation - Speisung Alimentação 50 Hz	P1 Max	P2 Nominale Nominal		Corrente assorbita Absorbed current Corriente absorbida Courant absorbe Abgenommener Strom Corrente absorvida	⊣⊢		U.S. g.p.m.	0	13	22	26	31	40	44	53	66	79	88	110	132	141	158	176
						µF	V	m³/h	0	3	5	6	7	9	10	12	15	18	20	25	30	32	36	40
		kW	kW	HP	A			l/min	0	50	83	100	117	150	167	200	250	300	333	417	500	533	600	667
BP 3	1 x 230 V	1,4	0,75	1	6,6	25	450	H (m)	21,5	20,6	20	19,5	19,3	18,5	18	17,3	16	14	12	8				
BP 3	3 x 230-400 V	1,06	0,75	1	4,8/2,8				21,5	20,6	20	19,5	19,3	18,5	18	17,3	16	14	12	8				
BP 4	1 x 230 V	2	1,1	1,5	8,8	31,5	450		22					21,4	21	20,6	20	19	18,2	15	11,5	10		
BP 4	3 x 230-400 V	1,45	1,1	1,5	6/3,5				22					21,4	21	20,6	20	19	18,2	15	11,5	10		
BP 5	1 x 230 V	2,6	1,5	2	12,6	40	450		24							23,5	23	22	21,5	19	15	14	9	6
BP 5	3 x 230-400 V	2,1	1,5	2	8,5/4,9				24							23,5	23	22	21,5	19	15	14	9	6

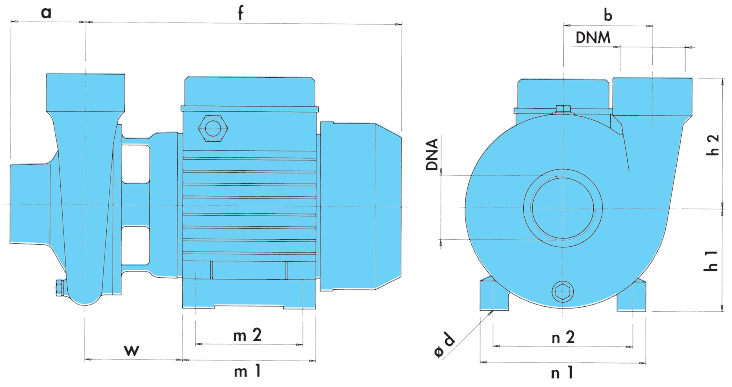

BP 3-4-5

DIMENSIONI E PESI

DIMENSIONS AND WEIGHTS - DIMENSIONES Y PESOS - DIMENSIONS ET POIDS
ABMESSUNGEN UND GEWICHTE - DIMENSÕES E PESOS

Tipo Type Typ	DNA	DNM	f	a	m1	m2	n1	n2	h1	h2	w	Ø d	Kg
BP 3	G 2"	G 2"	294	70	124	100	152	125	96	122	88	9	16
BP 4	G 2"	G 2"	294	70	124	100	152	125	96	122	88	9	19,2
BP 5	G 2"	G 2"	294	70	124	100	152	125	96	122	88	9	22

≅ 2850 1/min

BP 3

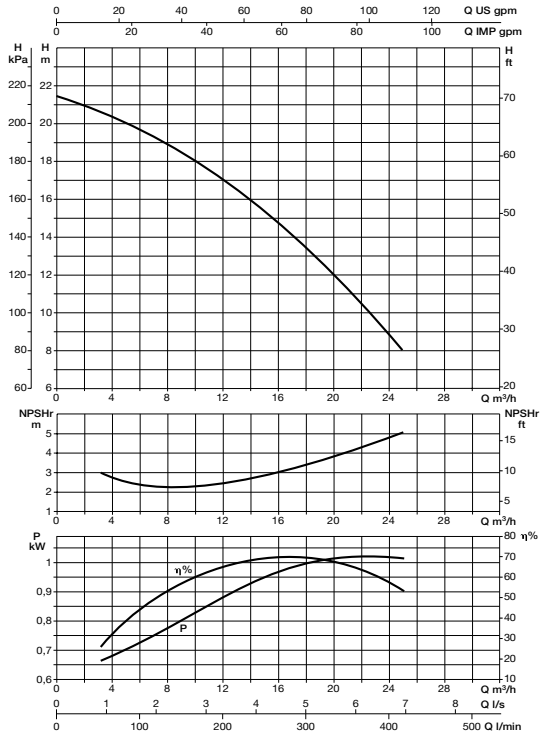

BP 4

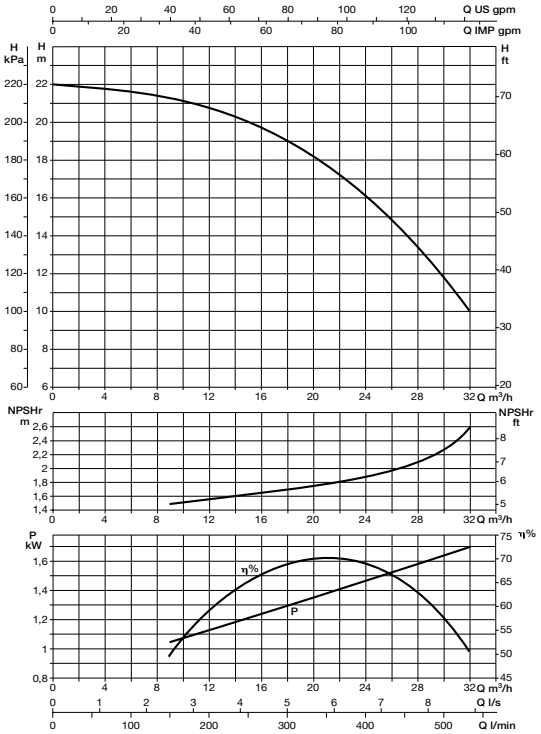

BP 5

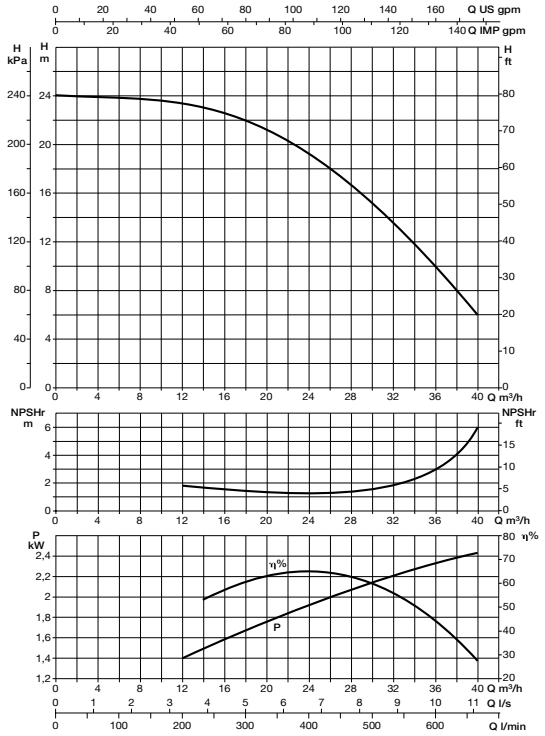

Le curve di prestazione sono basate su valori di viscosità cinematica = 1 mm²/s e densità pari a 1000 kg/m³. Tolleranza e curve secondo ISO 9906, appendice A.

The performance curves are based on the kinematic viscosity values = 1 mm²/s and density equal to 1000 kg/m³. Curve tolerance according to ISO 9906, attachment A.

Las curvas de rendimiento se refieren a valores de viscosidad cinemática= 1 mm²/s y densidad de 1000 Kg/m³. Tolerancia de las curvas de acuerdo con ISO 9906, parrafo A.

Les courbes de performances sont basées sur des valeurs de viscosité cinématique égale à 1 mm²/s et une densité égale à 1000 kg/m³. Tolérance et courbes conformes aux normes ISO 9906, annexe A.

Die Leistungskurven beruhen auf einer kinematischen Zähflüssigkeit von 1 mm²/s und einer Dichte von 1000 kg/m³. Abweichung und Kurven gemäß ISO 9906, Anhang A konstruiert.

As curvas de desempenho são baseadas em valores de viscosidade cinemática = 1 mm²/s e densidade igual a 1000 kg/m³. Tolerância e curvas segundo ISO 9906, parágrafo A.

BP

6-7-8

≅ 2850 1/min

CARATTERISTICHE IDRAULICHE

HYDRAULIC FEATURES - CARACTERISTICAS HIDRAULICAS - CARACTERISTIQUES HYDRAULIQUES
HYDRAULISCHE EINGESCHAFTEN - CARACTERÍSTICAS HIDRÁULICAS

Tipo Type Typ	Motore Motor - Moteur		U.S.g.p.m.	13	26	40	53	66	79	92	106	119	132	145	159	185	211	238	264	277	291	317	343	370	396	423	440	476	502	528
			m³/h	3	6	9	12	15	18	21	24	27	30	33	36	42	48	54	60	63	66	72	78	84	90	96	100	108	114	120
	kW	HP	l/min	50	100	150	200	250	300	350	400	450	500	550	600	700	800	900	1000	1050	1100	1200	1300	1400	1500	1600	1667	1800	1900	2000
BP 6E	0,59	0,8	H (m)	14,8	14,4	13,6	12,3	10,7	8,4	5,4																				
BP 6D	0,9	1,2		20	19,5	18,6	17,4	15,6	13,7	10,7																				
BP 6C	0,59	0,8		12,3	12,6	11,9	11,5	10,8	9,8	8,6	7,1	5,4																		
BP 6B	0,75	1		14,5	14,4	14,3	14	13,5	12,7	11,7	10,5	9	7,2																	
BP 6A	0,9	1,2		16			15,9	15,5	14,8	14	12,9	11,5	10,1	8,5																
BP 7D	1,1	1,5		12,7	12,7	12,6	12,5	12,3	12,1	12	11,7	11,4	11	10,5	9,6	8,3	6,7	5	2,9											
BP 7C	1,5	2		15,9	15,9	15,9	15,7	15,5	15,3	15,2	14,8	14,6	14,1	13,7	12,8	11,5	10	8,2	6,1											
BP 7B	2,2	3		19,4	19,4	19,4	19,2	19	18,8	18,7	18,4	18	17,6	17,2	16,3	15	13,4	11,7	9,6	8,5										
BP 7A	3	4		22,4	22,4	22,4	22,2	22	21,8	21,7	21,4	21	20,8	20,2	19,6	18	16,4	14,7	12,6	11,5	10,3									
BP 8C	3	4		16,5										16,5	16,4	16,2	15,8	15,3	14,7	14,3	14	13,2	12,3	11,4	10,3	9,3	8	6,5		
BP 8B	4	5,5		18,5										18,5	18,4	18,2	17,8	17,3	16,7	16,3	16	15,2	14,3	13,4	12,3	11,3	10	8,5	6,9	
BP 8A	5,5	7,5		20,5										20,5	24,4	20,2	19,8	19,3	18,7	18,3	18	17,2	16,3	15,4	14,3	13,3	12	10,5	8,9	7

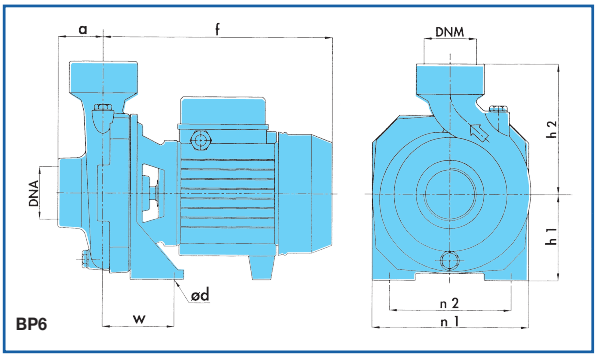

BP6

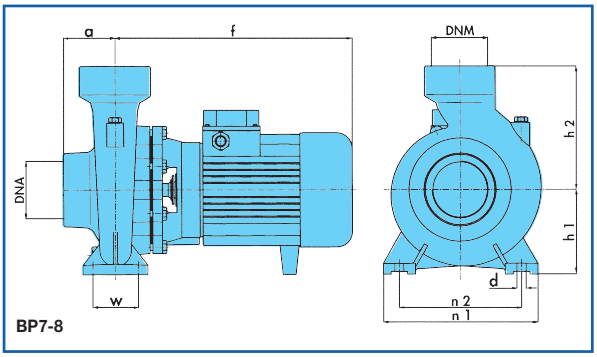

BP7-8

DIMENSIONI E PESI

DIMENSIONS AND WEIGHTS - DIMENSIONES Y PESOS - DIMENSIONS ET POIDS
ABMESSUNGEN UND GEWICHTE - DIMENSÕES E PESOS

TIPO *TYPE TYP*	DNA	DNM	f	a	n1	n2	h1	h2	w	Ø d	Kg
BP 6E	G 2"	G 2"	265	52	180	140	97,5	150	83	9	–
BP 6D	G 2"	G 2"	285	52	180	140	97,5	150	83	9	–
BP 6C-B	G 2"	G 2"	265	52	180	140	97,5	150	83	9	–
BP 6A	G 2"	G 2"	285	52	180	140	97,5	150	83	9	–
BP 7C	G 3"	G 3"	335	80	240	190	130	190	70	14	–
BP 7B	G 3"	G 3"	335	80	240	190	130	190	70	14	–
BP 7A	G 3"	G 3"	345	80	240	190	130	190	70	14	–
BP 7D	G 3"	G 3"	370	80	240	190	130	190	70	14	–
BP 8C	G 4"	G 4"	370	90	280	212	140	215	95	14	–
BP 8B	G 4"	G 4"	395	90	280	212	140	215	95	14	–
BP 8A	G 4"	G 4"	430	90	280	212	140	215	95	14	–

≅ 2850 1/min

BP 6 A-B-C

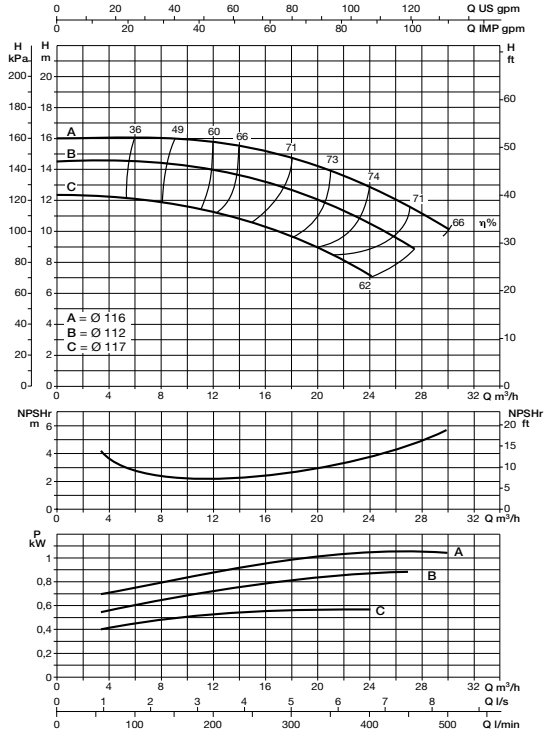

BP 6 D-E

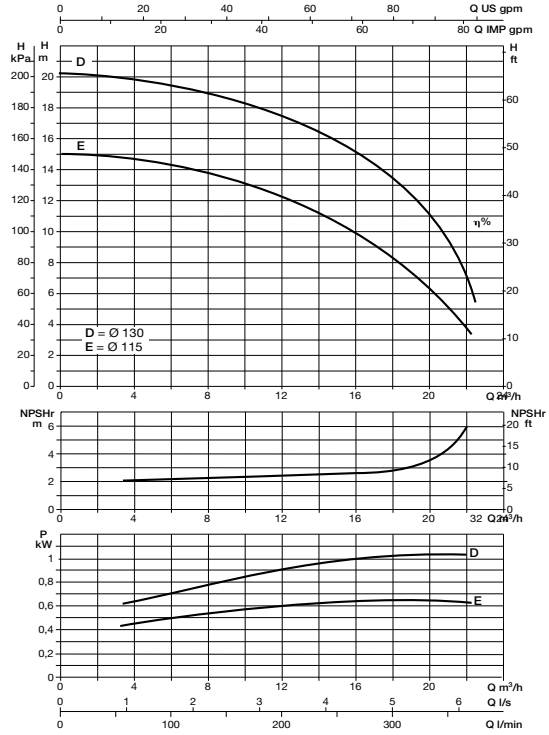

BP 7

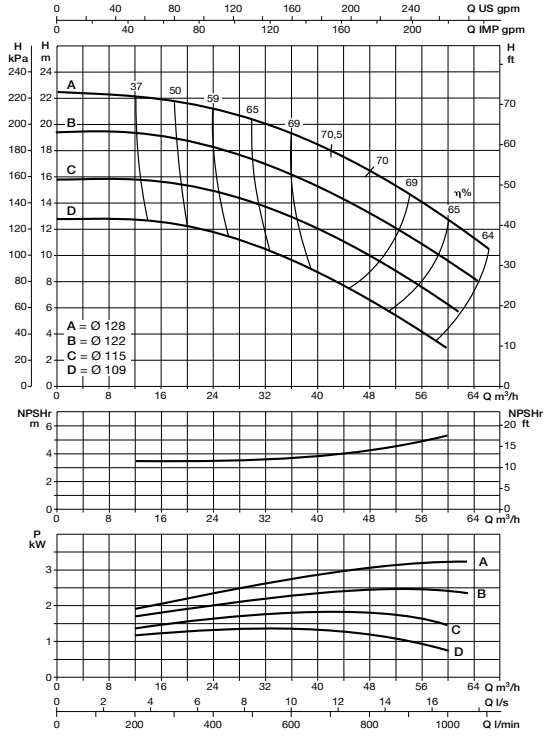

BP 8

